Statistical modeling of spiking activity in large scale neuronal networks

Ryan Christopher Kelly

CMU-CS-10-121
May 2010

School of Computer Science
Carnegie Mellon University
Pittsburgh, PA 15213

Thesis Committee:
Tai Sing Lee, Chair
Robert E. Kass
Geoffrey J. Gordon
Gary L. Miller
Kenneth D. Harris (Imperial College London)

Submitted in partial fulfillment of the requirements
for the degree of Doctor of Philosophy.

This research was sponsored by the National Science Foundation under grant number IIS-0713206 and National Institutes of Health under grant number 2-R01-MN06453704-A2. The views and conclusions contained in this document are those of the author and should not be interpreted as representing the official policies, either expressed or implied, of any sponsoring institution, the U.S. government or any other entity.

Keywords: neurons, primary visual cortex, V1, GLM, local field potentials, LFP, spike trains, network states

Abstract

Traditional visual neuroscience research has focused on determining the relationship between the activity of single neurons and the stimuli from the outside world, and more recently the interactions within pairs of neurons. These studies have typically recorded from neurons or pairs of cells in isolation. Recent advances in neural recording devices have made it possible to record simultaneously from hundreds of cells. Such data provide new insights into the interactions among the neurons, the connectivity of neurons in a local network, as well as the neural algorithms of information processing. These methods also present new challenges: the scaling of existing system identification and decoding techniques to address the dramatic increase in dimensionality and computational complexity, and the development of new statistical methods to infer the dynamic interaction and connectivity in neuronal ensembles during information processing.

We recorded neuronal activity from the primate primary visual cortex using 96-channel multi-electrode arrays during the presentation of a variety of visual stimuli. We observed that the large fluctuations in firing rate were shared across many cells in the array, regardless of stimulus. These network state changes are related to many other widely known neural phenomena: large spiking stochasticity, slow timescale correlation between cells, and neural oscillations. We sought to understand the extent to which these fluctuations could be captured with the data available.

A statistical technique, the generalized linear model (GLM), has recently begun to be used to model neural activity, due to both its flexibility and computational tractability. In this context, the models we built had explicit terms for the stimulus effects, coupling effects from other cells recorded simultaneously, and more global network effects. We found that the network terms could indeed explain many of the spikes, indicated that neuronal variability cannot be merely considered to be internal noise, but is widely shared across a population of cells. This approach shows how to incorporate the extra-stimulus data in identifying single cell firing properties, as well as taking a step toward reconciling our understanding of single cells with the computations being performed by the larger network.

Contents

Chapter 1

Introduction

The pioneering efforts of Adrian (1928); Hubel and Wiesel (1962); Mountcastle et al. (1957) and others using single electrodes to measure neural activity have built the foundation for much of our understanding of how the brain works. In the last decade alone, advances in electrode technology have begun providing for the recording of tens, hundreds, and thousands of cells. This progress has opened up new research possibilities in the study of neural population coding, computations performed by a network of cells. The data explosion stemming from these recording methods demand new statistical and computational tools, as most standard methods are tailored for the characterization of single cell tuning properties.

In this thesis we support the effort by developing computational tools to further the understanding of outstanding questions in the field:

1. What are the underlying sources of the apparent randomness of individual neurons' spiking activites?
2. How can we measure and understand correlated activity measured in a population of neurons?

We use the generalized linear model (GLM) technique to model individual cell spike trains with features of the stimulus and of the surrounding neuronal network. Our work goes beyond a simple linear model based on the stimulus-response relationship, providing a flexible and computational tractable framework capable of containing hundreds of parameters. We then show that neural variability can be characterized in part by a shared network component, and moreover that correlated spiking between pairs of cells is mostly due to these network fluctuations.

1.1 Background

One of the most striking features of spike trains is their variability – that is, the same visual stimulus does not elicit the same spike pattern on repeated presentations. This variability is often considered to be "noise," meaning that it is due to unknown factors. Identifying these unknowns should enable better characterization of neural responses. One effect of cross trial fluctuations that has received a great deal of attention is correlation between neurons. From neuroanatomy, we know that the visual cortex contains a rich pattern of connections. Because of these connections, the spiking activity of groups of cortical neurons is not independent – instead it is correlated on a range of time scales (Smith and Kohn, 2008). The correlation among neurons has most often been measured by simultaneous recording of nearby pairs. In the retina, it has recently become possible to record from a nearly complete population of certain types of ganglion cells in a region and identify the correlation structure of this population (Shlens et al., 2009). However, in cerebral cortex, recording a full population of individual neurons in a region is currently impossible, and large scale recordings *in vivo* have been rare. Correlated variability has a strong influence on population coding – it can enhance or diminish the information encoded within that population depending on a number of factors (Zohary et al., 1994; Shadlen and Newsome, 1998; Abbott and Dayan, 1999; Averbeck et al., 2006). Although it is possible for a signal to be encoded in the correlation strength itself (Kohn and Smith, 2005; Samonds and Bonds, 2005; Smith and Kohn, 2008; Huang and Lisberger, 2009), correlated variability is often merely removed in order to better reveal the signal. Experimenters typically repeat the visual conditions on multiple trials and simply average the neuronal responses, assuming that any unwanted noise is thereby diminished or removed.

An understanding of neuronal population activity is incomplete when measured only with spiking activity from a small subset of the total neurons in a region. Intracellular measurements of subthreshold activity have revealed that membrane potentials are continuously correlated between nearby cells in primary visual cortex (V1) (Lampl et al., 1999). In addition, the firing of neurons has been strongly linked to ongoing population activity measured with optical imaging (Tsodyks et al., 1999) and local field potential (LFP) (Nauhaus et al., 2009). This link to the state of the local population is an influential force affecting the variability in a cell's spiking behavior. Indeed, groups of neurons transition between "Up" (depolarized) and "Down" (hyperpolarized) states, which leads to cycles of higher and lower than normal firing rates (for review, see Destexhe and Contreras, 2006). Though they are often referred to as discrete states, this is somewhat deceptive: neuronal populations transition smoothly between epochs of high and low responsivity. These state transitions occur in sleeping and anesthetized animals, as well as in cortical slices (Johnson and Buonomano, 2007). Similar fluctuations in responsivity have also been reported in awake animal subjects (Leopold et al., 2003; Luczak et al., 2007) as well as awake human patients (He et al., 2008; Nir et al., 2008). Thus, a signal which reflects these states, and in turn helps account for some variability, would be an important tool for decoding a neuron's response.

The local field potential (LFP) is one such candidate signal. It is thought to reflect the average synaptic input to a region near the electrode (Mitzdorf, 1987; Buzsáki, 2004), and is known to be correlated with the subthreshold membrane potential fluctuations in nearby neurons (Eggermont and Smith, 1995; Petersen et al., 2003). Furthermore, slow dynamics of spiking activity can be inferred from the LFP (Rasch et al., 2008), and the phase of the LFP is predictive of multi-unit activity (Haslinger et al., 2006). However, there are a number of reasons why the LFP might not be a suitable signal for this purpose. Estimates of the spatial spread of LFP range from a few hundred microns to more than a few millimeters (Mitzdorf, 1987; Kruse and Eckhorn, 1996; Kreiman et al., 2006; Liu and Newsome, 2006; Berens et al., 2008; Katzner et al., 2009; Xing et al., 2009), and depend on laminae (Xing et al., 2009) and frequency (Frien et al., 2000; Henrie and Shapley, 2005; Liu and Newsome, 2006; Siegel and König, 2003). Furthermore, the feature selectivity of the LFP is broader than that of spiking activity (Kreiman et al., 2006; Liu and Newsome, 2006; Berens et al., 2008; Katzner et al., 2009). Though it is clear there is a relationship between LFP, neuronal states, and spiking activity, it is not known to what extent these factors can be disentangled to better decode spike-stimulus relationships.

Neural stochasticity

Neurons are often conceptualized as inherently stochastic from a systems level. Complete, biologically plausible models of single cell firing have existed for decades (Hodgkin and Huxley, 1952), but they generally require direct knowledge of the channel dynamics. For extracellular single unit recording data, the causes of a neuron's firing must be broken down more simply, into known and unknown sources. These methods are not as accurate, but are certainly more computationally tractable. One potential conception is that the firing rate is due to a stimulus effect plus some independent noise:

$$\mu = S + N \tag{1.1}$$

We can approximate μ by repeating the stimulus over many identical trials, and since we assume that the stimulus effect S and the noise N are independent, we achieve an estimate of $S = \mu - N$. If the noise is distributed in the same manner for different stimuli, we can measure the stimulus effects to different stimuli:

Figure 1.1 A: Responses of a single neuron to sine-wave grating movies. 120 trials of the same grating movie are shown here. The movie is a sequence of drifting gratings, with the orientation changing every 300ms. B: The peri-stimulus time histogram (PSTH) for the 120 trials in (A). The PSTH has been smoothed with a Gaussian window ($\sigma = 5ms$).

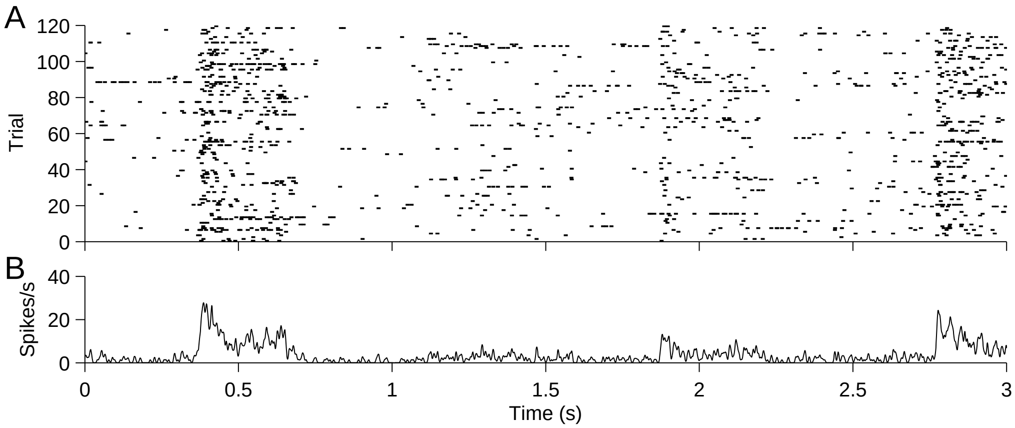

$$S_A = \mu_A - N \tag{1.2}$$

$$S_B = \mu_B - N \tag{1.3}$$

This simple averaging technique is useful for measuring the orientation tuning of a cell; the noise common to all stimulus conditions can be thought of as a baseline firing rate which is simply subtracted or otherwise ignored. This averaging can also be applied across a trial at fine timescales:

$$\mu(t) = S(t) + N(t) \tag{1.4}$$

or, assuming stationarity of the noise:

$$\mu(t) = S(t) + N \tag{1.5}$$

In this way, the firing rate during the presentation of a stimulus is directly related to the effect of a stimulus on firing. The time series $\mu(t)$ is known as the peristimulus time histogram (PSTH) - the stimulus aligned histogram of spike times. Figure 1.1A shows the responses of a neuron to repeated presentations of a sinewave grating stimulus. Figure 1.1B shows the smoothed PSTH for the set of trials shown in (A).

Figure 1.2 Example of a way that trial-averaging may oversimplify the estimation of stimulus transfer functions. A: A theoretical neuron, where the firing rate is simply the sum of a stimulus and noise contribution. Two stimuli are shown which drive the cell at different rates. For a given trial, the noise either adds ten spikes (N_1) or zero(N_2). B: If the distribution of noise changes depending on the stimulus, the bottom-up stimulus drive can be masked or reversed by trial averaging.

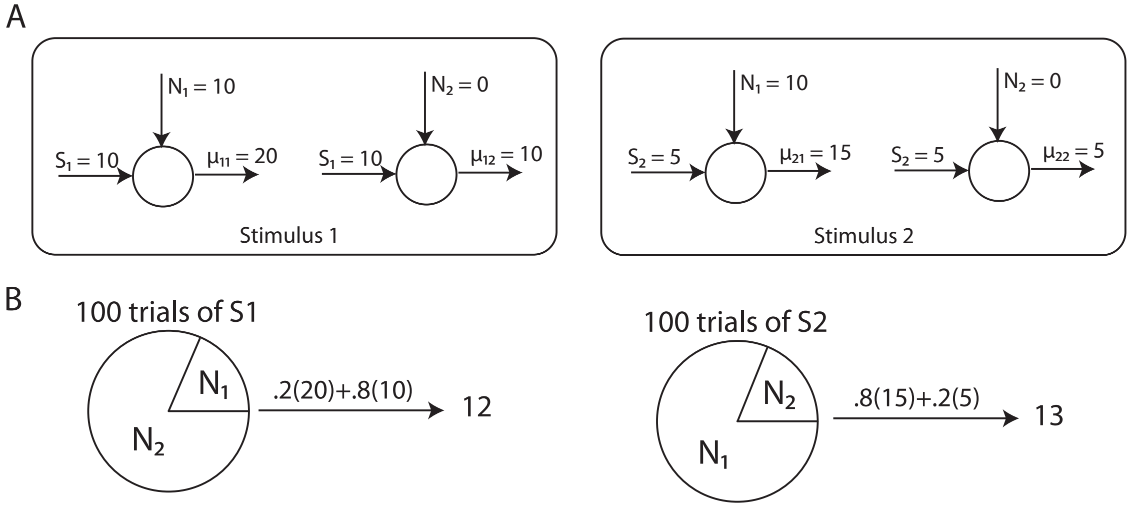

The stochasticity in the neuronal response is apparent in Figure 1.1. The regions of elevated firing are easy to see, but just knowing these epochs and the firing rates is not a guarantee that you will observe spikes during that portion of the stimulus on every trial.

The approach of trial averaging is acceptable as long as the noise is unrelated to the stimulus. Since neural noise is, in large part, a reflection of other cells firing, this is unlikely to be entirely true. Without explicitly modeling the noise term, it is possible to corrupt the measurement of bottom-up stimulus drive. To take a simplified example of this problem, if we want to determine the relative stimulus drive to two different stimuli, we can record responses during 100 presentations of each stimulus. For these particular cells, there are sometimes noise spikes added to the response of the cell, and the rest of the time none are added. Perhaps, for some high level reason (e.g. stimulus 2 is boring), the noise spikes are more likely to be added during the presentation of stimulus 2. Figure 1.2 gives an example of this kind of problem, and for the extreme case described here, the stimulus effect is completely hidden from the perspective of trial averaging. We would have to explicitly model the noise in some way to recover S_1 and S_2.

Figure 1.3 An example recorded spike train and the simultaneously recorded LFP from the same electrode.

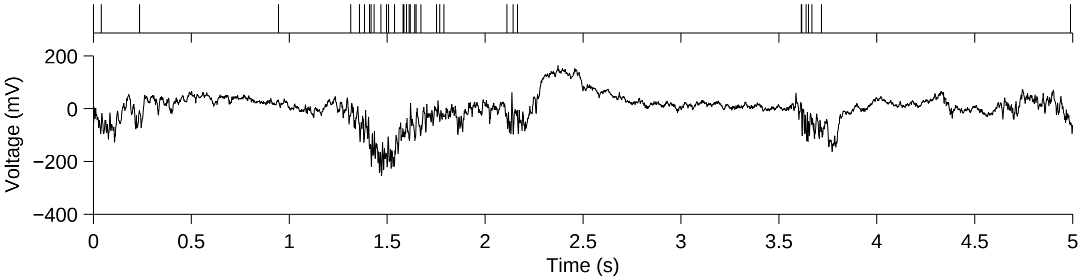

Local field potentials

There has been a large effort devoted to studying neural spiking behavior, but has been considerably less focused on the understanding of other signals like the LFP. Recent results have sharpened our understanding of many properties of the LFP. The LFP is thought to reflect the general input to a region, and is correlated spatially and temporally. The extent of the LFP coherence has been measured in some cases to be in excess of 4mm (Juergens et al., 1999), and the signal varies slowly relative to spike waveforms. Since the LFP is pooling from many hundreds of cells, it does not have a direct connection to any single cell's firing, but is more likely to reflect synchronized firing. Despite these constraints on the signal, a relationship has been found between cell firing and the gamma oscillations of the LFP (Rasch et al., 2008).

Figure 1.3 illustrates a spike train and the simultaneously recorded LFP (same electrode) during the presentation of a visual stimulus. The relationship between fast oscillations and spikes is evident here, but we also know the LFP is not driven by this cell alone, and only by a larger population of cells. So is it the case that many spikes are merely related to general network activity, and this network activity is reflected in the LFP?

Functional connectivity

We desire a modeling approach that can provide a greater understanding of neuronal correlation. Functional connectivity is typically computed via the cross-correlation between spike trains of different cells. The meaning, sources, and even the existence of various correlation measures remains hotly debated (Ecker et al., 2010). Our method of explicitly decomposing the different contributions on firing allows for an alternative and more targeted estimation of the functional connectivity among a group of cells. Here, we illustrate one way existing functional connectivity estimates can be difficult to interpret.

In extracellular recording, the relationship between a pair or group of cells can only be inferred, not directly measured. There are a variety of analyses that can be used, and they generally are statistical in nature, comparing the spike times between the cells in some way. Groups of cells for which the pattern of spike times fall outside of what we would expect by chance can be considered functionally connected. Some examples of this are two cells which fire synchronously more often than chance would predict based on their firing rates, or a cell which tends to fire right after another cell. The measurements take the form of a cross-correlation between the spike trains. If we have multiple neural recordings, we can explicitly build correction terms to eliminate the correlation due to common causes (e.g. correlation due to the stimulus).

Even with these controls in place, the causes of functional connectivity are mostly unknown. In the densely connected primary visual cortex, cells have hundreds or thousands of collaterals. There is thus a many-to-one mapping from network configurations to any single correlation metric. While these measurements can provide information about the network as a whole, in most cases they cannot pinpoint direct connections between cells.

Figure 1.4 illustrates this problem. In one configuration, there is some sort of global shared noise, and in the other, there is a causal, direct connection between two cells. The correlation between spike counts on 1000 "trials" is indistinguishable between the configurations. This is a very simple example, and serves only to show that even in the simplest kind of network, the meaning of measured functional connectivity is difficult to ascertain. Additionally, measurement of correlation with non-normal variables could also cause problems, particularly in calculating significance levels.

Computational challenges

To employ a GLM for separating and extracting the underlying contributions to neural activity in such a large data set, we had to address significant computational challenges. Dimensionality can be huge: for each time interval to be estimated, there are 10,000 or more parameters of the other cells and network that may be related to firing. To model stimulus effects, a 320×320 pixel movie can have 10^8 or more relevant parameters. This requires significant dimensionality reduction, and to our knowledge models of this type and scale have rarely been attempted in neural data analysis, with a few recent exceptions (Truccolo et al., 2010; Pillow et al., 2008). The form of regression we use is a tricky computational problem and required a large scale implementation of recently developed

Figure 1.4 Example of how spike correlation measurements do not pinpoint a single circuitry. A: Two distinct cellular arrangements. In the left panel, some shared noise affects the firing of two cells, A and B. There is not direct connection between the two. We generated Poisson samples where the mean spike count of each cell was 10 spikes and between 0 and 6 spikes (mean) shared noise additionally. In the second scenario, cell C has a mean spike count of 12 spikes, while cell D has a mean spike count of 10 spikes plus one-fifth of the actual number of spikes cell C fired on that trial - a direct connection. B: 2-dimensional histograms of the number of trials for each spike count pairing. That is, the value at (x, y) is the number of trials (out of 1000 total samples) where cell A had x spikes and B had y spikes. The correlation coefficients are shown above the plots. Though the correlation values are roughly equal, the underlying circuit is different.

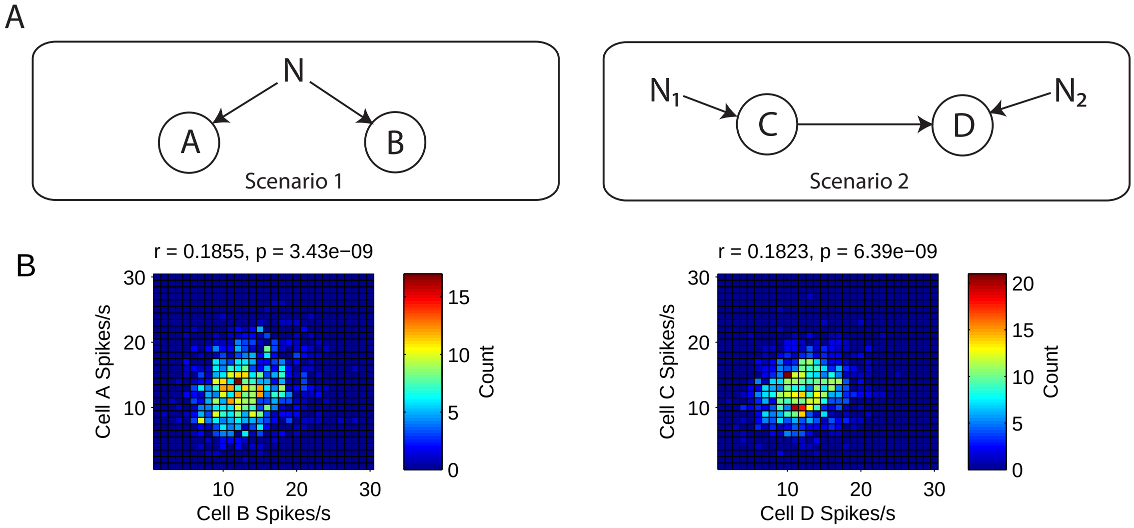

optimization approaches (Friedman et al., 2008). We have devoted considerable effort in adopting these statistical models to our problem, testing them in simulation studies, implementing performance assessments, and developing the infrastructure of data management that has allowed the processing of data of this scale. We have optimized the methods to produce productive models while walking the line between the bottlenecks of processing power, memory, and time.

Plan of attack and organization of the thesis

Our goal is twofold: first, to discover good models for cells using the aforementioned terms, and second, to make inferences about the underlying network with the insight gleaned from constructing these models. The organization of the work follows. We provide additional relevant background information in the corresponding chapters.

Chapter 2: We introduce the microelectrode array we use to collect data throughout this work, and also the neural data that is obtainable from the array. We also discuss the quality of these recordings compared to previously published data from single electrodes. Some of this chapter has been previously published (Kelly et al., 2007).

Chapter 3: We discuss neural stochasticity, and show how the network state can have a large impact on many cells across a population, independent of visual stimulation. We introduce a simple 1 variable GLM with the goal of removing some network activity from the total cell activity. The signal-to-noise ratio of responses to oriented grating stimuli improves across the neural population as a result of this removal. Thus, taking the network state into account can improve the recovery of the stimulus-response relationship. Some of this chapter has been previously published (Kelly et al., 2010).

Chapter 4: We provide details about the complete GLM and all its terms. The complete model has three main kinds of terms: a stimulus filter, spike coupling terms (this includes spiking history from the same cell), and network terms indicated by the LFPs. We provide details about the computational methods we used to fit these models in large data sets, and runs of the methods on simulated data. We also discuss ROC analysis, the model assessment method we use throughout this work.

Chapter 5: We apply the methods from Chapter 4 to real neuronal data. The models in this chapter use stimulus terms and spike coupling terms. We relate the models to standard measurements of the stimulus filter and spike correlation. We find that some cells are primarily predictable via the stimulus portion of the model (unaffected by the network activity) and others are mainly predictable from the other cell spikes (strongly coupled to the network state).

Chapter 6: We fit models using aspects of the LFP as the model terms. We contrast different models of the network state - the LFP value, the phase of the LFP signal, and the power in LFP frequency bands. We find that the LFP value and LFP power in the gamma frequency bands are the best models of the terms we tested.

Chapter 7: We put all the work together, fitting a complete model of neuronal firing using stimulus terms, spike coupling terms, and LFP value and gamma band power. We provide examples and conclusions about how this kind of model can help answer the two questions given above.

Chapter 2

Data and methods

In this chapter we describe details of microelectrode array data collection, and present an analytical study of the quality and stability of neural spike train recordings. This study, a collaboration between our laboratory and the laboratories of Tony Movshon and A.B. Bonds, we have collected and analyzed data from both anesthetized monkeys as well as anesthetized cats. As documented in Kelly et al. (2007), the general conclusion is that (1) the signal-to-noise quality of the array data is roughly comparable to single electrode data from published studies and (2) the temporal stability of the recordings is on the order of hours. Thus, we demonstrate that the quality of data is suitable for the application of the GLM techniques we lay out in the subsequent chapters.

2.1 Recording methods

As described above, advances in microelectrode neural recording systems have made it possible to record extracellular activity from a large number of neurons simultaneously. A substantial body of work is associated with traditional single electrode extracellular recording, and the robustness of the recording method has been proven experimentally. However, the recordings are limited to a small number of cells at a time, so much of the work has relied on compiling population statistics across many recording sessions. Multi-electrode recording systems theoretically have some major advantages over this paradigm. They increase the yield of neurons per recording session, and analysis of pairwise correlation benefits greatly from simultaneously recording from a large number of neurons (the number of pairs of cells is quadratic in the number of cells). The larger population also provides the possibility of examining higher-order (non-pairwise) interactions among neurons (Schneidman et al., 2006; Shlens et al., 2006). Finally, multielectrode systems have been developed which may be implanted and used for several months, which permits the study of learning in cell populations.

We recorded spiking activity with a specific microelectrode device, the Cyberkinetics "Utah" Array (Blackrock Microsystems, Salt Lake City, Utah) (Figure 2.1A). This device is a 10x10 grid of silicon microelectrodes (1 mm deep) spaced 400 μm apart, covering 12.96 mm^2. For most of this work, we focus on data collected from these arrays in anesthetized, paralyzed macaque monkeys (*M. fascicularis*). The techniques we use to record from the visual cortex of macaques have been described in detail previously (Cavanaugh et al., 2002; Smith and Kohn, 2008). To minimize eye movements, the animal was paralyzed with a continuous intravenous infusion of vecuronium bromide (0.1 mg/kg/hr). Anesthetia was maintained with sufentanil. We monitored vital signs continuously (EEG, ECG, blood pressure, end-tidal $\mathrm{P}_{\mathrm{CO}_2}$, temperature and lung pressure). The pupils were dilated with topical atropine and the corneas protected with gas-permeable hard contact lenses. We used supplementary lenses to bring the retinal image into focus by direct ophthalmoscopy, and then adjusted the refraction further to optimize the response of recorded units. Experiments typically lasted 4–5 days. All experimental procedures complied with guidelines approved by the Albert Einstein College of Medicine of Yeshiva University Animal Welfare Committee. The impedance of microelectrodes in the array ranged from 200-800 kOhm with an average of 400 kOhm. All measures of impedance were made with a 1 kHz sinusoidal current.

The details of the array insertion have been described in detail elsewhere (Smith and Kohn, 2008). Briefly, we inserted the array 0.6 mm into cortex using a pneumatic insertion device (Rousche and Normann, 1992), which led to recordings confined mostly to layers 2–3 of parafoveal V1 (receptive fields within 5° of the fovea). Signals from each microelectrode were amplified and bandpass filtered (250 Hz to 7.5 kHz) to acquire spiking data. Waveform segments that exceeded a threshold (set as a multiple of the rms noise on each channel) were digitized (30 kHz) and sorted off-line. We first performed a principal components analysis by waveform shape (Shoham et al., 2003) and then refined the output by hand with custom time-amplitude window discrimination software (written in MATLAB; MathWorks). We developed this software in-house for sorting this array data, and Figure 2.2 has a screenshot of the software GUI.

Figure 2.1 Cyberkinetics microelectrode array and example waveforms. **A**, The array, closeup and perspective with penny. **B**, Examples of sorted waveforms and signal to noise ratios from 3 representative channels and 1 channel of noise.

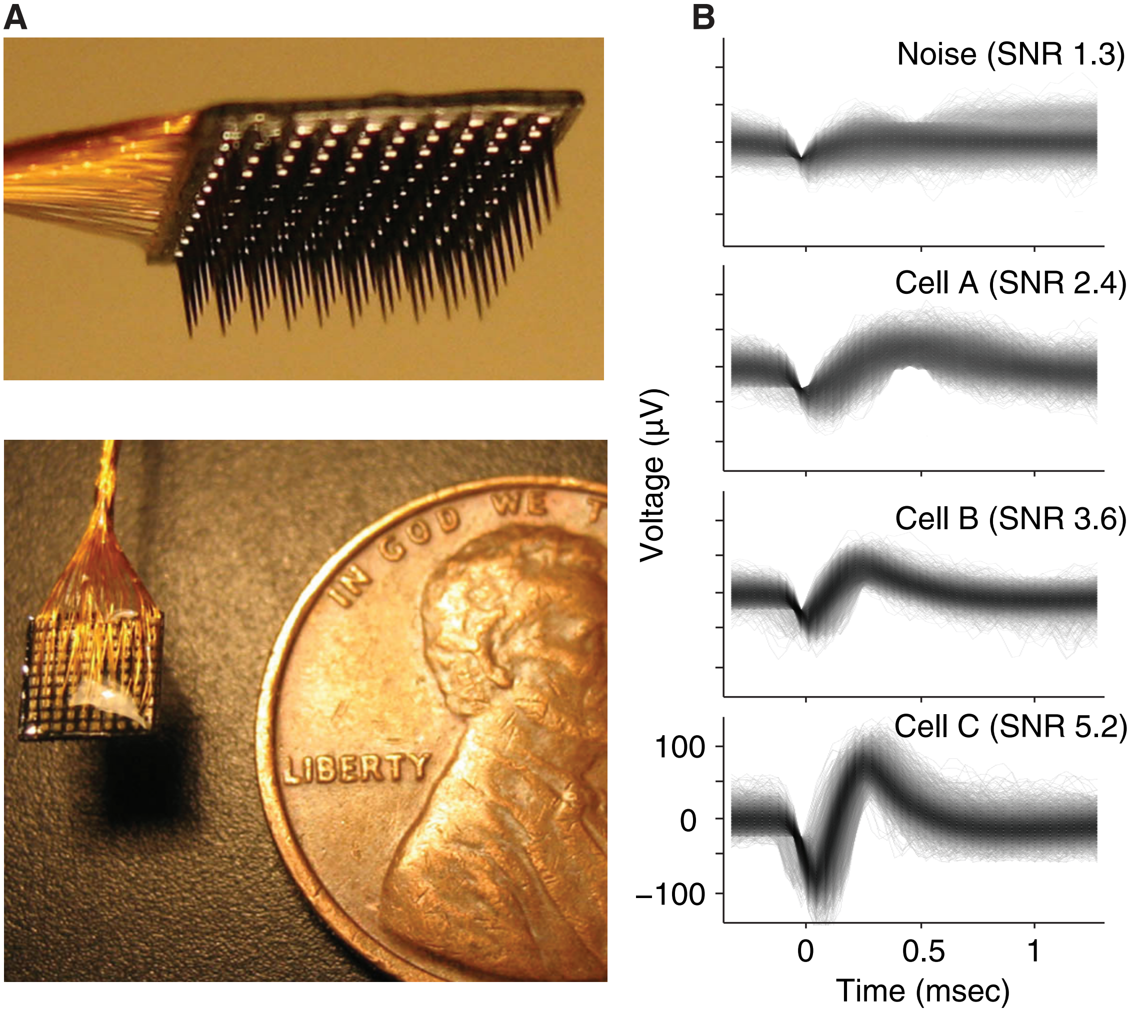

Figure 2.2 Screenshot of our custom spike sorting software. Waveforms are in the large panel, inter-stimulus intervals on the right, absolute spike times are below. Different sort codes are different colors (e.g. red,green,gray).

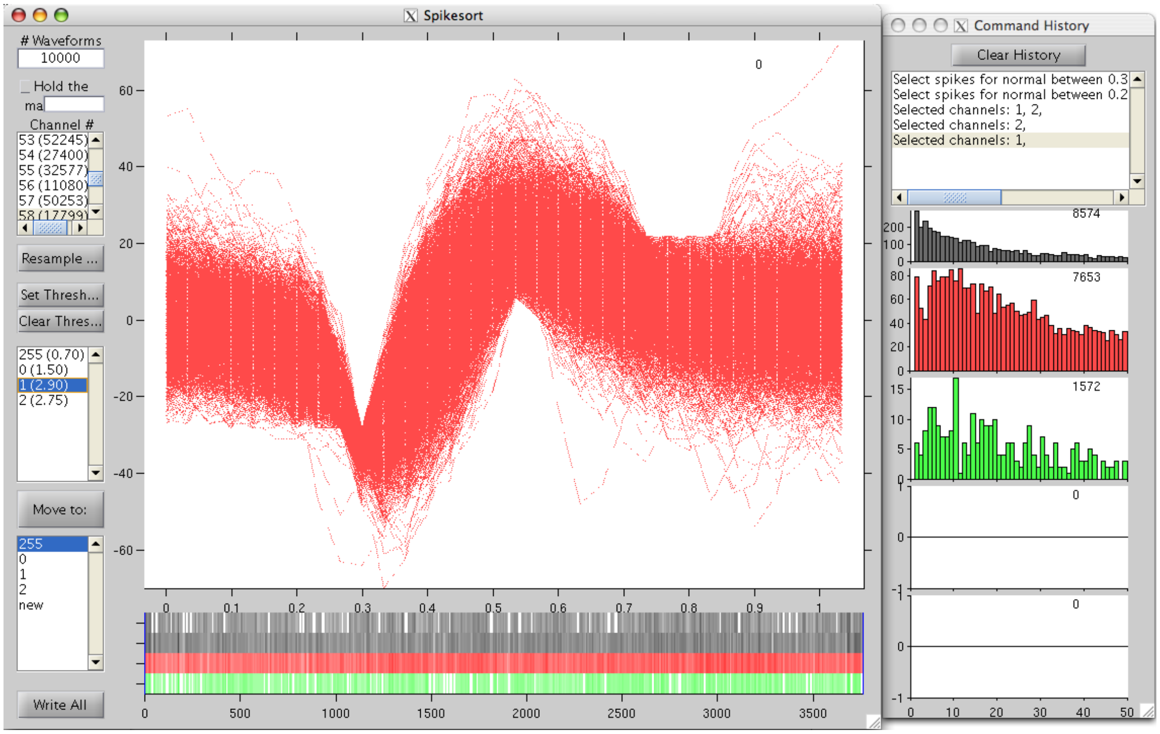

\# Waveforms: 10000

Hold the ma

Channel #
53 (52245)
54 (27400)
55 (32577)
56 (11080)
57 (50253)
58 (17799)

255 (0.70)
0 (1.50)
1 (2.90)
2 (2.75)

255
0
1
2
new

```
Select spikes for normal between 0.3
Select spikes for normal between 0.2
Selected channels: 1, 2,
Selected channels: 2,
Selected channels: 1,
```

2.2 Validity of array recordings

In this section, we assess this experimental approach for anesthetized acute (non-chronic) preparations, and compare the quality of recordings to those provided by the traditional single electrode method. We analyzed recordings from single electrodes and the Utah array in macaques and cats. Many reports on the quality (Nordhausen et al., 1996) and long term stability (Suner et al., 2005) of array recordings have not made a quantitative, direct comparison with established single electrode recordings. We addressed this uncertainty by comparing waveforms recorded with the array to waveforms recorded with accepted single electrode techniques. We found that the array yields good recordings on a large number of electrodes, with qualities comparable to those from single electrode recordings. On average, the recording quality is somewhat lower than that of single electrodes, but nonetheless the assessment of tuning properties such as the spatiotemporal receptive field and orientation tuning remains unchanged.

As mentioned, we analyzed waveforms from single electrode recordings in anesthetized, paralyzed macaque monkeys and cats (*F. catus*). We included microelectrode array recordings in cats. In all of these preparations, anesthesia was maintained with sufentanil and propofol with nitrous oxide, respectively. Monkeys were paralyzed with vecuronium bromide, and cats were paralyzed with pancuronium bromide. Single electrodes had a range of 1.2-3 MOhm in the macaque recordings (tungsten in quartz), and 0.5-2 MOhm in the cat recordings (tungsten in glass). Specific procedures for each recording preparation have been reported previously: cat single electrode (Snider et al., 1998), cat array (Samonds et al., 2006), monkey single electrode (Cavanaugh et al., 2002).

This yielded 105–129 candidate neural units from the 3 array implants, with roughly one half estimated to be well isolated single units similar in quality to those recorded with single microelectrodes. LFPs were acquired from the same electrodes simultaneously by band pass filtering the raw signal (0.3 Hz to 250 Hz) and sampling at 1 kHz. The LFP signal was then smoothed with a 100 ms boxcar filter for all subsequent analysis (50 ms and 200 ms filters produced the same results).

2.2.1 Signal to noise ratio

Using this procedure, we analyzed 58 V1 cells from single electrodes in cat, 38 V2 cells from single electrodes in macaque, 269 V1 cells from three microelectrode arrays in cat, and 301 V1 cells from three microelectrode arrays in macaque. In Figure 2.1B we show waveforms from three neurons recorded with the microelectrode array in macaque V1. These examples span the quality range we typically observed with arrays. Given these isolated single units, we computed signal to noise ratios (SNR) for collections of waveforms recorded in one hour periods for each of the four preparations. These waveforms have already been selected as exceeding the background noise during spike sorting, as described above. The SNR is computed as the ratio of the amplitude of the average waveform to the standard deviation of waveform noise (Nordhausen et al., 1996; Suner et al., 2005). That is, if each of k waveforms has n samples, then the collection of waveforms is

$$W = \begin{bmatrix} v^1(t_1), v^1(t_2), \ldots v^1(t_n) \\ \vdots \\ v^k(t_1), v^k(t_2), \ldots, v^k(t_n) \end{bmatrix} \tag{2.1}$$

with the mean waveform denoted as $\overline{W}$. The matrix of noise values (deviations from the mean) is thus

$$\epsilon = W - \begin{bmatrix} \overline{W} \\ \vdots \\ \overline{W} \end{bmatrix} \tag{2.2}$$

and SD_ϵ is the standard deviation of the collection of all entries in ϵ. The SNR is now

$$\text{SNR} = \frac{\max(\overline{W}) - \min(\overline{W})}{2 * SD_\epsilon} \tag{2.3}$$

Alternate definitions of SNR exist, such as the relative power of signal to noise, but the results presented here did not change with this alternate definition.

2.2.2 Response properties

Waveforms collected with the microelectrode arrays were similar in shape to waveforms collected using single electrodes, and neuronal response properties were similar as well. To demonstrate this point, we analyzed neural responses to a variety of stimuli collected with macaque V1 array implants. Orientation tuning curves were derived from responses to drifting sinusoidal gratings (Figure 2.3A). Most isolated cells showed clear orientation preference, and orderly shifts in orientation preference could be seen across the electrode positions in the array. In addition, we computed spatiotemporal receptive fields (STRFs) for cells responding to white noise stimuli using spike triggered averaging (Figure 2.3B). STRFs were found for cells when a contiguous 30 pixel area of the spike triggered average exceeded 3 standard deviations of the noise average. Of the cells isolated with this array, 60-65% revealed STRFs. Overall, we found that tuning properties were similar to those

Figure 2.3 Response properties. **A**, Orientation tuning curves for 16 example neurons in response to a sinusoidal grating drifting in 12 different directions. The grating was fixed at a spatial frequency of 1.3 cycles per degree, temporal frequency of 6.25 Hz, size of 8°, and duration of 1.28 sec with 1.5 sec between stimuli. **B**, Spatiotemporal receptive fields generated with reverse correlation of responses to white noise stimuli for the same 16 neurons.

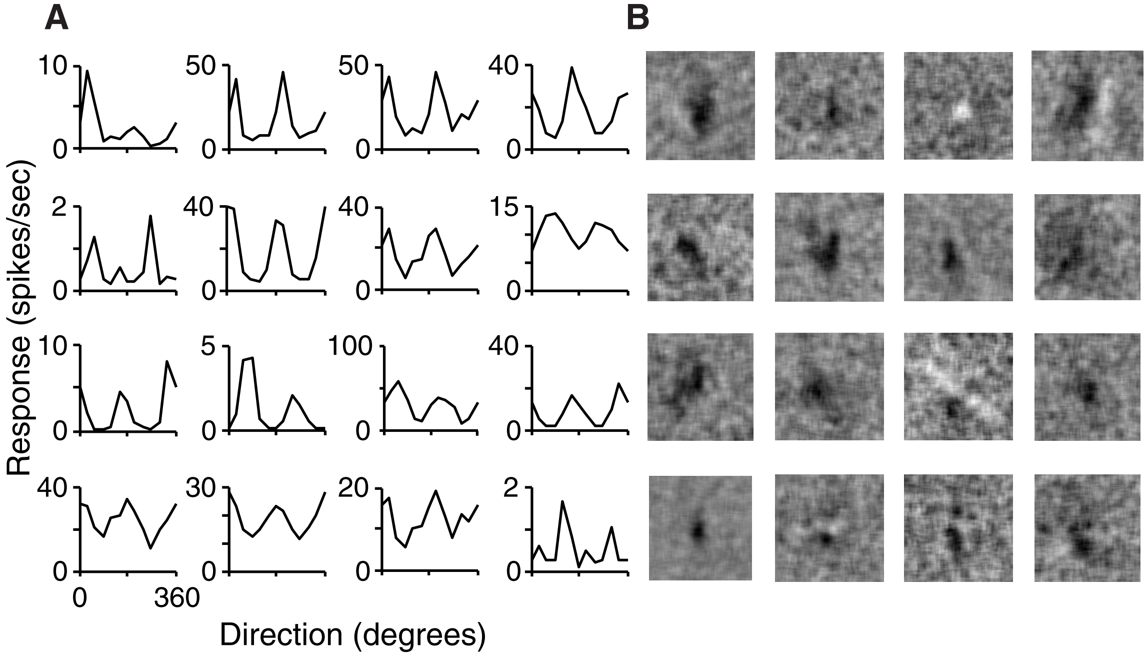

Figure 2.4 Signal to noise ratio in the four preparations. Macaque array SNR (**A**) tended to be lower than single electrode SNR (**B**, Two-sample Kolmogorov-Smirnov goodness-of-fit hypothesis test, $p<0.0001$). Similarly, cat array SNR (**C**) was lower than single electrode SNR (**D**, $p=0.046$). Finally, there was a trend for recordings in cat to have higher SNR than recordings in the macaque for single electrodes ($p=0.10$) and arrays ($p<0.0001$). All SNR values were computed from the waveforms over approximately 1 hour of recording time.

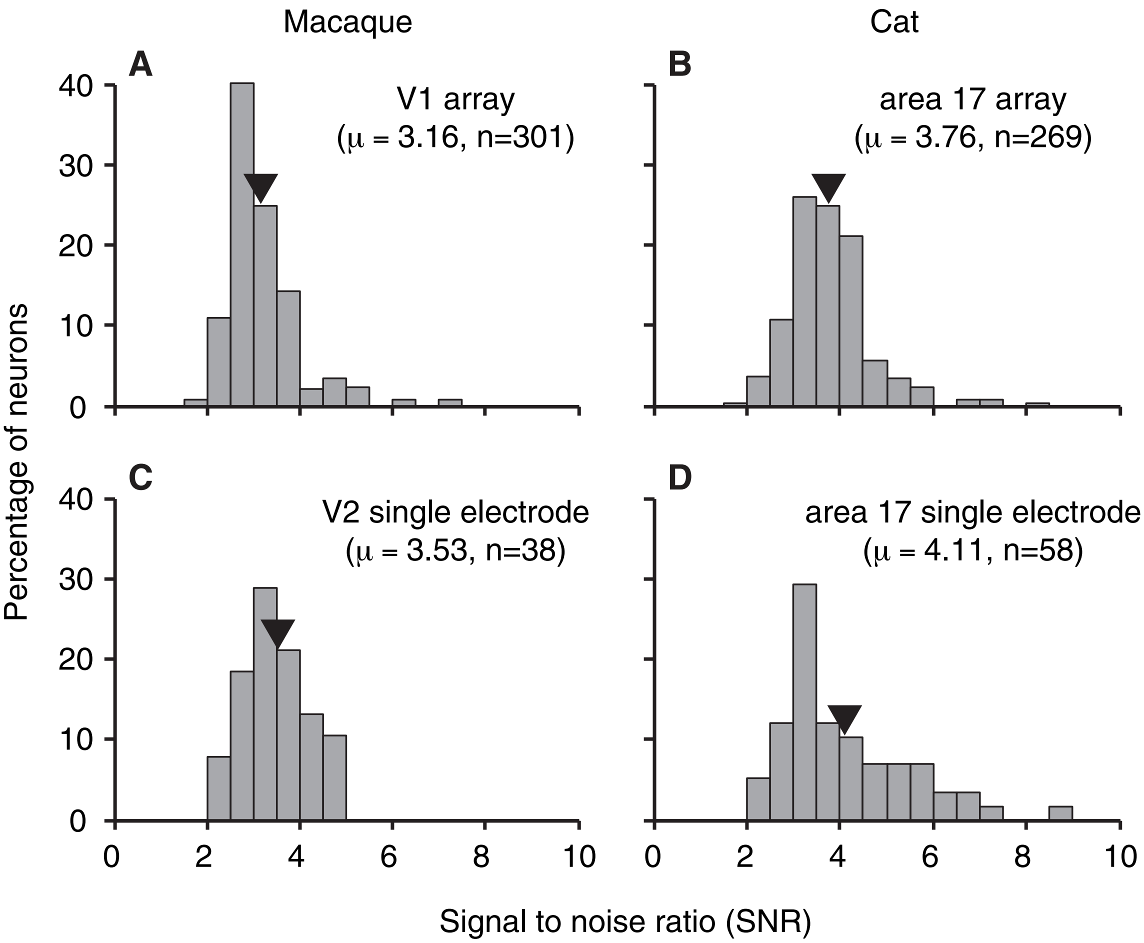

previously reported for orientation tuning (Hubel and Wiesel, 1968; Ringach et al., 2002b) and STRFs (Jones and Palmer, 1987).

We compared the distribution of SNRs across the different animals and methodologies (Figure 2.4). On a population level, SNR values for the arrays tended to be somewhat lower than those from single electrode recordings in both macaques and cats (see legend for statistics). One reason for this is that the array's electrode depth is fixed after implantation and cannot be adjusted to better isolate a cell as is typically done in single electrode recordings. The average SNRs from cat recordings were somewhat higher than from macaque data. This may be due to a true difference between species, or merely related to variations in recording setups. Despite the disparity in distribution means, the cells in the different conditions span the same SNR range – cells with the lowest SNR from arrays were still within the distribution from accepted single electrode recordings using an online dual time-amplitude window discriminator.

2.2.3 Stability of recordings

One advantage of the acute preparation is the ability to record for many hours consecutively. We addressed the stability of recording across a 29 hour period from one of our macaque array implants. Our sorting method was applied across the entire recording duration, and thus quality of recordings from individual cells was tracked over time. Figure 2.5 shows the change in SNR for all cells over the time period starting 2 hours after array implantation. Most SNR values tended to remain relatively constant throughout recording, with a few fluctuating between high and low SNRs. One trend we observed was that cells had lower SNR values near implantation and improved over the course of recording (Pearson $r = 0.27$, $p < .0001$). Out of 127 cells from this array, 88 (69%) had a significant ($p < .05$) increase in SNR, while only 2 cells showed a significant decrease in SNR. Evolution of the mean SNR over time is shown at the top of Figure 2.5. This could indicate that the pressure of the insertion caused the suppression of higher quality neural signals, and the return to normal may take many hours after insertion.

2.2.4 Discussion

Use of the Cyberkinetics microelectrode array has some considerations relative to single electrode techniques. It is currently manufactured in 2 fixed electrode lengths (1 or 1.5 mm), and insertion depth is not adjustable after implantation. The size and shape of the array prevents implantation in locations accessible to single electrodes, such as within sulci.

Figure 2.5 Stability of signal to noise ratio. Here we show the log(SNR) values for a continuous 29-hour recording session from one array implant. The cells here are sorted in decreasing order by average SNR value across time. The plot above shows the average SNR across all cells for each hour (error bars are ±1 SEM).

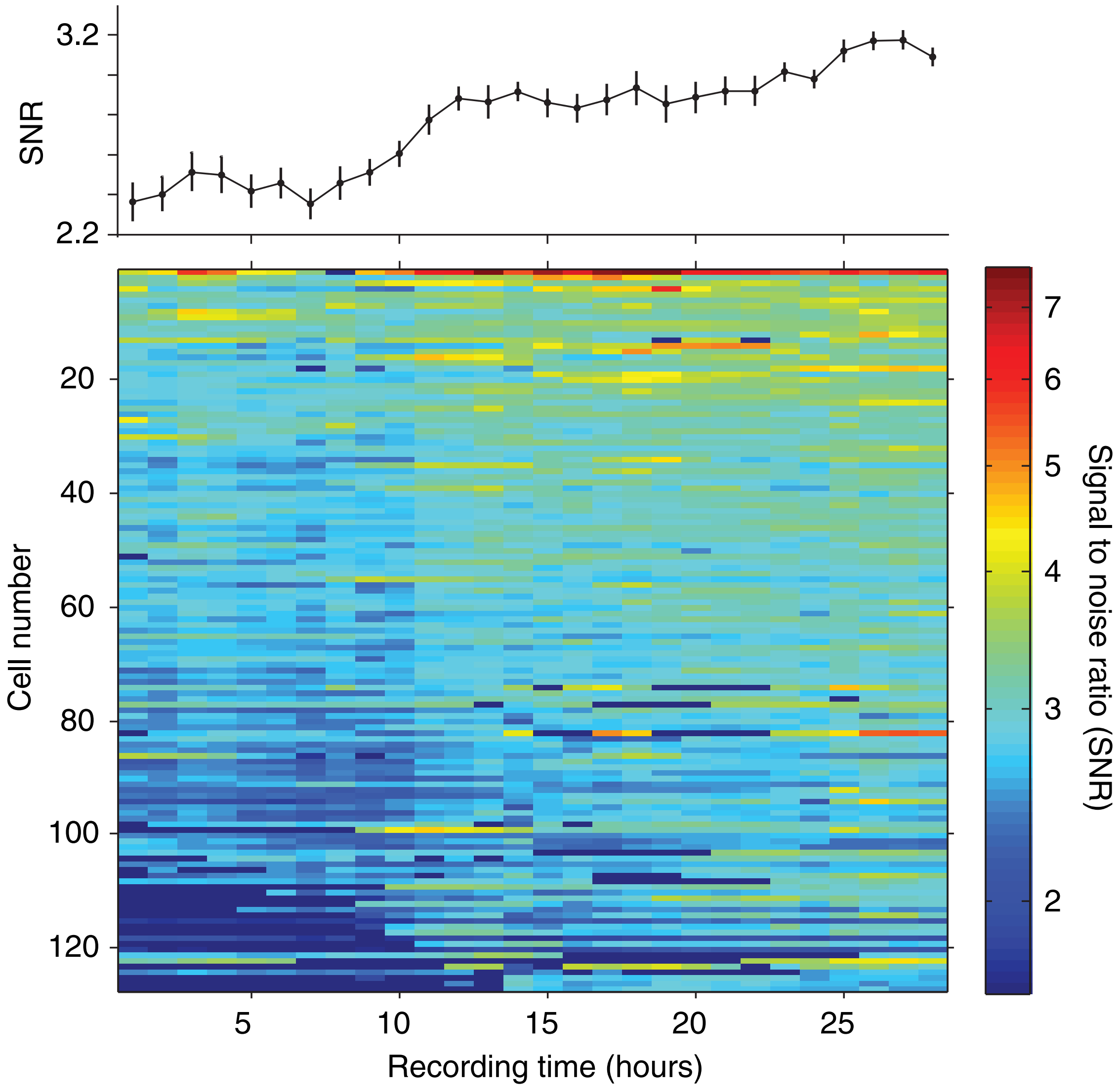

Also, since the array is flat and the cortical surface is curved, there is some chance that electrodes record from different layers. Finally, the implant procedure is somewhat more complicated than the preparation for single electrode recordings (Rousche and Normann, 1992). However, we observed no significant damage or edema after implantation and even after removal of the array.

We found that the array produced SNRs similar to those of single electrode recordings, both when the same spike sorting method was used and when spikes were sorted with standard online techniques. Although the ranges of SNR distributions were similar, single electrode recordings had higher SNR values on average. This may be due to the higher impedances of single electrodes, but is also likely to be strongly influenced by the fixed electrode depth of the array. The stability of recording may be influenced by the fact that single electrode setups are mounted externally, while the array is allowed to float with the motions of the cortex due to heartbeat and respiration. Our recordings from arrays had orientation tuning and spatiotemporal receptive fields in most cells. These cells were relatively stable throughout the day after implantation, with no signs of degradation after 30 hours – indeed, the signals tended to improve over time. A typical array implantation yielded 100 distinct candidate waveforms split roughly evenly between single unit and multiunit activity. Aside from increasing the amount of single unit data, arrays produce a high yield of neuronal pairs, providing a viable foundation for the study of higher order correlation properties.

2.3 Stimulus details

For the rest of this work, we focus on these microelectrode recordings in monkeys, with recording procedures described above. We studied the responses of cells to visual stimuli, presented on a computer screen. The cat data presented above was only for comparison in this chapter, and the remainder of this document deals with data recorded from arrays implanted into V1 of anesthetized monkeys. All stimuli were generated with custom software on a Silicon Graphics Octane2 Workstation and displayed at a resolution of 1024×768 pixels and frame rate of 100 Hz on a CRT monitor (stimulus intensities were linearized in luminance). Four kinds of stimuli were presented: gratings, natural movies, gaussian white noise movies, and a blank screen. The full-contrast sinusoidal gratings (presented in 2 of the 3 array implants) consisted of a pseudo-randomly chosen sequence of directions of drift, each lasting 300 ms and then proceeding to the next direction with no blank frames between. We used a total of 98 directions, evenly spaced, resulting in a sequence lasting roughly 30 s. Because we never repeated the same direction in a block, this 30 s stimulus comprised a unique “movie” of gratings in which no frame was repeated. This movie, with the same pseudo-random order of drift direction, was repeated 120 times. The spatial frequency (1.3 cycles per degree) and temporal frequency (6.25 Hz) were chosen to fit the preference of parafoveal V1 neurons (Valois et al., 1982; Foster et al., 1985; Smith et al., 2002), while the position and size (8° diameter circular aperture) of the grating were sufficient to cover the receptive fields of all the neurons. We also presented a natural movie stimulus, which was a square 5° 30-second segment of a consumer film, repeated 120 times. Finally, we presented gaussian white noise movies, with 8 pixel spatial blocks chosen independently from a gaussian distribution. The movies were 5° in width and height, 320 by 320 pixels. The stimuli were all surrounded by a gray field of average luminance. Both the natural movie and white noise stimuli changed frames every 4 refreshes (40ms) and so were effectively 25Hz.

Chapter 3

Shared noise and neural stochasticity

As mentioned above, stochasticity in neural activity to the repeated presentation of a stimulus is typically dealt with by averaging activity over many repetitions of the stimulus. The sources of this noise are not well understood *in vivo*, but they certainly include measurement noise and firing noise intrinsic to the neuron. Monitoring large numbers of neurons in primary visual cortex (V1), as we can with the microelectrode array, allows us to observe many other parts of the network. In many cases the state of the larger network can profoundly affect cell spiking, and can even rival stimulus driven behavior in magnitude. We found that this network state can be estimated with the band-passed electrode signal (given here by the LFP). To model cell firing, we used the generalized linear model (GLM), a well known statistical technique (Paninski et al., 2007; Pillow et al., 2008) that has recently begun to be applied in modeling population data in the retina (Pillow et al., 2008). These models can contain explicit terms for the various sources underlying the firing of neurons and can provide a more accurate assessment of their contributions.

This chapter reports on two key observations revealed by the simultaneous recording of a large neuronal population:

- In the absence of visual stimulation, neural populations can exhibit periods of synchronous activity elevation and depression.
- These synchronous epochs, known elsewhere as up and down states, tend to relate to the LFP value recorded by the same or nearby electrodes.

These synchronous activity changes are clearly related to underlying network factors rather than a visual stimulus, and may contribute to the apparent variability of spike trains during stimulation or behavior as well. We propose to use the LFPs as a proxy for a latent network state variable, and introduce a basic GLM to explore the impact of including this extra-stimulus factor in estimating the tuning properties of neurons. We demonstrate an improvement in the signal-to-noise ratio of orientation tuning curves of neurons with these models, which suggests that the LFPs can be used to estimate the network state which contributes to neural firing. The basic finding also has another practical implication: even in single unit recording, LFPs obtained from the same electrode can be used to improve spike interpretation without requiring simultaneous recordings from other electrodes.

3.1 Correlated fluctuations in spiking and the local field potential

We simultaneously recorded single- and multiple-unit neuronal activity (sorted offline) and LFPs from 100-electrode Utah arrays implanted in V1. We measured responses to sequences of sinusoidal gratings and natural movies as well as spontaneous activity with a mean gray screen. By pairing the spiking response on each electrode with the LFPs recorded from each of 96 active electrodes, we were able to measure and model the dependence of spike trains on the LFP.

In the absence of a visual stimulus, neurons in V1 respond at a baseline rate which varies from nearly no activity to tens of spikes per second. This rate is of course not constant – neuronal activity changes in a seemingly random pattern over time. However, some of that apparent randomness can be explained when the simultaneous responses of other neurons are observed. In Figure 3.1A, the responses from 128 sorted units (about half of these are single unit and half multi-unit) from a single array are shown in a raster plot for a 15 s period. If the neurons were responding randomly and independently, there would be no structure apparent in this plot. However, there are a number of prominent vertical bands present (for instance, one at roughly 8 s). These bands are produced by the temporally coordinated responses of a large portion of the neurons in the population. This kind of correlation in spiking has been reported previously in spontaneous and evoked activity in both anesthetized and awake animals (Zohary et al., 1994; Shadlen and Newsome, 1998; Bair et al., 2001; Kohn and Smith, 2005; Smith and Kohn, 2008; Huang and Lisberger, 2009).

Patterns of network activity such as these, or network "states", are well characterized in a number of systems and recording preparations (for review, see Kohn et al. (2009)). One means of measuring the state of a system is through the field potentials, which are thought to represent the sum of all synaptic inputs to a region of cortex (Legatt et al., 1980;

Figure 3.1 A: The activity of a neuronal population recorded with the array. In the upper plot, each row depicts the firing of one cell during spontaneous activity (the room is dark). Most cells in the population exhibit correlated activity on a slow time scale. The local field potential, shown below, typically contains peaks during the epochs of high correlated firing. B: The local field potential is averaged across all electrodes in this figure, and the y-axis is flipped for illustrative purposes.

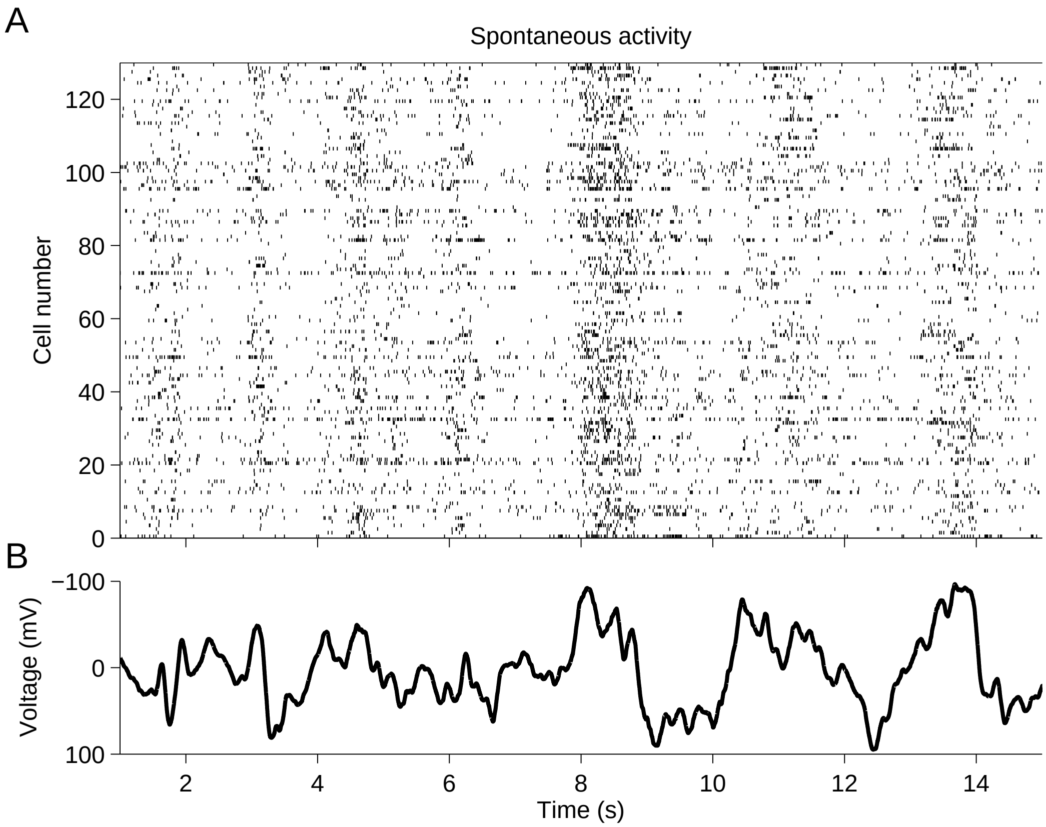

Gray et al., 1995). We compared the LFP (Figure 3.1B recorded simultaneously) with the spontaneous spiking activity in a population of neurons. We found that the states which contained a large number of spikes ("Up", or depolarized states) tended to correspond to large negative fluctuations in the LFP. Similarly, the absence of spikes ("Down", or polarized states) correspond to positive trends in the LFP.

Although Figure 3.1 only displayed correlated fluctuations in spontaneous activity, similar fluctuations were also present during the presentation of a visual stimulus. Figure 3.2 shows two sets of 5 raster plots, each created in the same way as Figure 3.1A, for five repeated presentations of a sequence of gratings (Figure 3.2A) or a natural movie (Figure 3.2B). In panel A, the sequence of gratings is identical in trials 1–5. Thus, the presence of a period of high activity on one of the trials that does not occur at the same time on all of the trials represents an "Up" state. Because the neurons prefer different orientations, there is no period in the grating sequence during which all of the neurons tended to fire in response to the visual stimulus. For this reason, the "Up" states were easy to identify. For the five identical natural movie repeats (Figure 3.2B), stimulus-dependent and independent correlated activity were more difficult to separate. Although correlated "Up" states are present, there were also periods of high activity in the entire population corresponding to stimulus events, presumably abrupt scene transitions, that altered the response of a large group of the recorded neurons. This mingling of stimulus-driven and state-driven activity makes it difficult to decode the signals sent by the spikes from a single neuron. However, with information about the population activity, it is possible to separate these two factors. Such a separation is certain to be imperfect - it is difficult or impossible to assess the "true" meaning of an individual spike. Nonetheless, we use a quantitative measurement (orientation tuning) which allows us to infer that the signal due to the stimulus has been increased relative to the network "noise", utilizing the assumption that the stimulus and network components are independent components which together comprise the neural response.

3.2 A generalized linear model for the effects of network state

Each spike train is a sequence of spike times and the natural statistical framework for spike train analysis is that of point processes, which may take a rather general form (Paninski et al., 2009). It is simplest to assume the spike trains follow inhomogeneous Poisson processes, and for our analyses it is unlikely that more complicated models would change our conclusions. We used time bins of duration 1 ms, ensuring that each bin has at most one spike due to the natural refractoriness of neurons. A spike train may thereby be considered

Figure 3.2 Network fluctuations differ across repeated identical visual stimulation. A: The stimulus is a movie of drifting gratings of different orientations, 300ms per orientation. For each trial, the stimulus is identical. Stimulus independent correlated activity occurs differently on each trial. B: The stimulus is 10 seconds of a single natural movie, for a different population than the one shown in (A). Stimulus independent correlated activity is apparent and also some stimulus-dependent activity is visible. For example, at 9 seconds into the stimulus the features in the movie begin to change more rapidly, and the movie drives the population activity more strongly as a result.

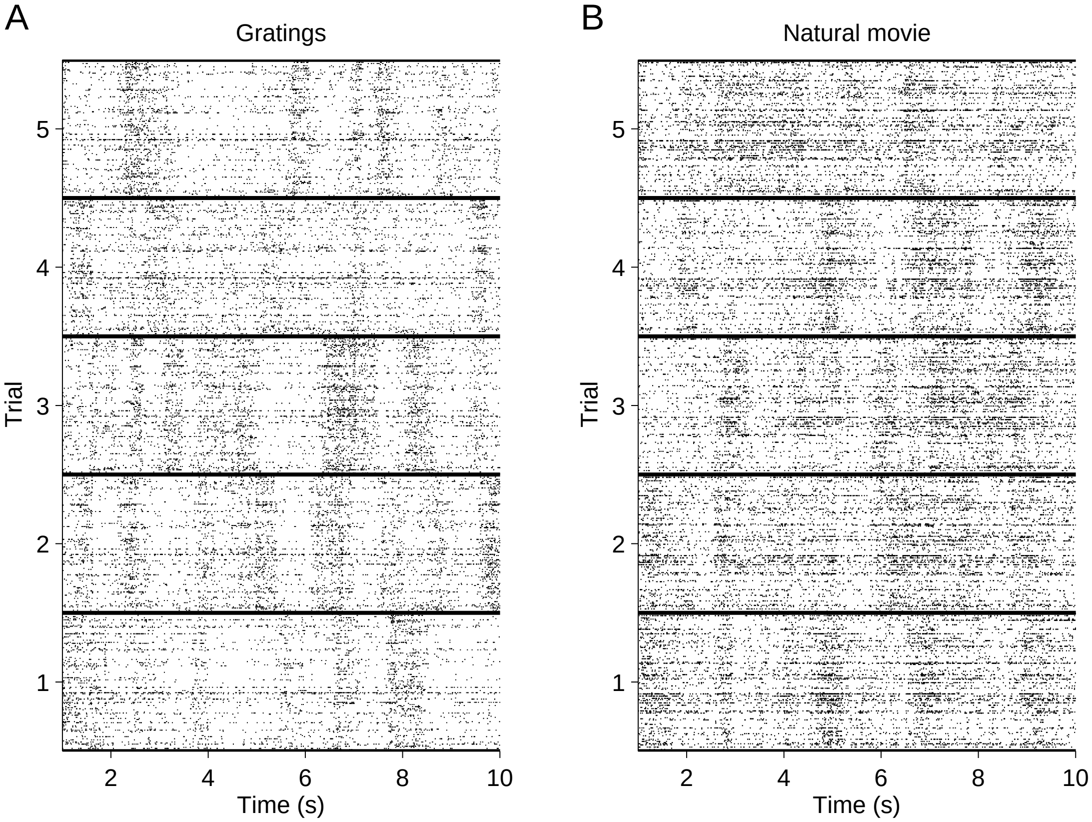

a binary sequence $Y = Y_1 \ldots Y_T$, each value Y_t indicating whether or not the cell fired at time t. According to the Poisson assumption the probability of observing y_t spikes at time t is given by

$$P(Y_T = y_t) = \frac{(r_t\Delta)^{y_t} \exp(-r_t\Delta)}{y_t!} \tag{3.1}$$

where r_t is a rate parameter for the process at time t and $\Delta = 1$ ms. Since y_t is always 0 or 1, the denominator drops out of the equation. The likelihood of observing the entire spike train $Y = y_1 \ldots y_T$ is the product of the likelihoods for each time bin, because of the assumption that these observations are independent:

$$P(Y = y_1 \ldots y_T) = \prod_t (r_t)^{y_t} \exp(-r_t) \tag{3.2}$$

In our context, the rate parameter r is an unobservable property of the neuron and time step, and we proceed by fitting r so that this likelihood value is maximized. Equivalently, and for computational convenience, we can maximize the log-likelihood

$$L = \sum_t^T (y_t \log r_t - r_t) \tag{3.3}$$

We make the assumption that the relationship between the rate r and the observables for any given cell is a linear relationship, followed by a nonlinearity, the exponential function. Paninski (2004) gives the rationale for using this kind of model as a trade-off between neural system faithfulness and computational tractability. The observed components are a network state component and a stimulus component.

$$\log r_t^{(i)} = s_t^{(i)} + \beta^{(i)} x_t^{(i)} \tag{3.4}$$

where $r_t^{(i)}$ is the expected number of spikes at time t from cell i, $s_t^{(i)}$ is the stimulus-dependent component of cell i's firing rate, $x_t^{(i)}$ is an independent variable corresponding to the LFP value (taken to be an indication of the local network activity) at time t, and $\beta^{(i)}$ is a constant which controls the extent to which the network state affects the firing of cell i.

Thus, the values $s_t^{(i)}$ and $\beta^{(i)}$ which maximize the log-likelihood function

$$L^{(i)} = \sum_t^T \left[y_t^{(i)} \left(s_t^{(i)} + \beta^{(i)} x_t^{(i)} \right) - \exp\left(s_t^{(i)} + \beta^{(i)} x_t^{(i)} \right) \right] \tag{3.5}$$

make up the best model of $r_t^{(i)}$ given the data. This is a convex function of $\beta^{(i)}$ and $s^{(i)}$, and we can easily fit it with iteratively reweighted least squares (IRLS), which is equivalent to the Newton-Raphson method (Hardin and Hilbe, 2007) in this context.

As assumed above, $\beta^{(i)}$ is not dependent on the stimulus. Since $s_t^{(i)}$ was just a constant $c^{(i)}$ when the stimulus is constant (a mean gray screen), we fit $\beta^{(i)}$ with spontaneous activity data, which is the simpler formula

$$L^{(i)} = \sum_{t}^{T} \left[y_t^{(i)} \Big(c^{(i)} + \beta^{(i)} x_t^{(i)} \Big) - \exp\Big(c^{(i)} + \beta^{(i)} x_t^{(i)} \Big) \right] \tag{3.6}$$

involving finding the values of only two parameters, $c^{(i)}$ and $\beta^{(i)}$ for each cell i. Larger $|\beta^{(i)}|$ indicates a greater dependence of firing on the value of the LFP.

In Figure 3.3A, the model fits are shown schematically for two example neurons for spontaneous firing (no stimulus parameter). On the left, spikes are shown along with the corresponding LFP from the same electrode. The predicted firing rate function after the fitting procedure is shown on the right along with the actual spike train. The value of β varied across neurons in the population – some cells tended to be more influenced by network state than others. To give context for the values of β, a value $\beta = -0.017$ means that an LFP change of -100 mV predicts a 5.5 fold increase in firing rate. A value $\beta = 0.014$ predicts for the same LFP change, a 4 fold increase in firing rate. The raster plot in Figure 3.3B, sorted by β, demonstrates this trend. LFP value is often linked to negative population spikes, and almost all of the cells show the dependence of negative LFP value on spiking. Neurons in the upper rows of this plot tended to not be very influenced by network state, and thus had low β values. They also tended to have higher firing rates (r =0.48, p <0.0001). Neurons in the lower rows of the plot had a strong tendency to fire during negative inflections of the LFP, and thus had highly negative β values. In the extreme, those neurons tended to fire only during “Up” states.

3.3 Spatial distribution of state dependence

Correlation is known to decrease as the distance between recorded neurons grows (Smith and Kohn, 2008). While LFPs reflect signal from a larger region of tissue, they also tend to cohere more for nearby electrodes than distant ones (Leopold et al., 2003). If the network-driven activity we describe here is one source of correlation between spiking neurons, it is likely to also show a distance dependence. In Figure 3.3, β was computed using the LFP recorded from the same electrode as the spiking activity. Here, we further tested the spatial dependence of spiking on the LFP by pairing each spike train with a single LFP from the array, building a model from each possible pair.

Figure 3.4A and B show the spatial distribution of β for two example neurons. The asterisks indicate the electrode from which spiking activity was recorded for each exam-

Figure 3.3 Description of the model. A: For each cell, $\beta^{(i)}$ is fit using the generalized linear model and spontaneous spiking data, with simultaneous LFP data. B: Cells with low $|\beta^{(i)}|$ are at the top and generally are not driven by the large correlated events. Cells with high $|\beta^{(i)}|$ are at the bottom and are highly susceptible to the network state.

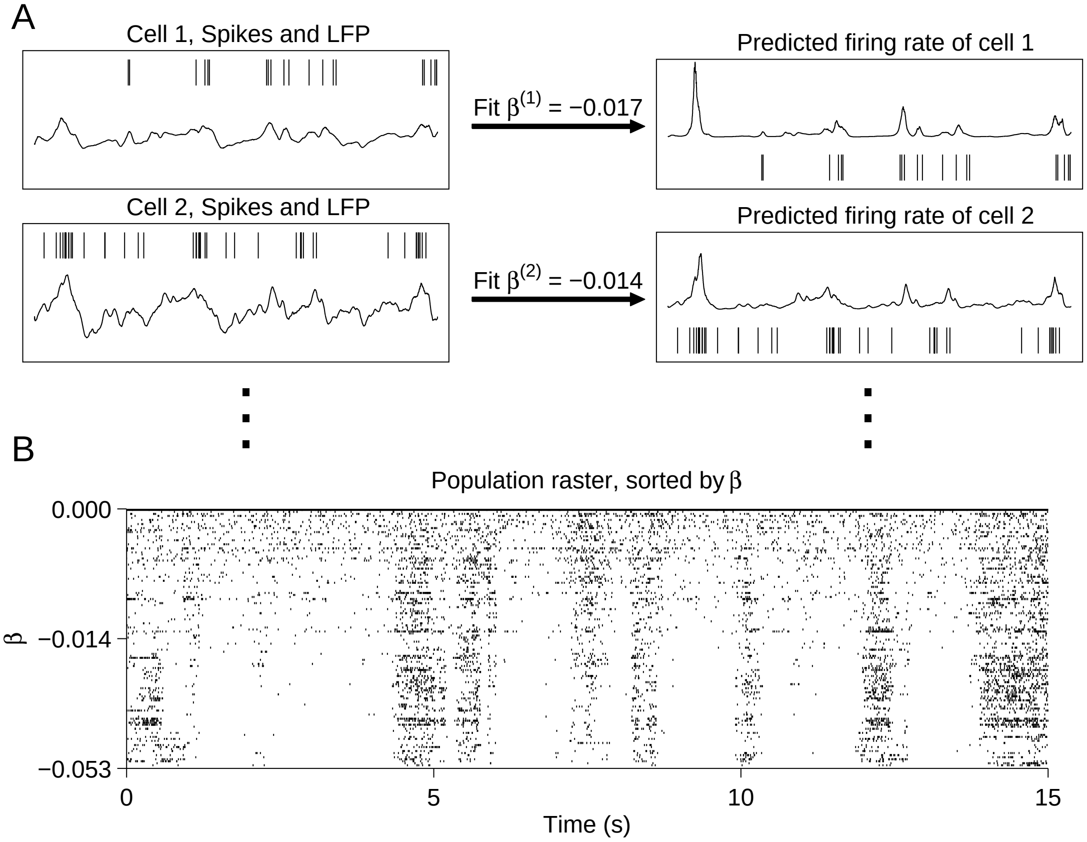

Figure 3.4 Distribution of β. A + B: Examples of β_i for two examples cells. β_i was fit using spontaneous data. These plots depict the 10x10 grid of electrodes on the array. The two cells are recorded from the electrodes labeled with white asterisks. β_i was fit using the LFP from each electrode by itself, and the values are plotted here in the color maps. When β_i is highly negative, negative LFP values from that electrode indicate a higher firing rate of the cell. When β is positive, positive LFP values indicate a higher firing rate. The electrodes closer to the electrode recording the cell's activity tend to carry more information about the cell's firing rates. C: The distribution of β values across the entire population of cells. The data shown in this plot are all possible pairings of cells and LFPs from the same or adjacent electrode. So each cell may be represented up to 9 times in this histogram, depending on its location in the array. For almost all cells, β is negative for nearby electrodes. D: For each cell, β was computed independently using data from each LFP electrode, and grouped into bins based on the distance between the two electrodes. The bar values are the mean values across the cells. There is a smooth falloff of β with increasing distance between the electrodes.

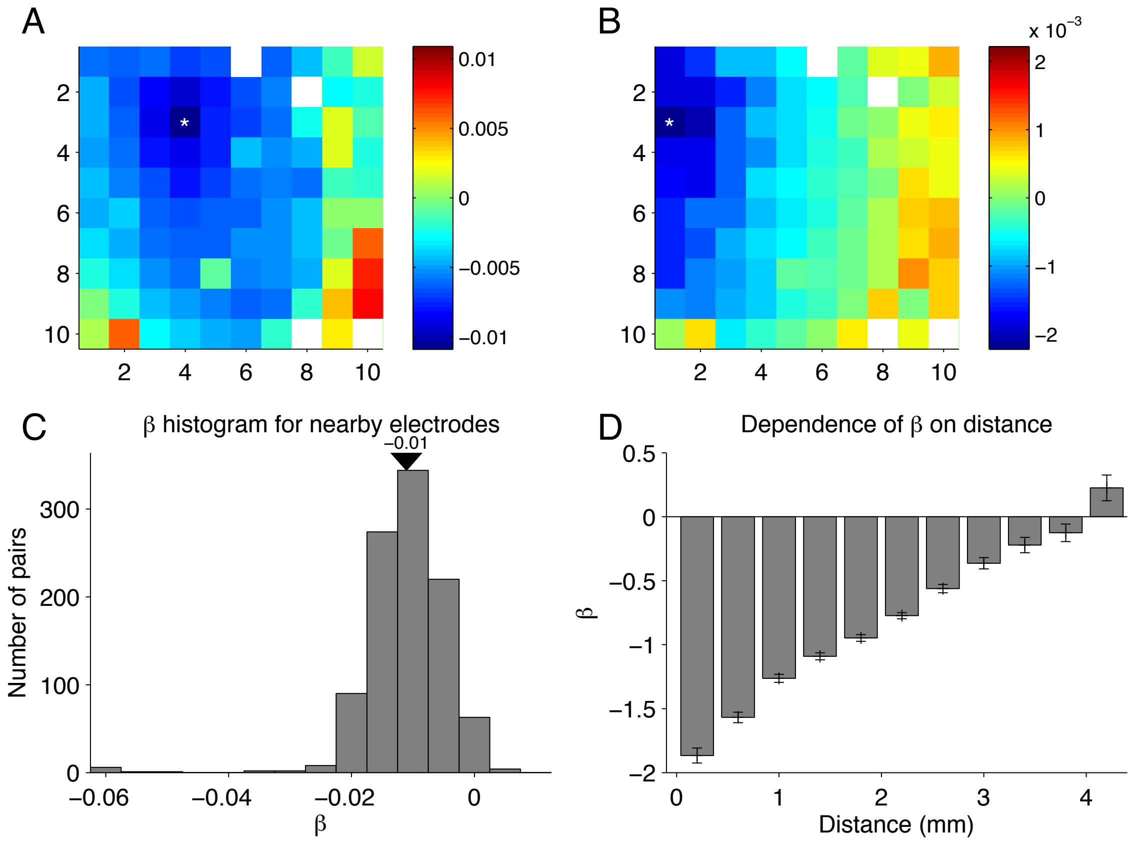

ple. The largest negative values of β, indicated by deep blue colors, were achieved when nearby electrodes supplied the LFP. Stated another way, the spiking activity on a given electrode tends to be most influenced by the LFP of nearby electrodes. The precise spatial distribution of β values varied between cells – in some cases there was a smaller region of high beta values than others. In addition, the overwhelming trend was for β values to be negative around the recording electrode (Figure 3.4C). This reflects the fact that spiking activity tended to occur when the LFP voltages were negative (as seen in the figures above).

To summarize its spatial dependence, we computed the average β for all pairs of spiking electrode and LFP electrode across the entire array. The results of this analysis are shown in Figure 3.4D, which plots average β as a function of the distance between the spiking and LFP electrodes. The largest negative values of β were for the same electrode. β was reduced in magnitude with increasing distance throughout the range in which we could make reliable measurements (4 mm).

3.4 Improvement in orientation selectivity after accounting for state dependence

The observed spiking activity of a neuron in response to a stimulus such as a grating, as we demonstrated above in Figure 3.2A, includes effects of both the stimulus and the network state. Our model factor βx_t is an attempt to assess the influence of the network state on each neuron. Once we determined the value of $\beta^{(i)}$ for each neuron i during spontaneous activity, we assumed that the relationship between spiking and the network state (LFP value $x_t^{(i)}$) remained the same during visual stimulation. We thus fit $s_t^{(i)}$ using the LFP and spiking data from repeated trials of drifting grating recordings, now holding $\beta^{(i)}$ fixed. The expression is

$$\log r_{t,n}^{(i)} = s_t^{(i)} + \beta^{(i)} x_{t,n}^{(i)} \tag{3.7}$$

where $r_{t,n}$ and $x_{t,n}$ are with respect to time and the trial number n, while the stimulus-dependent component $s^{(i)}$ only varies with time, since it is the same on each trial.

One caveat is that during visual stimulation across trials of the same stimulus, the LFP has a significant component of activity which is related to the stimulus. The LFP signal may contain a component of the stimulus related firing, and our goal in this chapter is to remove firing that is independent of the stimulus only, leaving the stimulus dependent activity untouched. We therefore subtracted the mean LFP across repeated trials from each trial's data before computing the fixed offset term $\beta^{(i)} x_t^{(i)}$.

$$\bar{x}_t^{(i)} = \frac{1}{N} \sum_{n}^{N} x_{t,n}^{(i)} \tag{3.8}$$

$$\log r_{t,n}^{(i)} = s_t^{(i)} + \beta^{(i)} [x_{t,n}^{(i)} - \bar{x}_t^{(i)}] \tag{3.9}$$

Figure 3.5A shows some trial data for an example cell.

We solved for $s_t^{(i)}$, and $\exp(s_t^{(i)})$ is the firing rate function with the LFP effect taken into account, in spikes/ms. Figure 3.5B shows the raw peri-stimulus time histogram (PSTH), or $r_t^{(i)}$ in our model, and the LFP-adjusted firing rate function (aPSTH). The aPSTH can be thought of as the stimulus-dependent component of firing, since the component of firing that can be attributed to the LFP, or network effect, has been removed. For points in time which happened to have more network state influence, the aPSTH estimate was very different than the PSTH value, and conversely some time points had a small amount of influence. Even with a large number of trials (N=120), network fluctuations were not evenly distributed in time, a fact that can bias any computed estimate of orientation tuning. Figure 3.5C shows the orientation tuning for this cell, computed both from the PSTH and from the aPSTH. The aPSTH estimate of orientation tuning has a more pronounced difference between preferred and non-preferred orientations, possibly reflecting the removal of action potential contributions that are unrelated to the stimulus. The orientation tuning curves are normalized by their mean firing rate for illustrative purposes.

We characterized the variability of the raw and LFP-adjusted firing by computing Fano factors for each. Specifically, for each neuron we computed the Fano factor (ratio of variance to mean) for each orientation with respect to the spike counts obtained from each repetition of that orientation. Because we found no dependence of the Fano factor on orientation, we averaged across these conditions to produce a single Fano factor for each cell. We then similarly computed the Fano factor among the LFP-adjusted firing rates. Examining the Fano factors across neurons in the two populations shows a substantial and highly significant reduction in variability ($p < 10^{-6}$, paired t-test) in the LFP-adjusted data. Figure 3.5D and E are histograms of the differences between the two variability measures for the two neural populations. For both populations, the LFP-adjusted component tended to have a smaller Fano factor, or more reliability, than the raw spike train. This reduction was not specific to responses evoked with grating stimuli. We performed the same analysis on the natural movie data shown in Figure 3.2 and determined there is also a significant reduction in Fano factor for spikes evoked by this stimulus (mean = -0.32, $p < 10^{-6}$, paired t-test).

Figure 3.5 Using the model to find orientation tuning with the network state removed. A: Data recorded during 4 trials of a single grating movie. The stimulus consisted of drifting gratings of different orientations, ordered randomly. Each orientation was presented for 300 ms. Shown in the plots are the spike trains for each trial and the LFP from the same electrode. The data is used to compute $\exp(s_i(t))$, the component of firing due to the stimulus. It is essentially a LFP-weighted version of the PSTH. B: The firing rate function was calculated by fitting the model for the component of firing due to the stimulus, given a fixed β_i, which were calculated from the spontaneous data as in Figure 3.3. There were 120 trials in total. C: The orientation tuning was calculated by averaging the firing rate function over bins corresponding to the 300 ms grating orientation stimuli epochs. D + E: In the two cell populations for which the grating stimulus was shown, the Fano factors were calculated for the raw spike train and also the model adjusted spike train. Most cells show a Fano factor decrease after the network state is accounted for, indicating a reduction in variability.

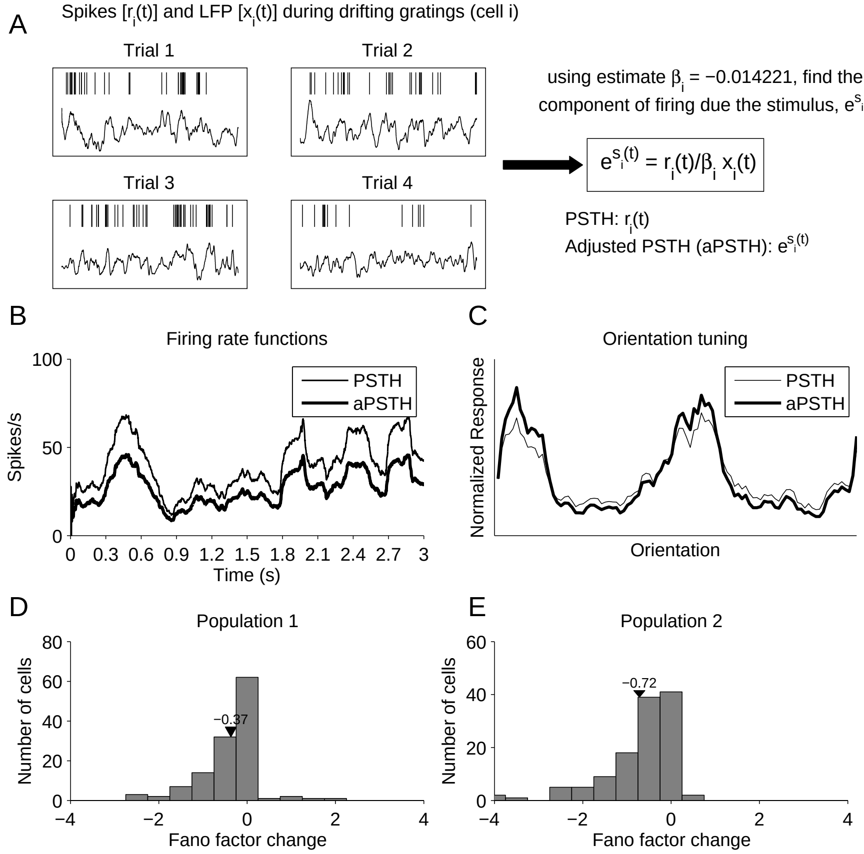

Figure 3.6 Increased orientation selectivity. A+B: Examples for two cells of orientation tuning, computed from the raw firing rate and from the estimate c_i (the firing due to the stimulus). The estimate c_i is computed here using the LFP from the same electrode that recorded the cell's activity. C: Improvement in 2 array populations. For most cells in the populations, selectivity was improved when accounting for the ongoing network activity with the LFP factor. The LFP was from the same electrode that recorded the cell's activity. D: Falloff of improvement with distance in the same 2 populations. Improvement was calculated using the LFP from each electrode, and this histogram shows the average improvement for electrodes at given distances.

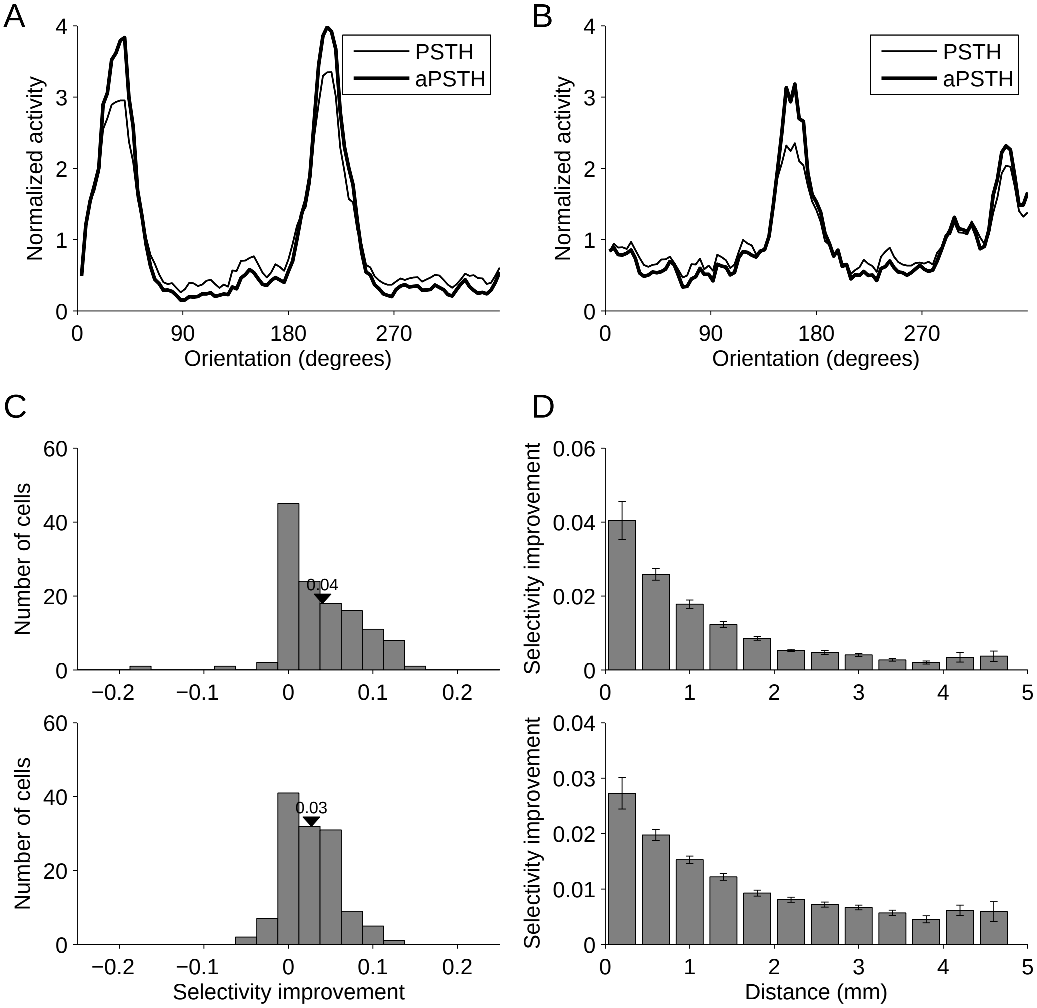

Figure 3.6A and B show the orientation tuning curves measured from two other neurons. In both of these examples, again it is apparent that the orientation selectivity improved after we accounted for network state – the peaks are higher and the troughs are lower. Note that the values on the y axis are relative to the mean firing rate across all conditions, where a value of 1 is exactly the mean firing rate and a value of v is v times the mean firing rate. We evaluated this selectivity change quantitatively using vector averaging:

$$\text{Selectivity} = \frac{|\sum_j \rho_j \exp(2i\theta_j)|}{\sum_j \rho_j} \tag{3.10}$$

θ_j is a specific orientation presented, and ρ_j is the firing rate corresponding to that orientation. $i = \sqrt{-1}$. Selectivity is 1 when the neural firing is concentrated at one or opposite orientations (e.g. $90°$ and $270°$). We found an average improvement of 0.04 (Figure 3.6C), which was statistically significant ($p < 10^{-6}$, paired t-test). This improvement in selectivity was strongest when we used the LFP from the same or nearby electrodes (Figure 3.6D).

We have used the LFP as a signal to reflect network state and account for neuronal variability, and through our model aid in decoding neuronal responses. It is also the case that the spikes themselves could serve as such a signal. Because the LFP has significant differences from spiking activity in terms of spatial extent and tuning selectivity, it was not known whether it would produce better results in our model. We therefore made a direct comparison between the orientation selectivity improvement using the LFP and spike trains in the GLM. We treated each spike train as a time series, and performed smoothing in exactly the same manner as for the LFP time series data. The rest of the analysis was identical, with the smoothed spike train used instead of the LFP as the measure of network state (x_t). In order to be sure that the distances were equal and that sorting errors did not contribute to the shared variability, we used the spike trains from only the neighboring electrodes. We found that at this distance (equivalent to the second bin in Figure 3.6D), the average improvement in selectivity when using spike trains was half the magnitude), significantly lower than what we observed using the LFP (0.013 vs. 0.026, $p < 10^{-4}$, paired t-test).

3.5 Discussion

We recorded spiking activity and the LFP simultaneously from a group of neurons with a microelectrode array implanted in primary visual cortex. We found that large negative fluctuations in the LFP tended to coincide with times of heightened spiking activity, or “Up” states, in neuronal firing. By using the value of the LFP as the indicator of network state, we attempted to separate neuronal responses into stimulus-dependent and state-dependent components. After adjustment for LFP effects the variability of individual neuronal responses was reduced, leading to increased SNR in orientation tuning. This finding demonstrates the value of adjusting firing rates for LFP effects, which are likely due to ongoing network activity rather than a visual stimulus.

Slow, correlated fluctuations in the firing rate of neurons were present in both spontaneous and evoked activity. This type of correlated variability, often measured by the Pearson's correlation between the spike counts of pairs of neurons over many repeats of the same stimulus (r_{sc}), has been previously reported in a number of experiments in both awake and anesthetized animals (Zohary et al., 1994; Shadlen and Newsome, 1998; Bair et al., 2001; Kohn and Smith, 2005; Smith and Kohn, 2008; Huang and Lisberger, 2009). Nonetheless, the visual effect of such correlation on the pattern of spikes in a large neuronal population is quite striking (Fig 3.1A) and has been rarely visualized before.

The epochs of correlated activity, lasting typically 200 to 800 ms with one of the up/down cycles happening every second or two, were highly correlated with large negative peaks in the LFP (Fig 3.1B). This pattern is similar to "Up" and "Down" states, which occur with roughly the same frequency (0.3–1 Hz) and have been reported in a number of different species, cortical areas, and experimental conditions (for review, see Destexhe and Contreras, 2006). While it is not clear that a common mechanism underlies all of these fluctuations in cortical responsivity, it is known that global network states are intimately related to anatomical connectivity, such as among orientation columns (Arieli et al., 1996; Tsodyks et al., 1999). However, while spontaneous activity might reveal the underlying cortical network in which the neurons are embedded, it poses a problem for characterizing cell tuning properties, and for decoding stimulus information based on the spiking activity of the neurons.

The activity of neurons is affected by both the dynamical changes in these cortical states and the tuning-based response to input stimuli. Here, we proposed a simple generalized linear model technique as a first attempt to estimate the contribution of the global cortical state during responses to a visual stimulus. The resulting weighting of the spikes allows a more efficient estimate of the response properties of the neurons, and it demonstrates the relative shortage of stimulus information in the spikes which occur during "Up" states. We used the LFP as an indicator of the network state, a signal which can be obtained simultaneously with spiking activity from the same electrode. We found that variability decreased after accounting for the LFP in both stimulus conditions, gratings and natural movies, demonstrating that this result generalizes. In addition, the LFP is a better indicator of the network state than the spike trains of other neurons, and produces larger decreases in variability using our model. Fluctuations in field potentials have long been known to be related to spiking activity (Eggermont and Smith, 1995; Petersen et al., 2003; Rasch et al., 2008). However, the full relationship between the LFP and spiking activity has been the subject of much recent interest and some controversy (Liu and Newsome, 2006; Berens et al., 2008; Katzner et al., 2009; Xing et al., 2009), and it was not certain that a simple model such as the one presented here could successfully improve the reliability of a stimulus dependent activity measure.

The model makes a number of simplifying assumptions about the relationship between spiking behavior and the LFP, and is limited in its ability to model precise spike timing due to its having only a single parameter β derived from spontaneous activity. It is also likely that this parameter β is somewhat different during stimulation, and fitting β with data acquired during visual stimulation would improve the model. Moreover, it does not allow for modeling the way a visual stimulus could be interacting with the network state: the components of the model are independent. It is known that neuronal response properties, such as receptive field structure (Ringach et al., 2002a; David et al., 2004; Körding et al., 2004), can change depending on the visual stimulus with which they are measured. In our case, we can't be sure that the state-dependence measured from spontaneous activity is the best predictor of state-dependence to gratings, or to other visual stimuli.

Nevertheless, this simple model shows that the LFP can indicate the state of the network, and it takes a significant step toward a true factorization of a spike train into stimulus-dependent and independent components. Our results demonstrate that it is possible to harness the information in the LFP to explicitly decouple these components to a significant extent. The model may be enhanced by incorporating additional effects, including supplementary indicators of the network state such as the full grid of LFP electrode responses, variables identifying high-frequency components of LFP, history effects, effects of other cells, or nonlinear interactions. All such effects could be incorporated as in other applications of generalized linear models (Kass and Ventura, 2001; Pillow, 2007; Pillow and Latham, 2008; Pillow et al., 2008; Paninski et al., 2009).

In this chapter we have laid out a procedure that is generally applicable to neural data which is subject to network state effects on action potential generation. While it was necessary for us to record many neurons and field potentials simultaneously in order to directly observe the population activity fluctuations, our basic finding is a general one that is relevant to single unit recording data. It can be implemented with spikes and LFP from even a single electrode, and does not require a large array. Despite the simplicity of the model, we have shown that using this procedure essentially boosts the signal to noise ratio of the orientation tuning provided by individual neurons. Thus, our findings are a powerful demonstration of the way in which field potential measurements relate to spiking activity. This kind of modeling can be used to compute a stimulus-dependent firing rate estimate in preparation for other computations as well, from receptive field estimation to latency calculations. It is especially appropriate for data with a limited number of trials, which is subject to large trial by trial variations in the effect of the network state. Providing a better model of these spontaneous states and their transitions, as well as further elucidating their origin and the connection with the underlying network, is an important goal of future experimental and theoretical research. In the following chapters we expand on this simple model to more completely model cell firing.

Chapter 4

Computational framework and evaluation

In the previous chapter we showed that simple, 1 parameter GLMs can help to reduce noise in the estimated stimulus dependent firing rate. That model remains too limited, however, since it does not reconcile different predictors of firing rate. That is, it only includes a network state term, which is given by the LFP value, and it does not explicitly model the spatiotemporal receptive field of the cells.

This chapter lays out the computational framework and methods that can support a much larger scale GLM, taking advantage of all the data available from the experimental session. A complete model of neural firing (Figure 4.1), using the same general framework, involves hundreds of thousands of observations and hundreds of model parameters. This model contains more parameters for a given predictor (e.g. the LFP value on multiple electrodes) and uses all the data at our disposal (the stimulus, other cell spikes, and the LFP). This increase in the model size presents a series of computational constraints on processing speed, memory, and storage space. In addition, the spike time series are relatively sparse, so a large model is underconstrained even when fit with a large amount of data. To deal with the data limitation we harness the power of the L1 regularization path algorithm from Park and Hastie (2007). To fit the models as fast as possible we implemented a version of coordinate descent, inspired by a similar implementation in Friedman et al. (2008). We found these methods effective at fitting models using the computational resources available. Here, we present the details of these methods and implementation, as well as our ROC (receiver operating characteristics) based measures for evaluating the comparative performance of the method in modeling spiking activities of the neurons. We establish the validity and effectiveness of these methods and measures with simulated

Figure 4.1 A complete GLM model, with terms corresponding to the stimulus filter, spike coupling terms, and a network state term given by the LFP.

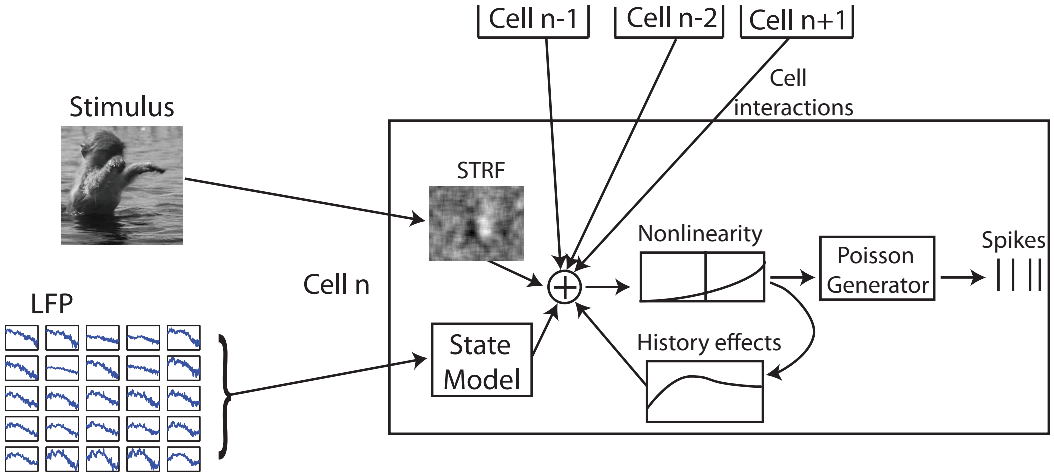

neural data with models of receptive fields and neuronal connectivity.

4.1 Simulating neural spike trains

The simulations we present in this chapter are designed to explore two main aspects of this work. One aspect is the computational feasibility of the methods, which is specifically the time and space required for model fitting on different problem sizes. The other aspect is the ability for the method to yield accurate results on neural data. Moreover, there is a natural trade-off between the accuracy of the model and the computational resources required. Adding more parameters to the model can help in terms of accuracy but will add to the memory requirements and runtime of any fitting methods. We use the following simulations to find a compromise between these factors. In this section we describe the simulation of data, and then in the following section we will attempt to recover these parameters by fitting a GLM to the simulated data.

We draw samples of neural spike trains from the following model:

$$\log P(spike) = \log \mu = \sum_i a_i b_i \tag{4.1}$$

Figure 4.2 An example of a gaussian white noise stimulus in the form $I_{xy}(t)$. The pixel values are chosen independently in time and space.

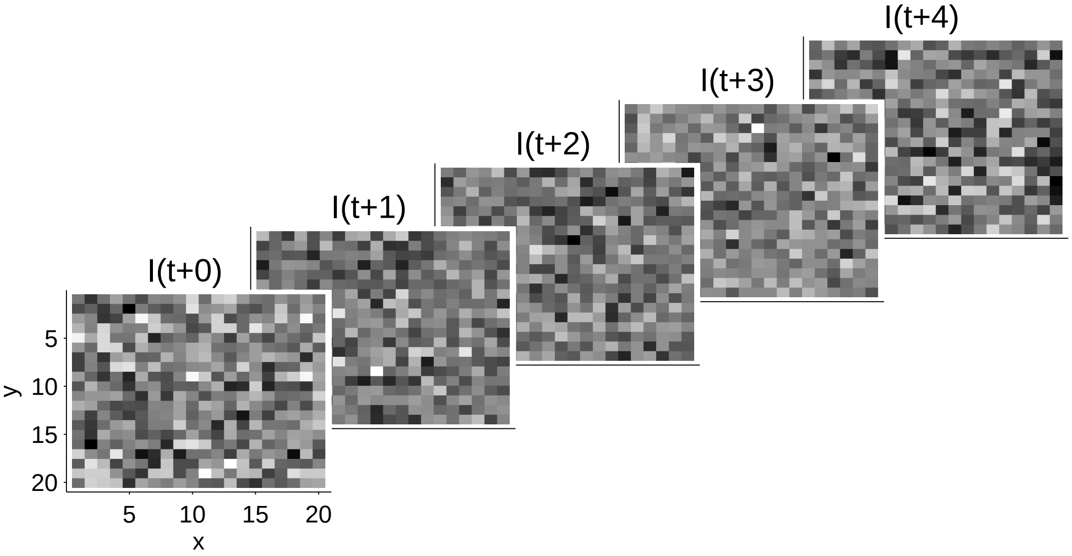

where b_i is a set of parameters corresponding to a combination of any measured potential causes of spiking, i.e. the visual stimulus or other cell inputs. In later chapters, we will build models from three types of terms: the stimulus, spikes from other cells, and network effects. Thus, in the simulations here we explicitly inject these terms into the system:

$$\log P(spike) = \log \mu = \sum_i k_i I_i + \sum_i \alpha_i r_i + \sum \beta_i s_i \tag{4.2}$$

where the three components are the stimulus effect $k_i I_i$, the contributions from history and other cells $\alpha_i r_i$, and the contribution from the network state $\beta_i s_i$. A further specification for these terms follows.

4.1.1 Stimulus effects

The stimulus term $\sum_i k_i I_i$ consists of the actual stimulus image pixel values I_i and the image filter values (or *kernel*) k_i. A V1 cell is generally recognized to be affected by the stimulus over the last few hundred milliseconds, so we can reduce the sum to only take into account these time points. Moreover, V1 cells have a spatially confined receptive field, so we can similarly crop the sum to relevant spatial locations. Rewriting the sum, we have

$$\sum_x \sum_y \sum_\tau k_{xy\tau} I_{xy}(t-\tau) \tag{4.3}$$

where x, y sum over spatial positions and τ over the recent history of the stimulus (Figure 4.2 shows, for a given time t, a sample of the last 5 images). The kernel for the simulated cell has one parameter for each spatio-temporal pixel. We simulated kernels of cells using the following equations, from Dayan and Abbott (2005):

$$LoG(\sigma, x, y) = -\frac{1}{\pi\sigma^4}\frac{1-x^2y^2}{2\sigma^2}\exp\left[\frac{-(x^2+y^2)}{2\sigma^2}\right] \tag{4.4}$$

$$D(\alpha, \tau) = \alpha\exp(-\alpha\tau)\left[\frac{(\alpha\tau)^5}{5!}-\frac{(\alpha\tau)^7}{7!}\right] \tag{4.5}$$

$$k_{xy\tau} = \gamma LoG(\sigma, x_0-x, y_0-y)D(\alpha,\tau) \tag{4.6}$$

Figure 4.3 shows a kernel in the range of parameters we have used for this analysis. We chose these parameters to roughly match the temporal and spatial shape of V1 receptive fields.

4.1.2 Spike effects

This term, $\sum_i \alpha_i r_r$, consists of the influences of the spikes that occurred in the population in the past, and takes into account spikes from the same cell being modeled (history terms) and spikes from other cells. Though many ways exist to model these terms, for these simulations we simply have one term per cell in the population. That is, the summation is over cells, and the term r_i is the actual spike count for some window of time before the current time. For the inputs from other cells, the term α can be either positive or negative, reflecting excitatory or inhibitory input, respectively. For the history term, α is taken to be negative, simulating a reduction in firing rate following spiking, or refractory period. It is worth noting that this is a very simple conception of functional connectivity, and it is trivial to model more complex dynamics within this framework using splines or kernel methods as Section 4.1.1 illustrates. Figure 4.4 shows some examples of these terms in a small network.

4.1.3 Network effects

In addition to stimulus effects and influences from other cells, we simulated a shared noise component $\sum_i \beta_i s_i$ which can be conceptualized as the network state effect. This term

Figure 4.3 A single kernel generated from Eq 4.6. Parameters used here are $\gamma = 0.077, \alpha = 0.12, \sigma = 0.85, x_0 = 1.23, y_0 = -1.43$. Shown here are temporal snapshots of the kernel in space, and below is the temporal profile of the peak spatial kernel location.

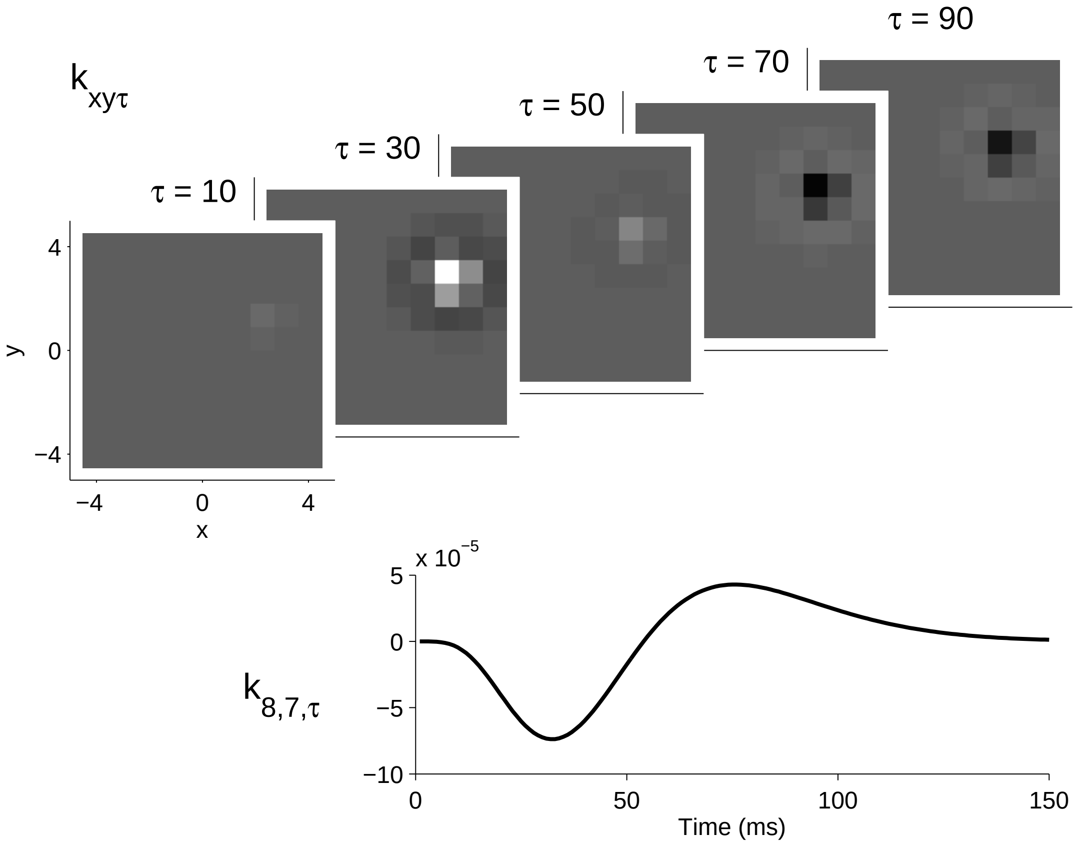

Figure 4.4 For a population of three simulated cells, each of the cells has an associated function $r_i(t)$ which is the input to the simulation, multiplied by a constant α_i. Here, the $r_i(t)$ alone is depicted.

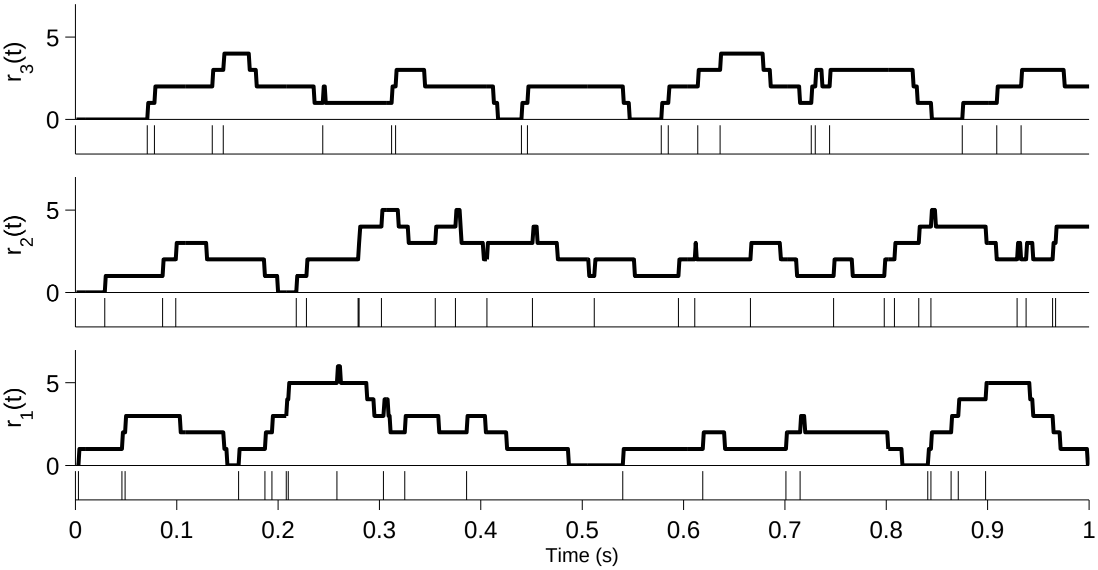

Figure 4.5 Two examples of the simulated network state component, low-pass filtered at 10Hz with a Butterworth filter.

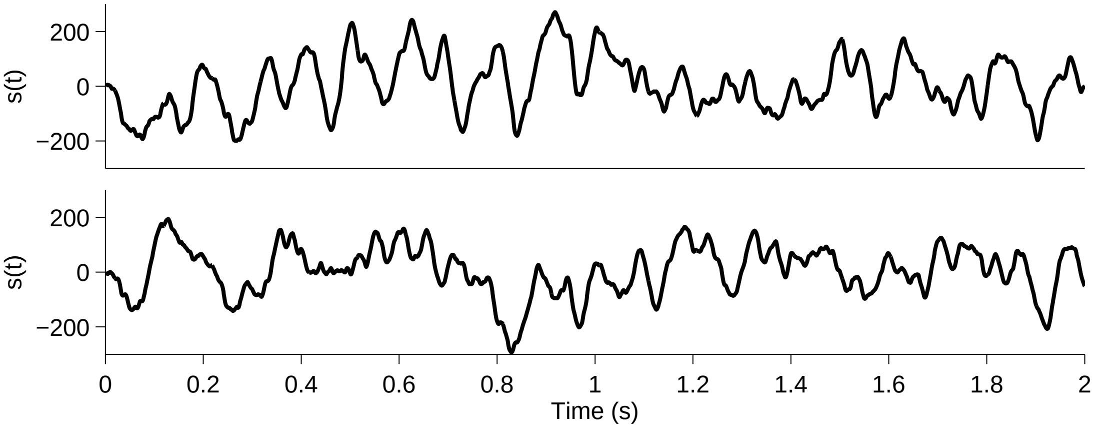

is shared among all cells in the population, although each cell has an individual β_i which weights the network state effect. Thus, some cells can be more affected by the network state than others, even inversely. We modeled the network state effect as a slowly varying signal, given by a gaussian noise time series sampled at 1ms resolution and then low-pass filtered. Examples of the signal are given in Figure 4.5.

4.1.4 Simulation of spike trains

Putting together all the above expressions and methods, we can compute the expected number of spikes at each time t, $\mu(t)$.

$$\log \mu(t) = \sum_x \sum_y \sum_\tau k_{xy\tau} I_{xy}(t-\tau) + \sum_i \sum_\tau \alpha_i r_i(t-\tau) + \beta s(t) \tag{4.7}$$

We determine whether or not a spike occurs at time t by sampling from a Poisson distribution with parameter $\mu(t)$. Since in real data there is a hard refractory period (we never actually observe more than one spike in each 1ms interval), we clamp the samples to be either 0 or 1, meaning there can be no more than one spike per millisecond.

Figure 4.6A-C shows some examples of simulated spike trains from different restricted models. Stimulus effects are repeated across trials of the same stimulus, but the network effects and spike effects are not repeatable with trials of the same stimulus. Figure 4.6D shows examples of data generated using all three types of effects as in Eq 4.7.

To demonstrate that this simulation is a reasonable model of spiking activity, we can also compute typical metrics of spike trains, like the cross-correlation (Figure 4.7) and the spike-triggered average (Figure 4.8). These produce similar results to the receptive fields and cross-correlograms shown in Chapter 5.

4.2 Fitting models

The above illustrates how to move from a model of neural firing to simulated spike trains, which is relatively simple. In the rest of this chapter we give the foundation for a reverse method, recovering the coefficients of such a model from the spike trains. In this scenario, we have data consisting of the spike trains themselves and also the associated stimuli and other recorded phenomena (for us, the LFP is such an associated signal). We model the spike train, as before, with

$$f(y;\mu) = \frac{\mu^y \exp(-\mu)}{y!} \tag{4.8}$$

Figure 4.6 Examples of simulated cell firing. A-C: The three simulation conditions given in the above sections: stimulus only, cell influences only, and network state only. In B, the only influences present are from cell 1 to all the other cells, with $\alpha = .6$. In C, the state affects all cells equally, each with $\beta = .01$. D: All three conditions are present in this simulation.

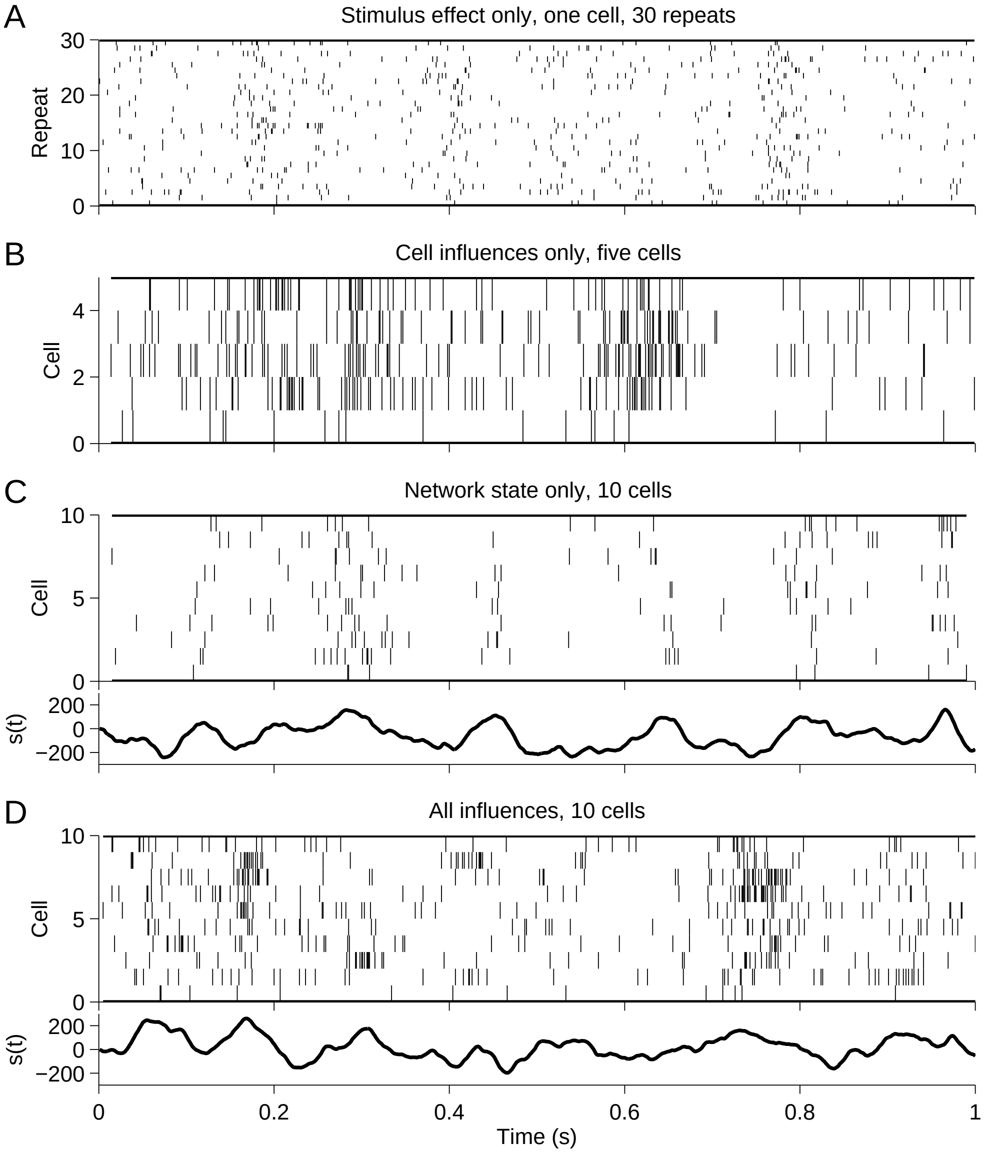

Figure 4.7 Shuffled-corrected cross-correlograms for a variety of simulated cells. The simulation used the parameters presented at the top, which consisted of cells 2 and 3 impacted by the firing of cell 1, and cell 4 and 5 under the influence of the same network state. All cells had receptive fields within a small area which are not shown here. Below, it is apparent that the cross correlation was strong and shifted from 0 for 1*2, and centered and strong for 2*3. The network effect caused a significant cross-correlation for 4*5. No correlation is apparent in 2*4, as expected. The shuffle correction consists of the subtraction of a cross-correlogram which is computed with non-simultaneous data on the two cells. Thus, any stimulus effect (repeated effect) is removed.

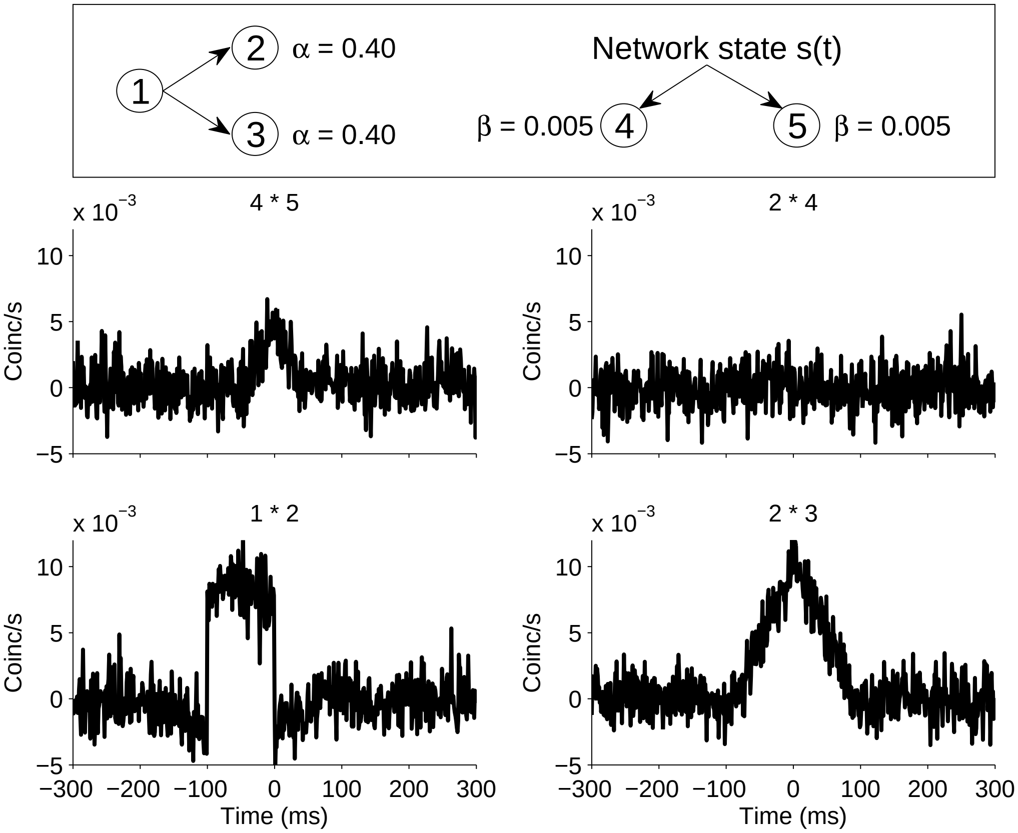

Figure 4.8 For the same simulation shown in Figure 4.7, the spike-triggered averages (STA) for cells 1 and 2 at two times lags, $\tau = 40, 80$. Above are the corresponding ground-truth kernels at those same times. Effects of the receptive field of cell 1 on the STA of cell 2 are visible, due to their connectivity.

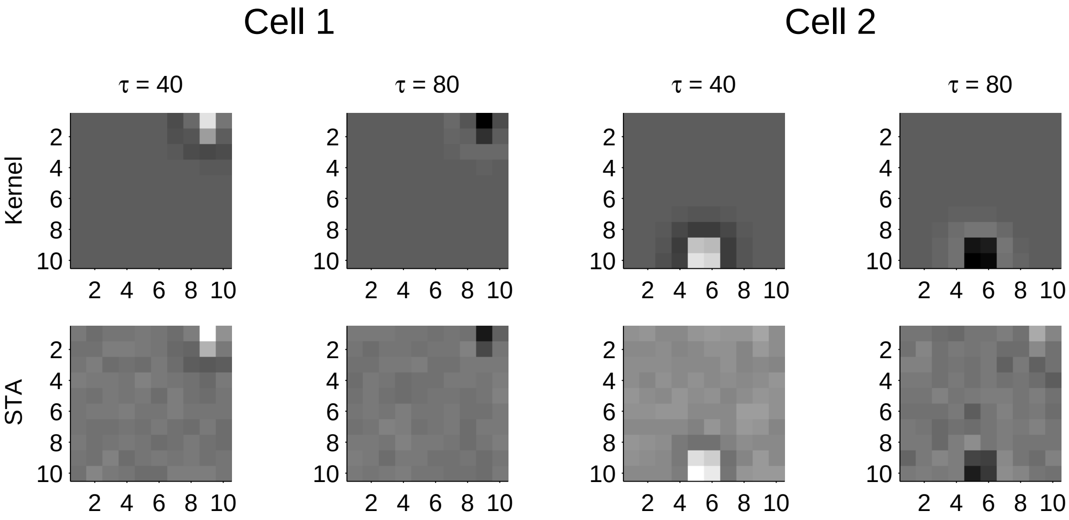

Here, $f(y;\mu)$ is the probability of observing y occurrences of an event in some window of time, and the parameter μ is the expected number of occurrences in that same window.

We model the firing of a cell over time, given the parameters of the stimulus and other observations. To this end, we characterize μ as a function in time, $\mu(t)$, and thus the likelihood of seeing all the responses $Y = y_1 \dots y_T$, where y_t is the number of spikes observed in time window t, is

$$F(Y,\mu) = \prod_i^T \frac{\mu(t)^{y_t} \exp(-\mu(t))}{y_t!} \tag{4.9}$$

The goal is to find the function $\mu(t)$ such that L is maximized. To make the fitting tractable, we define the function $\mu(t)$ as the exponential of a linear combination of some data, the same as the formulation above:

$$\log \mu(t) = \sum_x \sum_y \sum_\tau k_{xy\tau} I_{xy}(t-\tau) + \sum_i \alpha_i r_i(t) + \sum_i \beta_i s_i(t) \tag{4.10}$$

We can equivalently maximize $L = \log F$, since $\log$ is monotonic. The log-likelihood function is

$$L(Y,\mu) = \sum_t^T \log \frac{\mu(t)^{y_t} \exp(-\mu(t))}{y_t!} = \sum_t^T (y_t \log \mu(t) - \mu(t) - \log y_t!) \tag{4.11}$$

We can neglect the constant term $\log y_i!$ in the maximization. This formulation fits within the generalized linear model framework as an example of Poisson regression with the canonical (log) link function. So the parameters $\beta_i, \alpha_i, k_{xy\tau}$ which maximize L are the maximum likelihood estimate for the cell, given the data x_i and y_i.

4.2.1 Standard GLM fitting

To fit the parameters $\theta = \{\beta_i, \alpha_i, k_{xy\tau}\}$we can use any convex nonlinear optimization approach. First, we define V to be a $T \times N$ matrix of variables we believe can impact the firing rate of a cell, where each row t of V is $v_1^{(t)} \dots v_N^{(t)}$, which are the collection of observables I, r, s, from equation 4.10.

Here we lay out the procedure for iteratively reweighted least squares (IRLS) which for our problem is equivalent to the Newton-Raphson method. This method proceeds by ascending or descending a function to find the stationary point, which we know is unique because of the convexity of the function. The values θ_i are iteratively approximated until convergence as follows:

$$\theta^{(i+1)} = \theta^{(i)} - H(L(Y,\mu))^{-1}\nabla L(Y,\mu) \tag{4.12}$$

where $H(L(Y,\mu))$ is the Hessian of the log-likelihood function and $\nabla L(Y,\mu)$ is the gradient of the function. We define W to be the diagonal matrix

$$\begin{aligned} W_i, j = &\quad \mu(i) = \exp(\textstyle\sum_k^N \theta_k v_k^{(i)}) \quad \text{if } i = j & (4.13)\\ = &\quad 0 \quad \text{otherwise} & (4.14)\end{aligned}$$

The hessian and gradient are given by

$$H(L(Y,\mu)) = -V^T W V \tag{4.15}$$

$$\nabla L(Y,\mu) = V^T(Y - \mu) \tag{4.16}$$

4.2.2 Regularized GLM fitting

The previous method works well and efficiently by maximizing the likelihood of the model using second order approximations, but it suffers from a serious problem. The kind of neural data we have collected typically has a likelihood function which is relatively flat near its minimum. Part of the reason for this is a sampling problem: there simply are not enough spikes to locate the true parameters. To solve this overfitting problem, we take the approach of regularizing the GLMs. Two possibilities are L1 and L2 regularizations, which in our context are penalties applied to the log-likelihood function:

$$L(Y,\mu) + \lambda_2 \sum_j^p \theta_j^2 + \lambda_1 \sum_j^p |\theta| \tag{4.17}$$

The L1 penalty term is particularly important to us here, because it reduces some of the coefficients of model parameters to identically zero, creating a sparse model. However, fitting a generalized linear model to models that include an L1 penalty is computationally difficult, because the function is no longer differentiable (when coefficients are zero). The above version of Newton's method is only guaranteed to converge on differentiable functions. Friedman et al. (2008) show how coordinate descent can successfully perform logistic regression on functions with L1 penalties. This method avoids a costly line search, and is capable of computing the solution along the whole path of an elastic net penalty term. Below, we derive a similar method for Poisson regression in an analogous way.

As above, the log-likelihood can be written

$$L(\theta) = \sum_{i}^{T}(y_i \log \mu(i) - \mu(i) - \log y_i!) = \sum_{i}^{T}(y_i \theta V_i - \exp(\theta V_i) - \log y_i!) \tag{4.18}$$

and we would like to find

$$\min_{\theta \in \mathbb{R}} \left[\sum_{i}^{T}(-y_i \theta V_i + \exp(\theta V_i) + \log y_i!) + \lambda P_\phi(\theta) \right] \tag{4.19}$$

where $P_\phi(\theta)$ is an elastic-net penalty, which is a compromise between L2 and L1 penalties, with the amount of compromise dictated by the value of ϕ. $(0 \leq \phi \leq 1)$

$$P_\phi(\theta) = \sum_{j=1}^{p} \frac{1}{2}(1-\phi)\theta_j^2 + \phi|\theta_j| \tag{4.20}$$

We approximate the left part of equation 4.19 with a quadratic Taylor series expansion around the current estimate $\tilde{\theta}$:

$$L(\theta) \approx L(\tilde{\theta}) + \sum_{j=1}^{p}(\theta_j - \tilde{\theta}_j)L_{\theta_j}(\tilde{\theta}) + \frac{1}{2}\sum_{j=1}^{p}\sum_{k=1}^{p}(\theta_j - \tilde{\theta}_j)(\theta_k - \tilde{\theta}_k)L_{\theta_j\theta_k}(\tilde{\theta}) \tag{4.21}$$

where $L_{\theta_j}(\tilde{\theta})$ and $L_{\theta_j\theta_k}(\tilde{\theta})$ are the first and second partial derivatives of the log-likelihood L. They are given by

$$L(\tilde{\theta}) = \sum_{i}^{N}(y_i \tilde{\theta} V_i - \exp(\tilde{\theta} V_i) - \log y_i!) = \sum_{i}^{N}(y_i \log \tilde{\mu}_i - \tilde{\mu}_i - \log y_i!) \tag{4.22}$$

$$L_{\theta_j}(\tilde{\theta}) = \sum_{i}^{N}(y_i v_{ij} - v_{ij}\exp(\tilde{\theta} V_i)) = \sum_{i}^{N} v_{ij}(y_i - \tilde{\mu}_i) \tag{4.23}$$

$$L_{\theta_j\theta_k}(\tilde{\theta}) = \sum_{i}^{N}(-v_{ij}v_{ik}\exp(\tilde{\theta} V_i)) = -\sum_{i}^{N} v_{ij}v_{ik}\tilde{\mu}_i \tag{4.24}$$

$$
\begin{aligned}
L(\theta) \approx L_Q(\theta) &= \sum_i^N \Big[y_i \log \tilde{\mu}_i - \tilde{\mu}_i - \log y_i! + \sum_{j=1}^p v_{ij}(\theta_j - \tilde{\theta}_j)(y_i - \tilde{\mu}_i) + \\
& - \frac{\tilde{\mu}_i}{2} \sum_{j=1}^p \sum_{k=1}^p v_{ij} v_{ik} (\theta_j - \tilde{\theta}_j)(\theta_k - \tilde{\theta}_k) \Big] && (4.25) \\
&= \sum_i^N \left[y_i \log \tilde{\mu}_i - \tilde{\mu}_i - \log y_i! + \sum_{j=1}^p \Big(v_{ij}\theta_j y_i - v_{ij}\theta_j \tilde{\mu}_i - v_{ij}\tilde{\theta}_j y_i + v_{ij}\tilde{\theta}_j \tilde{\mu}_i \Big) + \right. \\
& \left. - \frac{\tilde{\mu}_i}{2} \left(\sum_{j=1}^p v_{ij}(\theta_j - \tilde{\theta}_j) \right)^2 \right] && (4.26) \\
&= \sum_i^N \left[y_i \log \tilde{\mu}_i - \tilde{\mu}_i - \log y_i! + (y_i - \tilde{\mu}_i)\theta V_i - y_i \log \tilde{\mu}_i + \tilde{\mu}_i \log \tilde{\mu}_i + \right. \\
& \left. - \frac{\tilde{\mu}_i}{2} (\theta V_i - \log \tilde{\mu}_i)^2 \right] && (4.27) \\
&= \sum_i^N \left[-\tilde{\mu}_i - \log y_i! + (y_i - \tilde{\mu}_i + \tilde{\mu}_i \log \tilde{\mu}_i)\theta V_i - \frac{\tilde{\mu}_i}{2} (\theta V_i)^2 \right] && (4.28)
\end{aligned}
$$

Substituting this approximation to the log-likelihood gives the expression we would like to minimize:

$$R = -L_Q(\theta) + \lambda P_\phi(\theta) \tag{4.29}$$

Given an estimate of θ, a coordinate descent step amounts to the minimization of this expression with respect to θ_j, for $j \in 1 \ldots p$.

For $\tilde{\theta}_j > 0$,

$$
\begin{aligned}
\frac{\partial R}{\partial \theta_j} &= \sum_i^N \left[-v_{ij}(y_i - \tilde{\mu}_i + \tilde{\mu}_i \log \tilde{\mu}_i) + \tilde{\mu}_i v_{ij}(\theta V_i) \right] + \lambda(1-\phi)\theta_j + \lambda\phi \\
&= \omega_j + (\lambda(1-\phi) + \sum_i^N \tilde{\mu}_i v_{ij}^2)\theta_j + \lambda\phi && (4.30)
\end{aligned}
$$

where

$$\omega_j = \sum_i^N v_{ij}\left(-y_i + \tilde{\mu}_i - \tilde{\mu}_i \log \tilde{\mu}_i + \tilde{\mu}_i \sum_{k \neq j} v_{ik}\theta_k\right) \tag{4.31}$$

$$= \sum_i^N v_{ij}\left(-y_i + \tilde{\mu}_i - \tilde{\mu}_i(v_{ij}\theta_j)\right) \tag{4.32}$$

For $\tilde{\theta}_j < 0$,

$$\frac{\partial R}{\partial \theta_j} = \sum_i^N [-v_{ij}(y_i - \tilde{\mu}_i + \tilde{\mu}_i \log \tilde{\mu}_i) + \tilde{\mu}_i v_{ij}(\theta V_i)] + \lambda(1-\phi)\theta_j - \lambda\phi$$

$$= \omega_j + (\lambda(1-\phi) + \sum_i^N \tilde{\mu}_i v_{ij}^2)\theta_j - \lambda\phi \tag{4.33}$$

These are linear functions with positive slopes, and a discontinuity at $\theta_j = 0$. When $-\lambda\phi < \omega_j < \lambda\phi$, there is no zero crossing; the function R decreases as θ_j increases toward 0, and reaches a minimum at $\theta_j = 0$, after which point it increases unbounded. Alternatively, when $|\omega_j| \geq \lambda\phi$, $\frac{\partial R}{\partial \theta_j} = 0$ when

$$-(\omega_j - \lambda\phi)/(\lambda(1-\phi) + \sum_i^N \tilde{\mu}_i v_{ij}^2), \quad \text{for } \omega_j \geq \lambda\phi \tag{4.34}$$

$$-(\omega_j + \lambda\phi)/(\lambda(1-\phi) + \sum_i^N \tilde{\mu}_i v_{ij}^2), \quad \text{for } \omega_j \leq \lambda\phi \tag{4.35}$$

4.2.3 Regularization path

To efficiently choose the proper penalty which avoids overfitting we implemented a regularization path algorithm, given by Park and Hastie (2007) and in the coordinate descent context by Friedman et al. (2008). The algorithm proceeds by performing fits of the same kind described above with an elastic net regularization term. Instead of just performing the fit with a given λ, it computes all the fits for the whole λ path.

We begin with λ large enough so that all coefficients are dominated by the regularization, and hence 0 for this value of the penalty. In the coordinate descent method, for very large λ and $\phi > 0$, $-\lambda\phi < \omega_j < \lambda\phi$ for all j, where ω_j is given by Eq 4.32. As λ is reduced, some coefficient j will be the first of the set such that $|\omega_j| = \lambda\phi$.

$$\phi\lambda_{\text{max}} = \max_j |\omega_j| \tag{4.36}$$

At this point the "active set" $A^{(0)}$ is empty, where $\lambda^{(0)} = \lambda_{\text{max}}$. We then repeat the following steps until we reach some stopping criterion, which may be a minimum λ value or a cross validation constraint. The coordinates $V^{(0)} = \{v_j\}$ are all 0 at this point.

Iteration i

- Set $\lambda^{(i)} = \lambda^{(i-1)}/c$, where c is chosen to give a desired number of total log-steps for λ.
- Optimize using coordinate descent with penalty term $\lambda^{(i)}$, using $V^{(i-1)}$ as a warm start. We start $A^{(i)} = 1 \ldots p$, the full set of coordinates. Each time a coordinate v_j is set to 0, we remove it from $A^{(i)}$.
- Now we want to make sure that no terms that have been dropped from the active set should actually be in the model. Set the active set back to $1 \ldots p$, and rerun coordinate descent on the full active set, using the coordinate values $V^{(i)}$ that were obtained from the last step. If the active set is the same as after the previous step, we are done: the function has converged. Otherwise, a parameter was removed from the active set that actually belongs there. Take this new, larger active set and go back to the previous step using it.

Figure 4.9 shows an example of fitting parameters using the coordinate descent method.

4.2.4 Stimulus remapping

For the kind of stimulus we are using, there is a large amount of correlation at millisecond precision. Thus, we have required 40-50 components (one for each millisecond of the recovered kernel) to accurately represent the true kernel. It would be much more efficient, and potentially smoother, to instead represent the kernel as a sum of gaussian bumps of different width and temporal location. To show this, we have transformed the stimulus values into values in a space of gaussian bumps. The gaussian bumps were represented by

$$g_i(x, y, \tau) = \exp\left(\frac{-(\tau - \tau_i)^2}{2\sigma_1^2} + \frac{-(x - x_i)^2}{2\sigma_2^2} + \frac{-(y - y_i)^2}{2\sigma_3^2}\right) \tag{4.37}$$

Figure 4.9 Example of coordinate descent using a regularization path. The kernel at $\tau = 30$ is shown at the top. Below are fitted parameters for the same τ in 6 steps of the regularization path, for different values of λ. The λ values and active set sizes throughout the progression of the algorithm are shown at the bottom.

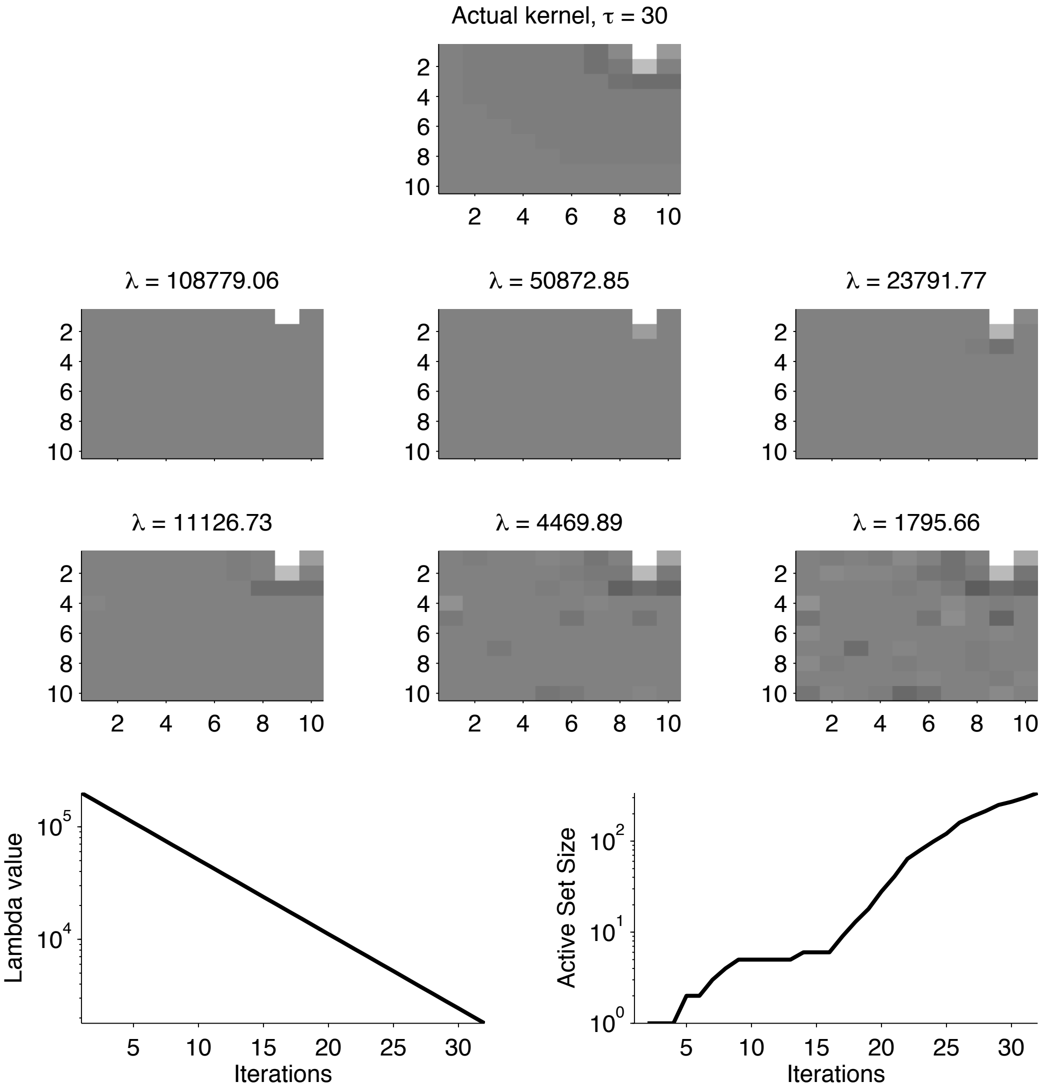

The stimulus is X, which is a $N \times T$, where N is the number of time points in the kernel. H and W are the height and width of the visual stimulus. We transformed the stimulus with $Y = GX$, where G is the matrix of all the vectorized g_i functions. G has size $M \times N$, where M is the number of gaussian bump functions g_i. M can be any chosen number of gaussian functions here, and the set Y has size $M \times T$.

We can get the corresponding filter in the original space of pixels and time points by the following logic:

$$\log \mu(t) = \sum_i^M \beta_i Y_{i,t} = \sum_i^M \beta_i \sum_j^N G_{i,j} X_{j,t} \tag{4.38}$$

Moving the summations around:

$$\sum_i^M \beta_i \sum_j^N G_{i,j} X_{j,t} = \sum_j^N X_{j,t} \sum_i^M \beta_i G_{i,j} \tag{4.39}$$

Thus the quantities $\sum_i^M \beta_i G_{i,j}$ are the filters in the original space. In chapter 5 we use this transformation in the spatial domain as well due to the spatial correlations in the stimulus used there.

4.3 Assessing the models

Figure 4.9 shows various points in the regularization path, and it is easy to see that the model beings by underfitting the data and progresses through the path until it is finally overfitting the data, using pixels that are completely irrelevant to the true receptive field to predict spikes. It is important that we can both assess these fits, and also halt the path algorithm before overfitting occurs.

To quantitatively assess the model fits, we employ an ROC procedure (Hatsopoulos et al., 2007). For each model fit, the firing rate function is $u(t)$, given by Eq 4.7. To compute the ROC curve based on $\mu(t)$, we first create a thresholded version of $\mu(t)$ which serves as the prediction of spiking:

$$\hat{r}_c(t) = 1 \text{ if } \mu(t) \geq c \tag{4.40}$$

$$0 \text{ if } \mu(t) < c \tag{4.41}$$

For each fixed threshold c, a point on the ROC curve is the ratio of the true positive rate (TPR) to the false positive rate (FPR), given by comparison to the actual spikes recorded,

$r(t)$. Both of these are binary time series functions, so TPR and FPR are defined as:

$$\text{TPR} = \frac{1}{\sum_t r(t)} \sum_t^T r(t)\hat{r}_c(t) \tag{4.42}$$

$$\text{FPR} = \frac{1}{\sum_t (1 - r(t))} \sum_t^T (1 - r(t))\hat{r}_c(t) \tag{4.43}$$

An example of such a curve is shown in Figure 4.10B. The true value of these models lies in their ability to predict data unused in training. Figure 4.10C shows how the ROC curve looks at different points in the path algorithm.

A standard approach to finding an appropriate penalty term is to use 10-fold cross validation, holding out 10% of the data for testing and training on the rest of the data. The model fits are then computed on each of the 10 partitions separately. This kind of cross-validation is more robust to data with outliers and fluctuations. Figure 4.11 shows the test results from a 10-fold cross valid ation run. The peaks in the curves correspond to the predicted optimal values for the regularization parameter λ.

Figure 4.10 ROC example. A: A simulated kernel with 3 distinct fits in the regularization path, chosen to illustrate underfitting, overfitting, and good fitting. These fits are with the parameterization of the pixel values, not with Gaussian smoothing. B: The ROC curves corresponding to the 3 panels in A. C: The area until the ROC curve, as a function of iteration in the regularization path. λ decreases by a step on a log scale with each iteration. The 3 fits illustrated in A and B are indicated with lines.

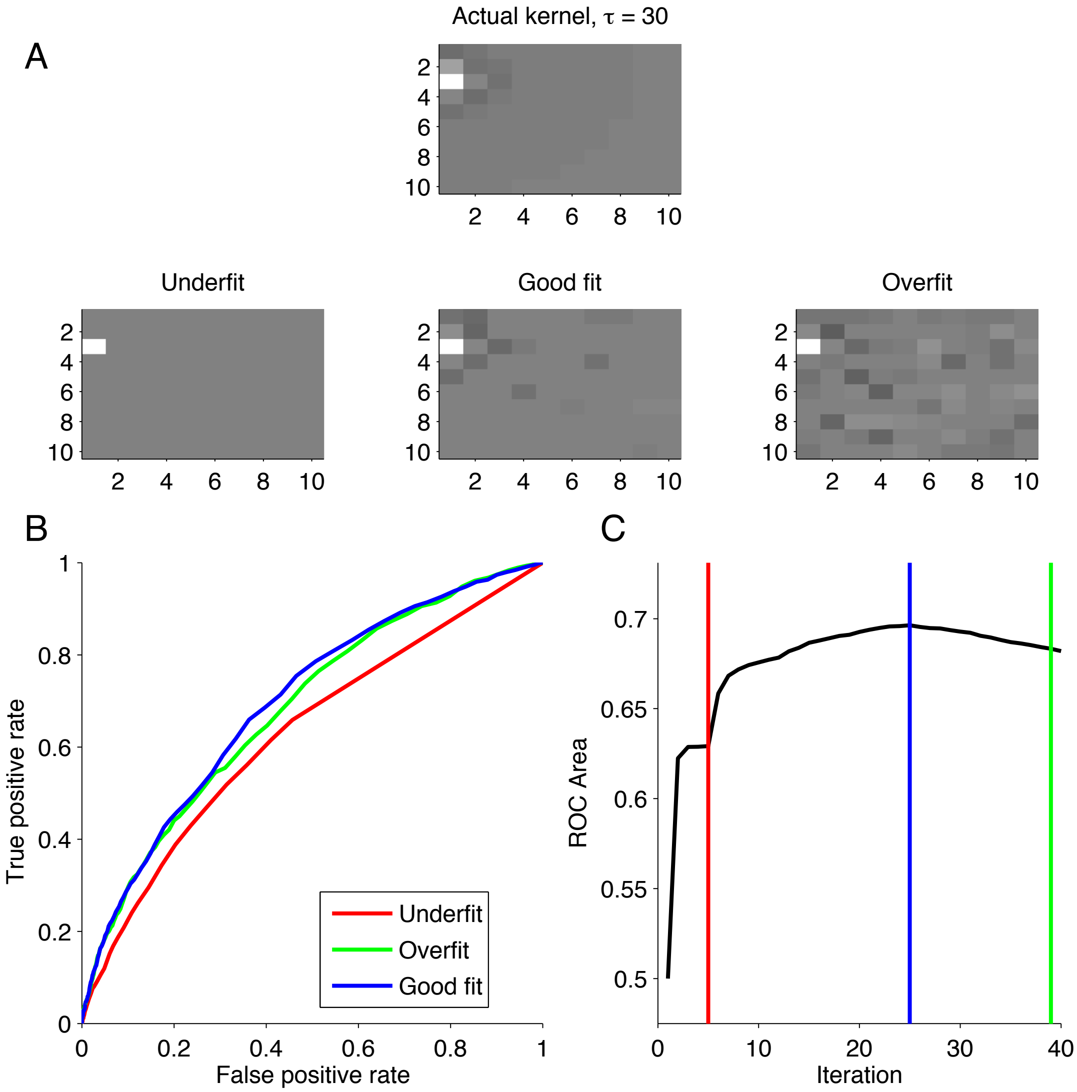

Figure 4.11 10-fold cross validation. 10 curves are shown here, each corresponding to a unique run of the cross validation procedure. The highest value on the curves corresponds to the best model. We can generally choose the penalty corresponding to the maximum of the mean of the 10 curves.

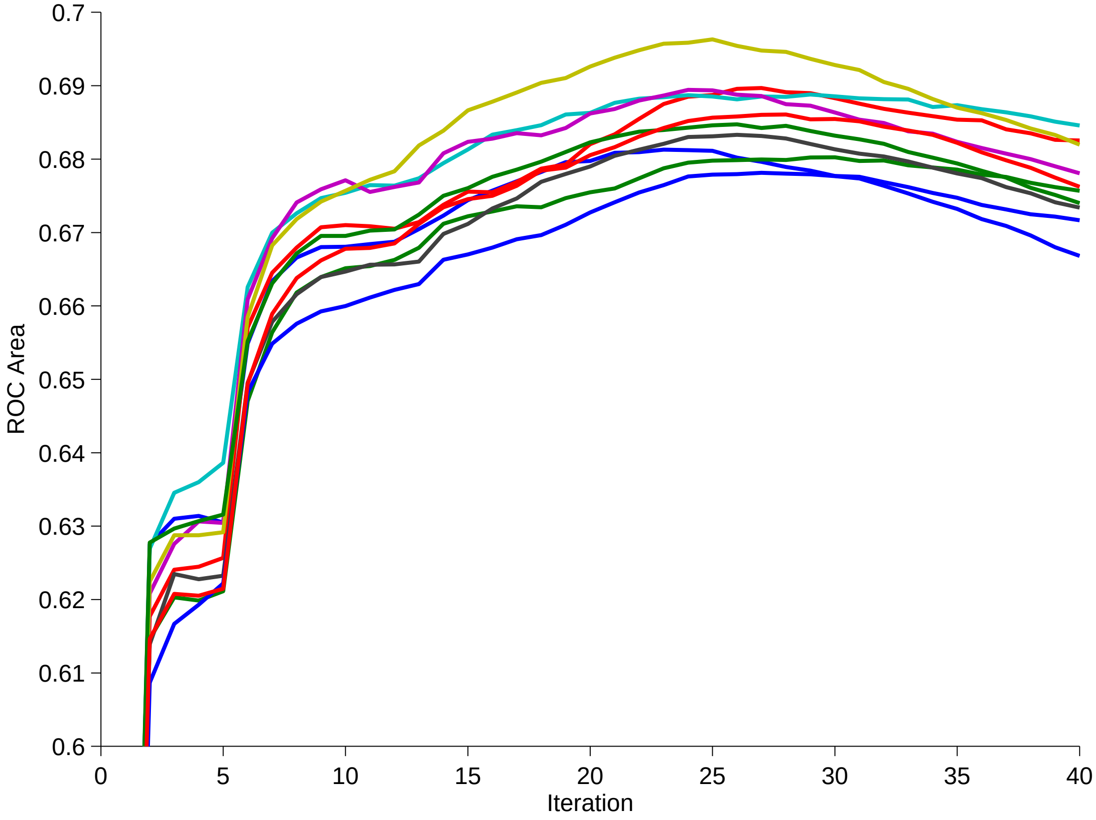

Chapter 5

Modeling real neural signals

The previous chapter set the groundwork for fitting generalized linear models to neuronal data while satisfying 3 desired properties:

- A sparse set of regressors
- Capable of hundreds of parameters
- Cross validation for estimating penalties

In this chapter, we report results from the application of these methods to fit GLMs to real neural array data. The models here contain stimulus effects (spatio-temporal receptive fields) and coupling effects (history terms and past spikes from other cells). In the previous chapter we showed that the L1 regularized GLM path method provides a principled way of performing model selection. Here, we show a variety of results on real neural data. The chapter is laid out in the following way.

First we focus on GLM models built with stimulus terms. We find that the models obtained using the GLM method are very similar to the STAs computed on the same cells, with significantly less noise. We show a range of performance across the population, with an average AUC of .55.

Then we fit GLM models using spike coupling terms. We present fits using a variety of parameterizations, and find that most of the information that helps in fitting is in the most recent 20-30 ms. More temporally distant spiking provides only a small benefit. The cell's own firing history tends to be the most valuable term, with importance falling off with distance from the cell. The parameters are similar to other metrics like noise correlation and cross-correlograms. Surprisingly, the AUC for these models tended to be higher than for the stimulus models, with an average AUC of .72.

Finally, we fit models using both stimulus and spike coupling terms. The terms tend to be mostly orthogonal, but for many cells with poor stimulus models, the stimulus term sets are reduced in size when the spike coupling terms are added. This indicates that there are some components of firing that are affected by both types of terms. These cells may be more selective for the firing of neighbor cells rather than for features of the stimulus.

5.1 Spatiotemporal receptive fields

5.1.1 Spike-triggered average

The spike-triggered average (STA) has been used widely in visual areas like LGN (Reid and Alonso, 1995) and V1 (Jones and Palmer, 1987; DeAngelis et al., 1993) and also auditory areas (Eggermont et al., 1983), among others. Following the treatment in Dayan and Abbott (2005), the STA is given by

$$C(\tau) = \left\langle \frac{1}{n} \sum_{i=1}^{n} s(t_i - \tau) \right\rangle \tag{5.1}$$

where τ is the time interval preceding the spike, and $s(t)$ is the stimulus value at time t. This is the one-dimensional STA, but our stimulus is a $W \times H$ pixel movie, and so the STA is

$$C_{xy}(\tau) = \frac{1}{n} \sum_{i=1}^{n} s_{xy}(t_i - \tau) \tag{5.2}$$

where x, y range over the movie dimensions.

The stimuli are movies presented at 25Hz, with temporally independent frames. The frames were made up of 8x8 pixel noise blocks, each with a value chosen independently from a Gaussian distribution. These values, for all noise blocks and all time points, were normalized and rounded so that the mean was 127.5 and range was 0-255. Each pixel in the final noise movies was a member of an 8x8 pixel noise block. Lastly, the frames were randomly jittered by 0-7 pixels in each direction, so that the inter-block contours can fall between any pixels on a given frame. We performed this translation to increase the spatial resolution of the recovered receptive field. Figure 5.1 illustrates some examples of this stimulus. We chose this resolution for the noise blocks since it was effective for driving V1 cell responses.

Figure 5.1 Three temporal frames from the Gaussian white noise stimulus we presented. Frames are temporally independent, and outside the constant 8x8 pixel noise blocks the frames are spatially independent.

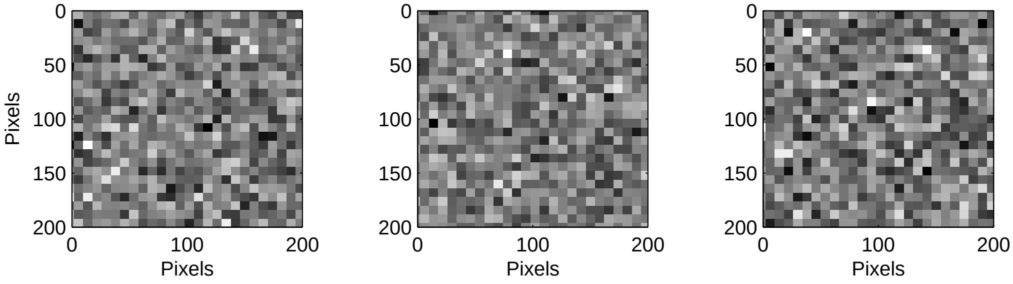

We collected data during the presentation of 16 distinct 3000 frame movies (2 minutes in length each). Spikes were sorted as mentioned in Chapter 2, and are recorded with millisecond precision. For each sorted unit in the population, we compute the spike triggered average as given by Equation 5.2 for the entire stimulus duration. We find that a little less than half (57/128) of the units yielded a distinguishable receptive field with this method. Figure 5.2 shows some example STAs from our cell population. We restrict the modeling of spike trains to these 57 cells for the remainder of this work, since we are interested in modeling cells which have stimulus components as well as network components.

There are many reasons why recorded units may not produce a visible STA. First, the given cell recorded may not have a linear STRF. Some complex cells may not have any linear components. Other cells may be inhibitory interneurons and not be directly influenced by the stimulus. Second, the cell may have a very low firing rate - either an inherent property of the cell or may simply be unresponsive to white noise. For cells like this, another stimulus could be better suited for driving the cell response. Third, there may be too much noise in the spike train, caused either by poor signal or by too much corruption from a large cell population. Such a large multiunit population would corrupt the STA estimate with many features from different cells.

5.1.2 Population properties

As mentioned above, out of the 128 units recorded, 57 had by-eye localizable receptive fields. Figure 5.3 shows, for each of these units, a single time point in the STA, chosen to illustrate the linear receptive field shape. These spatio-temporal receptive field representations have varying orientations and lobe characteristics. The orientations correspond

Figure 5.2 For five example units, the full 150ms of the spike-triggered average. The labels of the cells are in the format ”Electrode label:Sort code”.

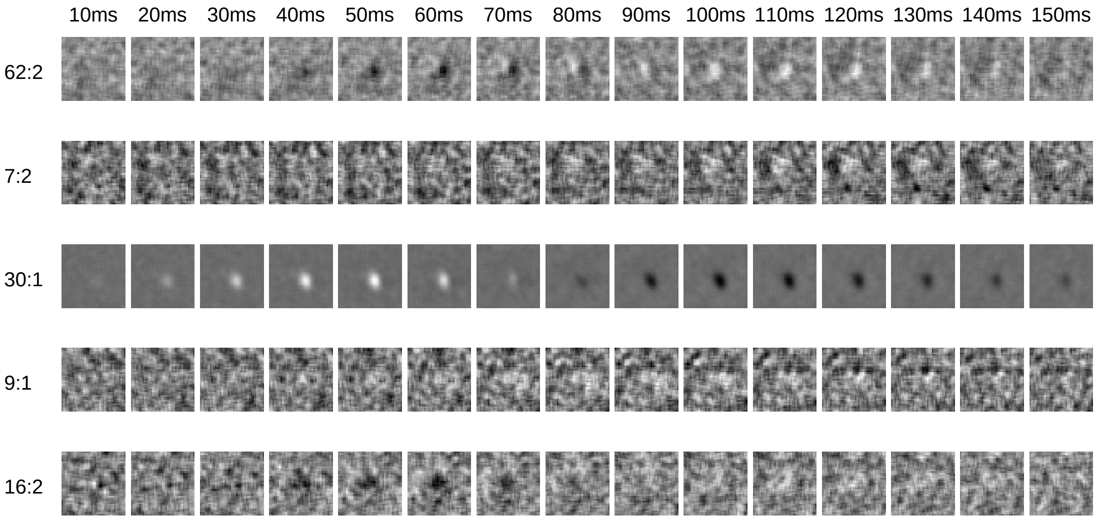

roughly to the orientation tuning measurements derived from moving grating responses. The evoked firing rates to the noise stimuli were between 1 spike/s and 20 spikes/s.

Orientation tuning We computed the orientation tuning (see section 3.4 for more information about orientation tuning) for all cells in the population from the spiking responses to the orientation sequence stimulus described previously (Figure 3.2). Cells may be classified easily in the following groups:

- Little or no tuning
- Undirectionally tuned
- Directionally tuned

The complete population is shown in Figure 5.4. The cells that had no directional tuning were tuned to the same grating orientation, but not the direction of motion of the grating. Directionally tuned cells had only one peak in these plots, corresponding to a preference for both the orientation of the grating and its direction of motion. Sorted units on the same electrode tended to share orientation tuning properties to a large degree. For a

Figure 5.3 One frame from each of the units which had a visible receptive field in the STA. The labels are in the format ”Electrode label:Sort code”. The temporal frame depicted is the frame such that $|\bar{S}|$ is maximized.

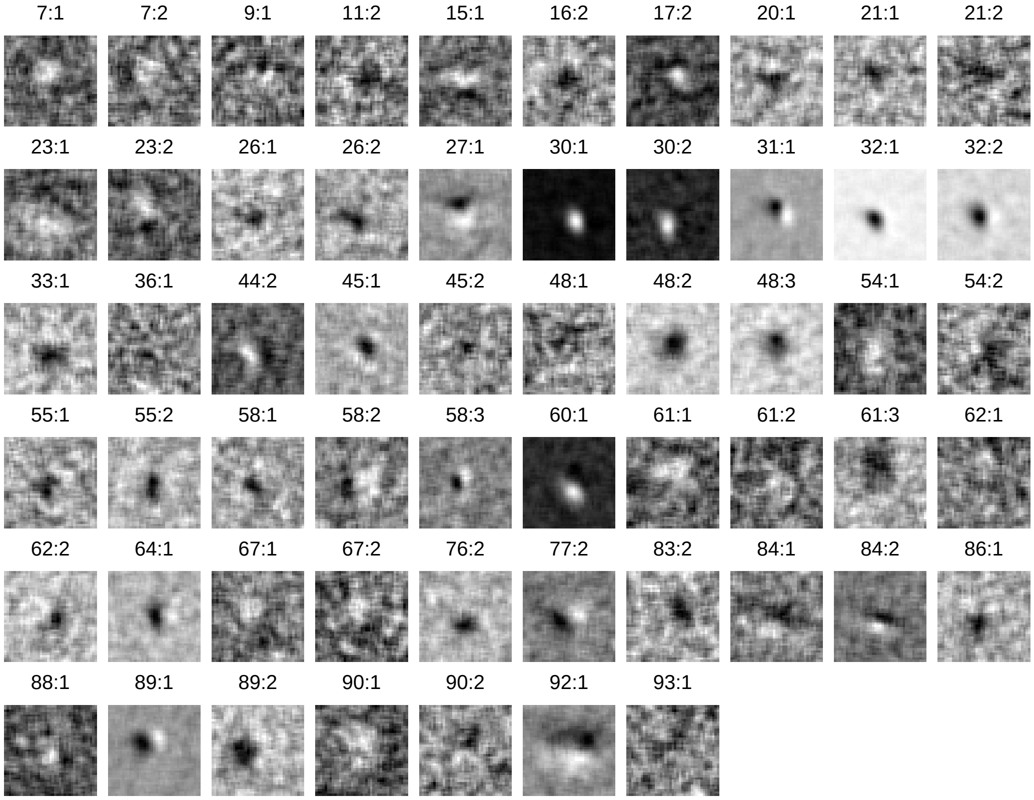

Figure 5.4 A complete population of cells' orientation tuning. This plot is laid out as a 10x10 grid of plots, each corresponding to a single electrode in the array. The plots are arranged spatially in the same manner as the electrodes on the array. Plots with multiple curves correspond to electrodes which had multiple units isolated during the sorting procedure. Plots with a gray background were electrodes which contained no units with a visible STA. The plots with white backgrounds thus had at least one unit with a visible receptive field in the STA. Cells can have orientation tuning but not be responsive to white noise.

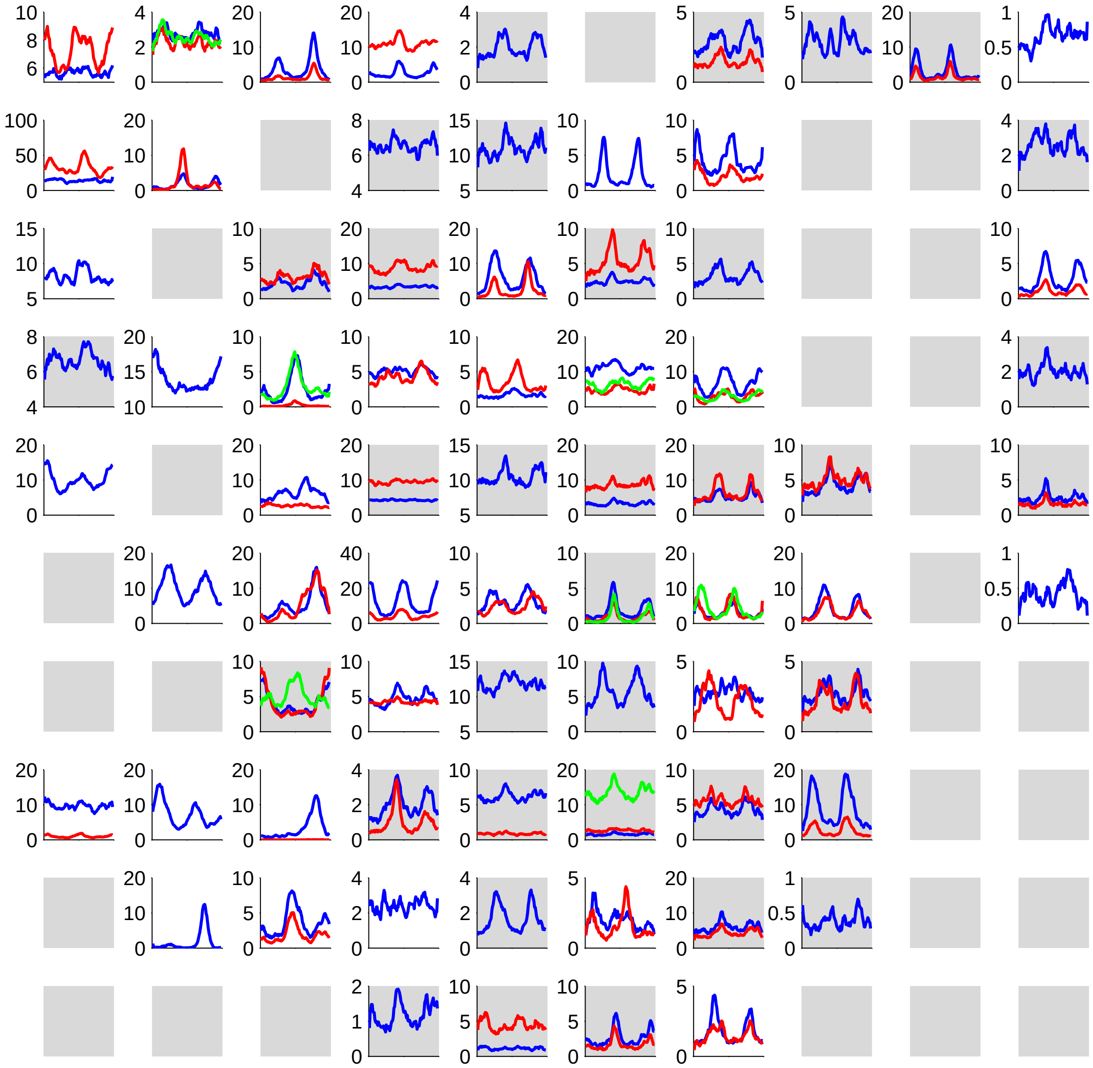

unit to have visible STA features, strong orientation tuning was not required, as there are units in this population which had such features but with very weak orientation tuning.

Receptive field locations The STA maps across the array spanned across a roughly circular area about 150 pixels in diameter, which corresponds to about 2.5 dva in diameter. Each STA map fit within a 80×80 pixel square window, which is thus the window size used for analysis of these receptive fields. The locations of the receptive fields were related strongly to the locations of the electrodes on the array via a linear transformation.

Receptive field size and shape The receptive fields varied in shape and size. In the language of Gabor functions, the receptive fields exhibited 1 or more lobes each in space and time, and varied in size across the population, ranging from 1/6 dva to 1/2 dva in diameter. The orientations varied as well, and corresponded roughly to the orientation tuning given by the grating characterization above. Some receptive fields had lobes present for as little as 30-40 ms, while others persisted for longer than 100ms.

Firing rates Over the course of the 32 minute noise stimuli, the firing rates of the units in the complete neural population had a mean of 4.26 spikes/s. The firing rates for the units that had a visible STA was 4.67 spikes/s, and the firing rates for units without was 3.94 spikes/s. Of the units which had a visible STA, we examined the relationship between a signal-to-noise measurement of the receptive field and the firing rate of the corresponding unit. The STA SNR is defined as

$$\text{STA SNR} = \frac{\max_{xy\tau} |C_{xy\tau}|}{||C||} \tag{5.3}$$

Though the denominator contains some true signal pixels, most of them are from outside the receptive field in space or time. Thus the denominator is strongly related to the noise.

Figure 5.5 shows a scatter plot of the units. There was a Pearson correlation of .659 ($p < 10^{-7}$), indicating that cells with higher firing rates tended to have more easily discriminable receptive fields from their STAs.

Waveform quality To determine if the quality of the unit isolation was related to the quality of the STA, we calculated the signal-to-noise ratio for the action potential waveforms for the same data. The measure is given by Equation 2.3. Though the quality of the waveform (given by the waveform SNR) was on average higher for the cells which had visible receptive field features in their STAs, there was no reliable relationship between the quality of the waveform and the quality of the receptive field (paired t-test, Figure 5.5).

Figure 5.5 A: Population firing rates. The average firing rate was higher for the subpopulation of units that had a visible receptive field in the STA. There was a positive correlation between the firing rates and the receptive field quality for those units with a visible receptive field. B: Waveform SNR. The average waveform SNR was higher for the subpopulation of units that had a visible receptive field in the SNR, but we found no statistically significant correlation between the quality of the receptive field and quality of the recordings, for cells with visible receptive fields.

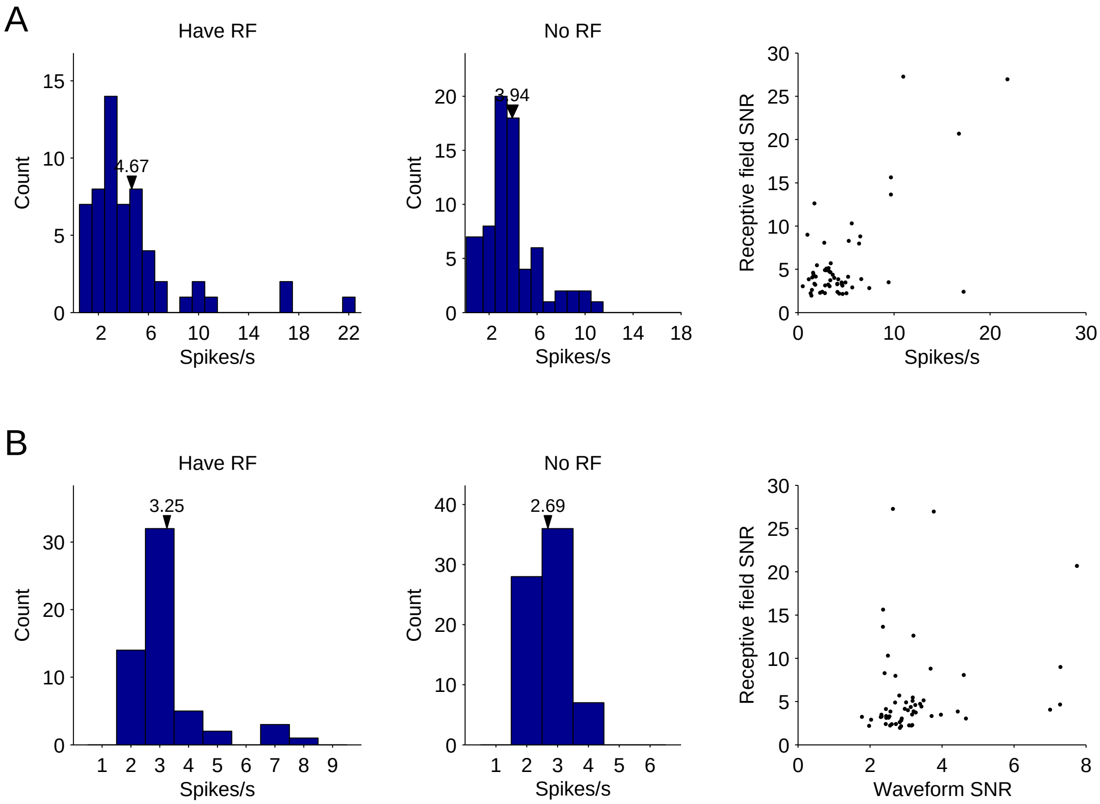

Figure 5.6 The spatial and temporal components of the spatio-temporal Gaussian filters.

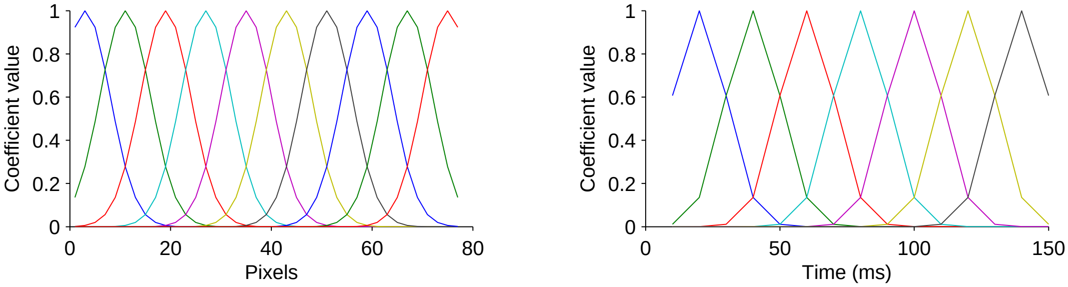

5.1.3 Model fitting from white noise

Using the procedure laid out in Chapter 3, we fit models to the spiking data for the cells in the population. The biggest obstacle is the huge dimensionality of the stimulus. If the pixel representation of the movies are used, and the last 150ms are relevant for spiking influence, there are $320 \times 320 \times 150 = 15,360,000$ parameters. This is far out of bounds of the practical limitations of the fitting method and data. We reduced the number of potential parameters using four methods:

Movie downsampling: We reduced the movie to 160x160 by just considering every other pixel in each dimension. The resulting movie was 160x160.

Space pruning: Using the STAs computed above as guides, for the cells with visible receptive fields we located the approximate locations of the receptive fields. For each unit, an area of 40x40 pixels of the 160x160 original image was located.

Time pruning: The spike trains were binned at a 10ms resolution, with each bin containing the spike count within a particular 10ms. This reduced the number of temporal points in the model to 15 from 150.

Stimulus transformation: We transformed the stimulus into Gaussian bump responses, as in Chapter 4. The kind of bumps used are shown in Figure 5.6. The separation of the bump centers was 4 pixels spatially in the 40x40 pixel space, and 2 time points (20 ms). The total number of parameters was $10 \times 10 \times 7 = 700$, which is 100 parameters for each of 7 distinct time points.

We fit the models of 700 parameters to the spike train of the units. For each unit, we computed the regularization path, starting with the max λ, and proceeding in logarithmic steps toward a low λ. Figure 5.7 shows one of the fits on a particular cell, although this result in typical. The model fit matches the STA well. We additionally ran 10-fold cross validation with the cells, and computed the ROC curves and areas as described in Chapter 4. This particular cell had an average (across the folds) maximum ROC area of .57.

5.1.4 Regularization paths

We used cross validation to estimate the performance of the models on 10 different test sets. The total number of data points for the 32 minutes of stimulus was 192,000. Thus each test set consisted of 12,000 test points and 180,000 training points. For each model created, we computed a ROC curve for each point in the regularization path. The point in the regularization path with the largest average area across all the cross validation runs was considered the optimal penalty.

Some of the cells had a maximum ROC area point as the last point in the regularization path. The path could be extended in these cases to compute the ROC values for more of the path, but for most of these cells the predictability of the spike train from these stimulus-influence models tended to be quite low. In addition, the variance of the distribution of values across the different cross validation folds tended to increase with decreasing penalty. These models are unlikely to achieve a better model with a reduced penalty since the trend was that their performance was diverging.

5.1.5 Discussion

We computed the correlation between the STA maps and the maps over the same windows derived from the fitted models. The correlation described here between a model fit and the STA is the Pearson correlation between the two sets of pixel values. A summary of this analysis is shown in Figure 5.9. Plot A in this figure shows that the faithfulness of a model to the STA increases for the range of penalties considered for these plots. There remain differences between the two, since STA is computed for each pixel independently and these models have strong dependences between the parameters. The amount of smoothing used for the stimulus transformation affects the actual values here, with either very little smoothing or too much smoothing causing this correlation value to decrease.

In plot B, the relationship between map correlation and ROC area for all 57 units are plotted. For cells with high ROC values, the predictive value of the models is high. These same units tend to have larger correlation between the STA and model parameters. Even when the max of the ROC area curve is passed, the STA/model correlation tends to increase as the penalty pushes the model into overfitting. Units which have low ROC values have models which cannot predict cell firing well, and these are also limited in their correlation

Figure 5.7 One cell in the population with a particularly strong spike-triggered average. A: Five time points in the spatio-temporal receptive field and the corresponding models. At the top is the spike-triggered average. Below are four points in the regularization path. B: The 10-fold cross validation assessment of the regularization path. The second point above, $\tau = 50$, is around the best fit with respect to the cross-validation procedure.

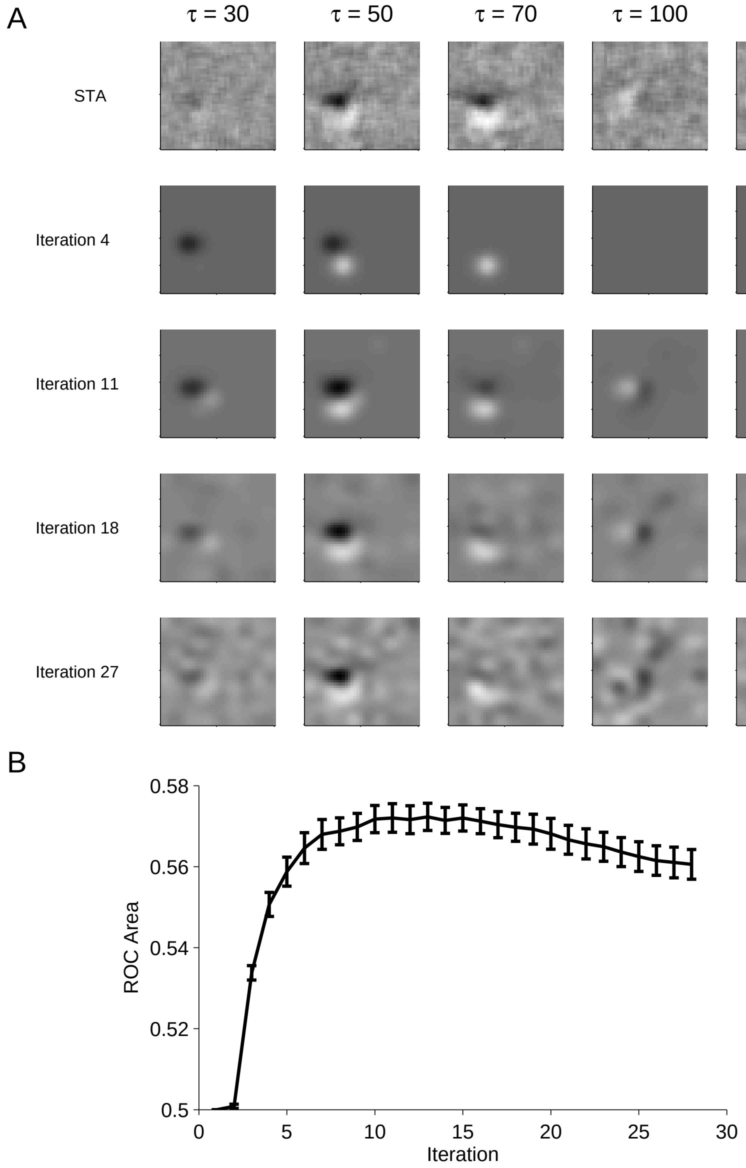

Figure 5.8 Fitting stimulus models. A: Histogram of the best AUC values for the cells which had visible STAs, given by 10-fold cross validation (n=57). B: Scatter plot of the relationship between AUC and the number of nonzero parameters. C: Colormap in array space of the best AUC values for each unit. For electrodes with more than one unit, the square is split into 2 or 3 components. These are only the units with STAs.

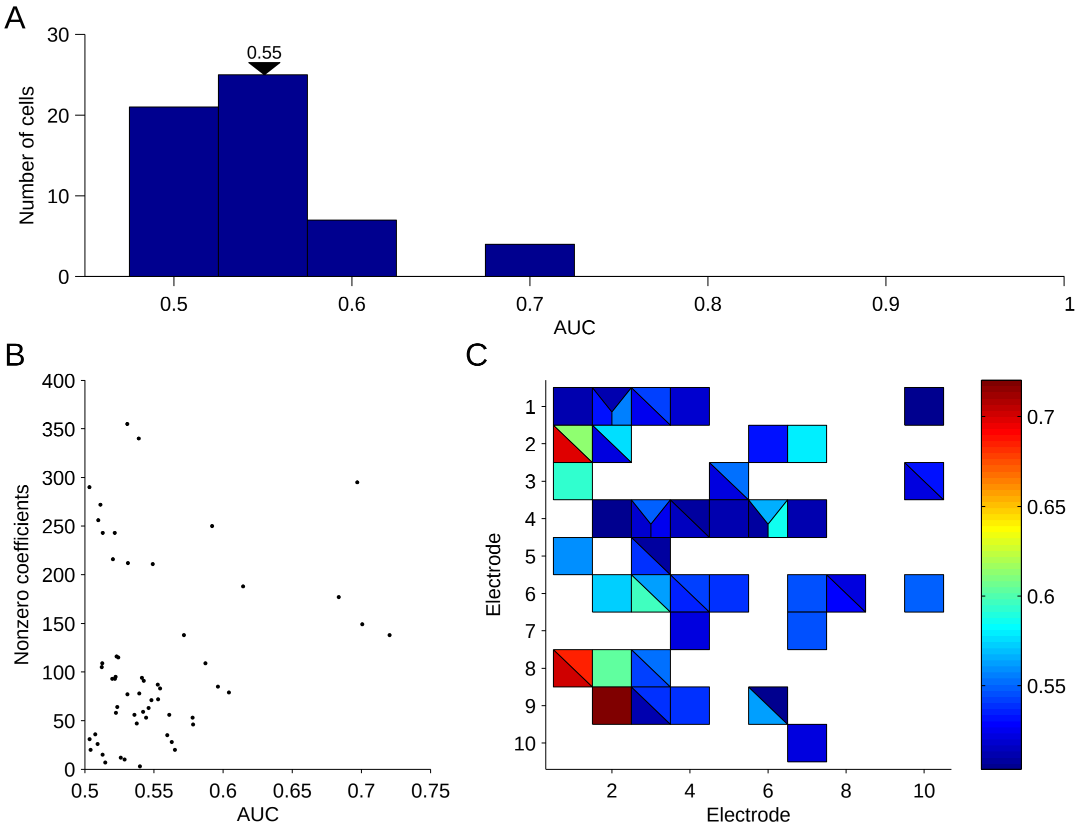

with the STAs.

5.2 Functional connectivity

The previous section presents a model of the visual system where each neuron is independent and solely driven by a visual stimulus and noise. However, neurons in V1 are not the endpoints of a feedforward computation from the retina to the cortex. They are members of a dense network, with each cell connected to hundreds of other cortical cells. The network contains feedforward, lateral, and feedback connections, and is rife with interleaved excitatory and inhibitory cells. The topic of functional connectivity is undergoing extensive study, as the technologies that make it possible to record from many cells simultaneously have grown in popularity.

Direct observation of causal connectivity in extracellular single unit recording is typically not possible in an area like V1. Even if a casual pair of cells (A,B) is recorded, the effects of cell A on cell B will be somewhat washed out due to all the other hundreds of inputs into cell B. The field has relied on measuring correlated firing as a proxy for connectivity.

We review a few of these methods in this section, noise correlation and cross-correlation. We also explore the modeling of cell influences using the GLM. Notably, we found that for many cells, other cell influences are more valuable as a whole in predicting cell firing than the stimulus effects given in the previous section.

5.2.1 Noise correlation

Correlation between the firing of two neurons break down into two classes, signal and noise correlation. “Signal correlation” characterizes the relationship between two cells’ average firing rates to different stimuli. Cells which increase their firing rates to the same stimuli are said to have positive signal correlation. An example of a pair of cells with positive signal correlation are two cells which have similar orientation tuning curves. This type of correlation is computed from average firing rates only, and it thus does not quantify correlations that are unrelated to visual stimulation. The other type of correlation is “noise correlation”, which is the tendency of cell responses to rise and fall together during the presentation of the same or similar stimuli. The purpose of this correlation is unknown, but possible interpretations of this shared noise range from improving signal strength (redundancy) to increasing the information a population encodes. Averbeck et al. (2006)

Figure 5.9 Summary of the comparison between model receptive fields and the STAs. A: The correlation between the model receptive field map and the STA for the first 4 points in the regularization path, stepping the penalty λ down from $\lambda_{\max}$ in 15 logarithmic steps toward $\lambda = 1$. The mean correlation across the population improves as the penalty is lowered. B: For the same 4 steps in the regularization path, the correlation between the maps is compared to the ROC curve area. Lines connect points corresponding to the same cells. The points are colored by their iteration, and are colored the same as in A.

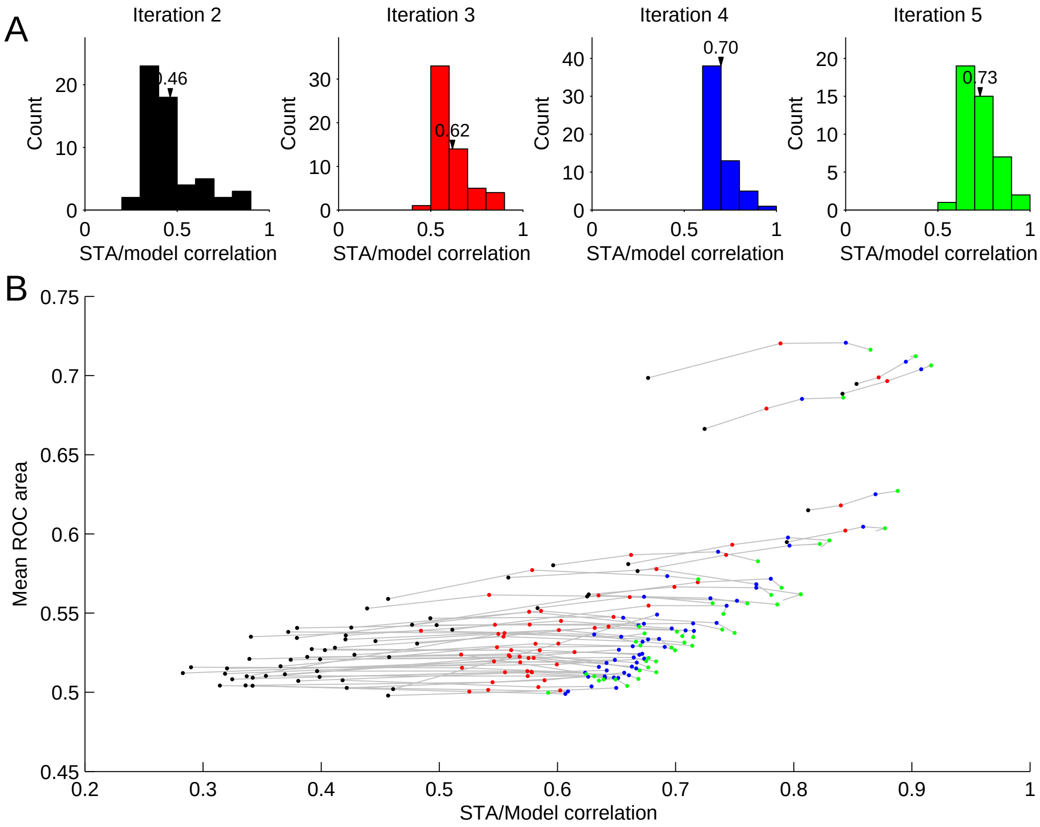

have provided an extensive review on the subject of noise correlation and information encoding, where they show that noise correlation can increase or decrease the information a population encodes, depending on the nature of the noise correlation.

Since our experiments were performed as continuous movies with an animal whose gaze is fixed, "trials" have arbitrary boundaries and we can measure noise correlation at a range of time scales, breaking up the stimulus in trials of any length. The noise correlation between two cells is given by the Pearson correlation of the paired spike count distributions n_1, n_2:

$$\rho = \frac{\text{Cov}(n_1, n_2)}{\sqrt{\text{Var}(n_1)\text{Var}(n_2)}} \tag{5.4}$$

The distribution, ideally, is over a repeated stimulus. The motivation is that if the stimulus is held constant, none of the correlation measured is due to signal correlation between the cells. The unrepeated noise movie stimulus which was used to fit models in the previous section has no repeated movie segments, but we could potentially consider trials at different points in the noise movie to be equivalent, stimulus-wise, under the assumption that the noise movies generally affect the cells the same, and any signal correlation will be dwarfed by the noise correlation. To see if this was a valid assumption, we computed the signal correlation between all the pairs of cells in addition to the noise correlation. Figure 5.10A shows the relationship between signal correlation and noise correlation. The relationship between the two types of correlation is very strong, indicating that the variations in the different 300ms noise movies certainly do have a influential effect on the correlation between cells. The reason for this relationship is due mostly to the fact that cells whose receptive fields are in close proximity to each other tend to be affected by the same stimulus features simultaneously. The electrode distance between cells with similar receptive field locations also tends to be smaller. Moreover, noise correlation is also inversely related to the distance between the pair of electrodes. Figure 5.10B shows these two relationships for these data. It is notable that the signal correlation does not drop to zero, even for very distant electrodes. These pairs generally have no receptive field overlap, and thus the influence of the stimulus alone is not sufficient to account for the positive correlation. One possibility for this is that some noise correlation may be coming through; a result of the limited number of trials run (n=120). More trials would have been likely to reduce this correlation at large distances further. It is also possible that the areas outside the purported receptive fields may have an effect (known as the extra-classical receptive fields), and there is some receptive field overlap after all. Regardless of the reasons, computing the noise correlation independent of the stimulus risks corruption by signal correlation, even with a stimulus such as Gaussian white noise.

Since the previous section dealt only with the cells that had a visible STA, we plotted the noise correlation distributions computed over repeated noise movie segments for two groups of pairs. First is the pairs whose members both had visible receptive fields, and the other group is the remaining cells in the population, where both units didn't have visible receptive fields. Figure 5.10C indicates that pairs whose units do not show visible STA maps tend to have higher correlation. These cells may not be responsive to noise, and thus the lack of stimulus drive may be giving rise to the increased stimulus-unrelated correlation.

5.2.2 Cross-correlograms

A related way of measuring noise correlation is the cross-correlogram (CCG) (Perkel et al., 1967). The CCG provides a way of measuring the relative spike timing of two neurons.

$$\mathrm{CCG}(\tau) = \frac{1}{M}\frac{\sum_{i=1}^{M}\sum_{t=1}^{N} y_{i1}(t)y_{i2}(t+\tau)}{\mathrm{Tri}(\tau)\sqrt{\bar{\mu}_1\bar{\mu}_2}} \tag{5.5}$$

where M is the number of trials, N is the length of the trial (in ms), y_{ij} is the spike train function for cell j on trial i, τ is the time lag, and $\bar{\mu}_j$ is the mean firing rate of the cell j. Tri is the triangle function which corrects for the amount of overlap in the two spike trains that differs with time lag. We normalized the CCG by the geometric mean of the firing rates, in line with previous studies of this kind (Smith and Kohn, 2008).

The CCGs computed from the equation above can contain stimulus-locked correlation in addition to noise-correlation effects. A standard practice is to compute a shuffle correction, which is the same computation as the CCG above, but with the trials shuffled randomly for one of the two cells in the pairing. Subtracting this correction term from the raw CCG removes correlations that are locked to the stimulus. The resulting CCG reflects correlation on a range of time scales, including precisely aligned spike times and slow covariations in firing rate.

To measure the correlation on different time scales using the CCG, we created jitter-corrected CCGs (Harrison et al., 2007) to subtract from the raw CCGs. The jitter-correction CCG is created by shuffling individual spikes across trials. In more detail, the duration of the repeated trial is divided into into equally sized epochs based on a parameter, the jitter window size. For each trial, and each spike, a new spike is chosen randomly without replacement from the set of spikes in the same epoch across all trials. This method preserves the spike count in each epoch and trial. Thus, correlation at a timescale greater than the window size is preserved, but correlation at a faster timescale is eliminated. It also preserves the PSTH exactly, since the set of total spikes at each time point remains the same, which preserves stimulus-locked correlations. Subtracting the jitter-corrected CCG from

Figure 5.10 A: For each pair in the population, the mean noise correlation and signal correlation for the pair was computed on 300ms segments of repeated noise. B: Two plots show the fall-off of noise correlation and signal correlation with increasing inter-unit electrode distance. C: The cell pairs broken down into two subsets, pairs where neither cell had a visible STA and pairs where both did. The histograms show the noise correlation distributions for these two groups. The means are indicated with arrows.

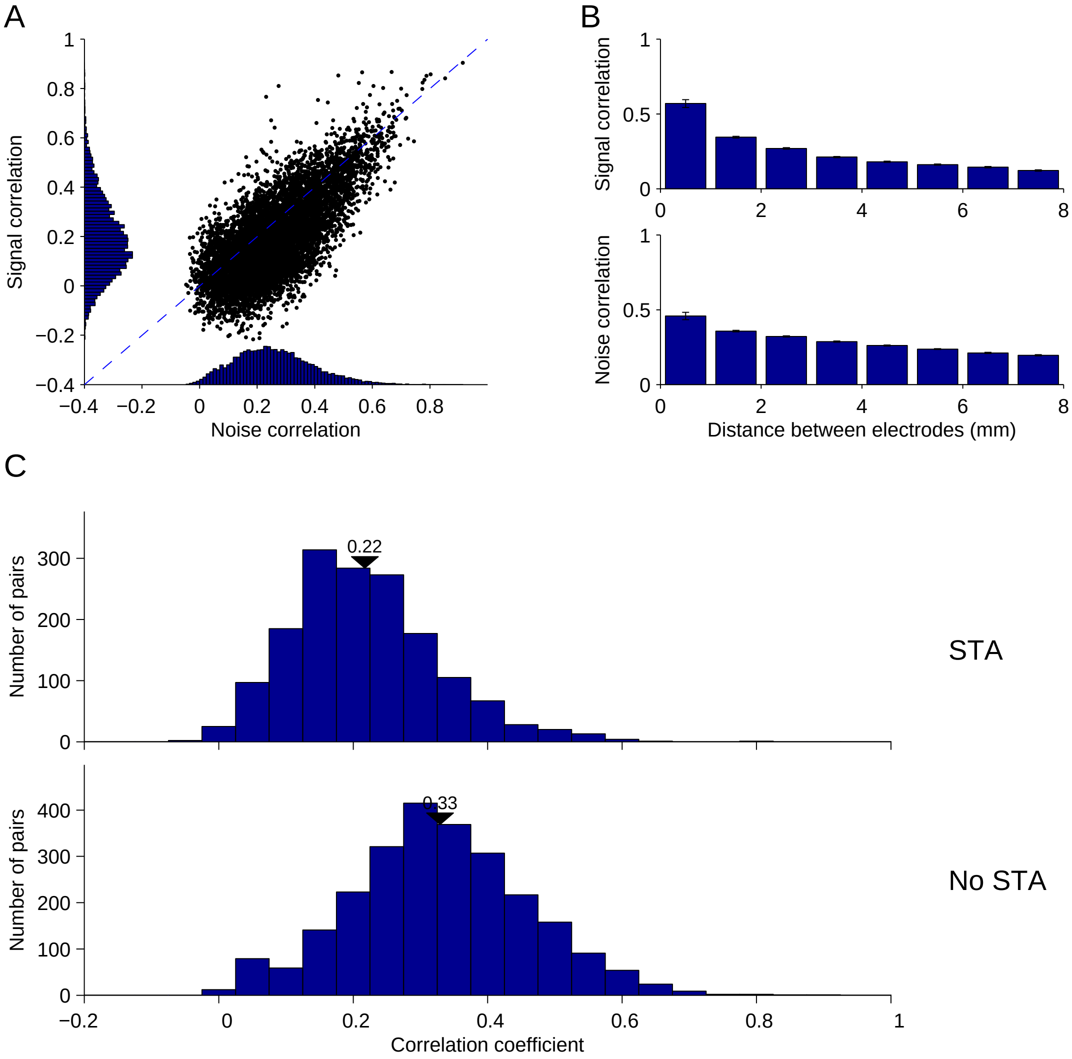

the raw CCG yields an estimate of the relative spike timing of two neurons at arbitrarily precise timescales, independent of stimulus effects.

Figure 5.11 shows the population CCGs under a variety of correction conditions. We computed the shuffle and jitter corrections for each pair of units, and then smoothed the results with a 10ms boxcar window. We excluded same electrode pairs from this analysis to eliminate the possibility of spike sorting corrupting the result. In panel A, the highest curve is the shuffle corrected CCG, and the lower curves are the jitter corrected CCGs. The jitter corrected curves remove stimulus effects and correlation on a timescale beyond a specified temporal window. As this window decreases, the curves become lower. Panel B shows only the jitter-corrected CCGs. Since these are averaged across all pairs, they reflect general population trends rather than individual pair correlation. On this level, there is essentially no correlation with a jitter window of less than 10ms. The window sizes are 400ms, 200ms, 100ms, 50ms, 25ms, 10ms, 5ms, 1ms. Panel C shows the mean (absolute value) peak height for different pair distances. Each curve corresponds to a specific jitter window, colored in the same way as in panels A and B. Nearby electrode pairs have a higher mean peak height for any window size, and all fall off in general with distance. The curves do not decrease all the way to zero, since there is a level of noise in the CCGs and just by chance the maximum peak height is some nonzero quantity. Correlation at all timescales is greater on average for nearby pairs, with more precise timing falling off faster and less precise timing occurring somewhat for distant pairs.

5.2.3 Functional connectivity in the GLM

With respect to functional connectivity, we addressed the following questions using the GLM framework laid out in Chapter 3.

- Are the responses of other cells helpful in predicting cell firing?
- What kinds of cells are most predictable? What kinds of cells are most helpful in predicting other cell responses?
- Does a cell's own history help more than other cells?
- What kind of regularization is most appropriate for this kind of modeling?

Figure 5.12 shows an example of the general fitting process with respect to coupling terms. Panel A shows points in the regularization path for the fitting of one cell, where more terms' coefficients become nonzero as the L1 penalty is decreased. Panel B shows

Figure 5.11 A: Mean corrected cross-correlograms (CCGs). The highest curve is the shuffle-corrected CCG. The lower curves are the jitter-corrected CCGs. B: Blowup of the plot in (A). The corrected CCGs have window sizes 1ms, 5ms, 10ms, 25ms, 50ms, 100ms, 200ms, 400ms. The largest window size corresponds to the largest curve. C: For each cell pair CCG, we computed the maximum peak of the CCG. This plot shows the mean CCG peak height for different jitter-correction windows, in the same configuration as (B). The peak height is larger for nearby electrodes, and falls off with distance.

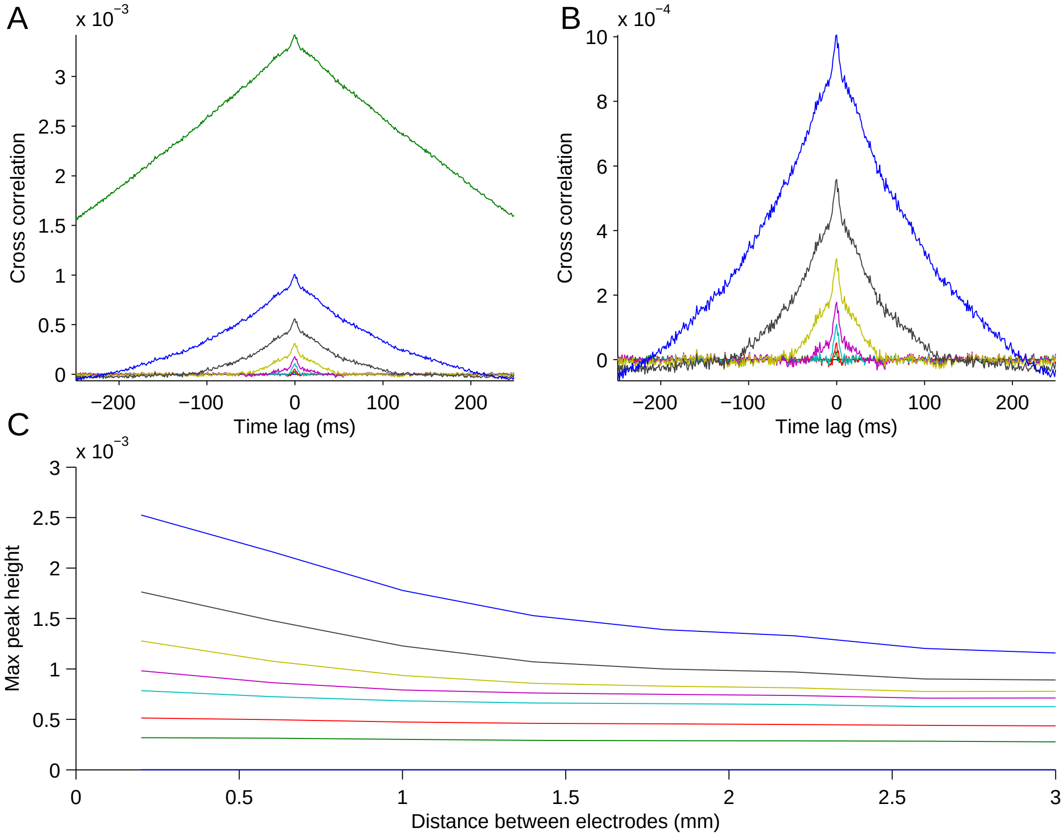

the mean AUC with respect to iteration in the path. The maximum of this curve corresponds to the most effective L1 penalty value. For reference, panel C shows the noise correlation between this cell and the other cells in the population. These values are positively correlated ($p < .05$, panel D).

Population results

For each of the units analyzed in the previous section (units with visible STAs), we fit GLMs to their firing rates, using other unit firing as the input data instead of the stimulus parameters. We observed a range of AUC values for these fits (Figure 5.13), from near chance levels up to .9. There was a significant ($p < 10^{-6}$) negative correlation between the goodness of fit and the number of nonzero coefficients used in the model. Thus, the units which were well predicted by the other firing in the population also did not require a large model to achieve the best AUC. The models built for units which could not be predicted well by the population had a large set of maginally effective parameters. There was also an effect of array location. Figure 5.13 shows that units toward the left side of the array generally have smaller maximum AUCs based on the population activity than units on the right side.

The AUC gradient across the array could have many potential causes. The quality of recordings may vary across the array surface due to an insertion problem. Related to this is the possibility that the array may be deeper on one side, causing the electrodes in the array to span multiple cortical layers. There could also be a feature difference in the right side of the array, like a blood vessel. Without histology it is impossible to know the reason definitively, but we instead examined other properties of the cells with respect to the array position to make some inferences about the cause of the AUC gradient.

Figure 5.14 shows the analyses we did to address this finding. A quality difference in cell sorting or in recording signal across the array is a possible explanation for the gradient, but in panel A it is apparent that the action potential waveform quality does not vary in the same manner across the array surface. Indeed, we found no significant correlation between the waveform SNR and the AUC measure. Another possibility is that the cells being sampled from are different populations due to a variation in impedance across the array. Panel B shows that this is also not the explanation, and while there are changes in impedance across the array surface, this measure is uncorrelated with the AUC measure. As is expected, we can see in panel C that noise correlation varies in the same manner as AUC, and the two are highly correlated ($R = .834, p < 10^{-16}$). Noise correlation is higher for superficial layers 2-3 and also layer 5, and less high for layer 4 (Smith and Kohn, 2009). It is thus likely that the AUC gradient is caused by a difference in recording

Figure 5.12 The same cell as Figure 5.7, here fit with coupling terms instead of a spatio-temporal receptive field. A: 8 points in the regularization path. These plots are in electrode space - the colors indicate the value of the parameters chosen for the corresponding coupling terms. The white X indicates the location of the cell being modeled. B: The 10-fold cross validation assessment of the regularization path. The function hits its maximum at 20. C: The Pearson correlation between the cell and the other cells in the population. The cell is marked with an X. D: Scatter plot of the parameter values (α) at iteration 20 and the correlation values. Only pairs in which $\alpha \neq 0$ are shown here.

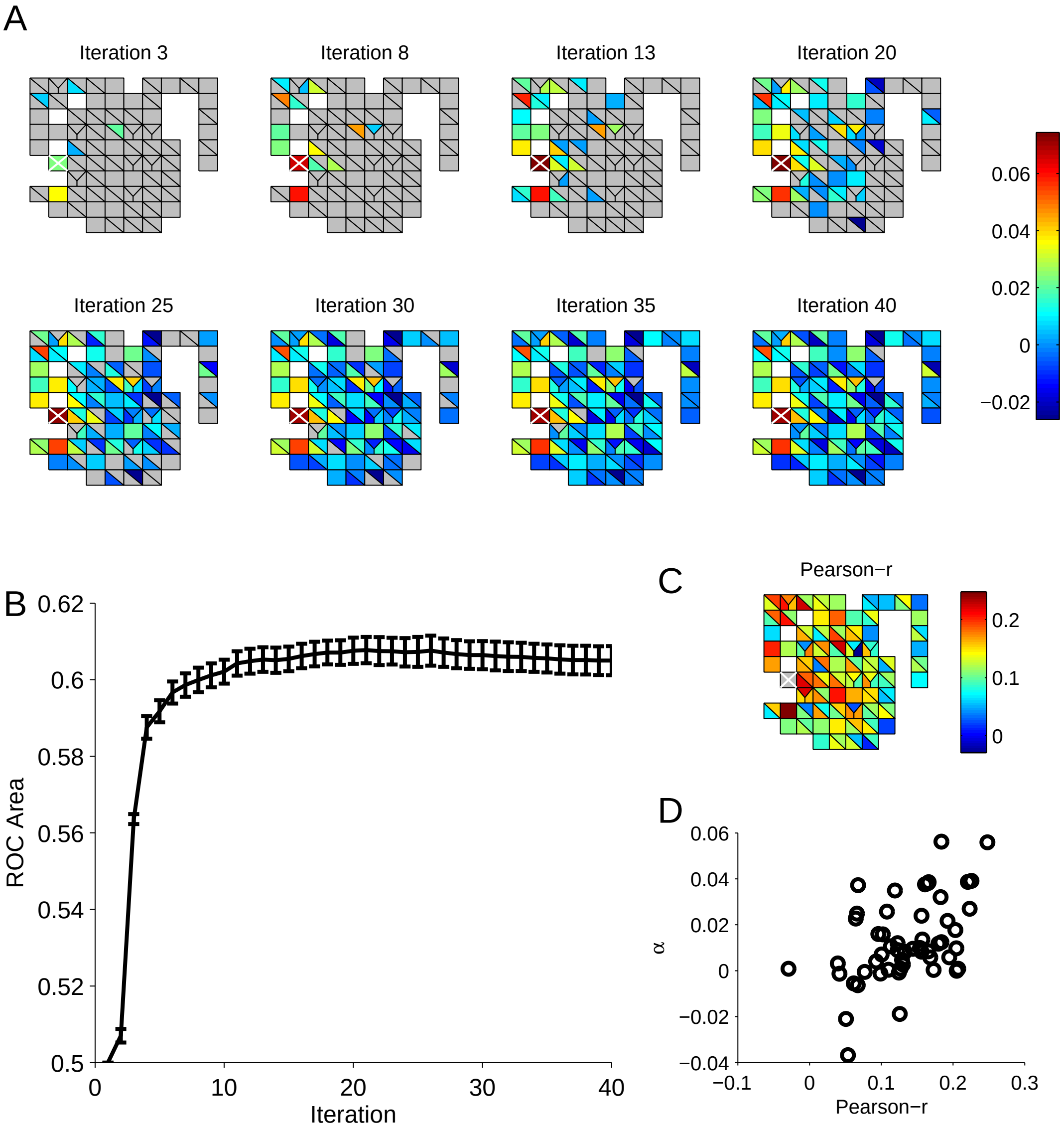

Figure 5.13 Fits to coupling terms. A: Histogram of the best AUC values for the cells which had visible STAs, given by 10-fold cross validation (n=57). B: Scatter plot of the relationship between AUC and the number of nonzero parameters. There was a significant negative correlation ($p < 10^{-6}$). C: Colormap in array space of the best AUC values for each unit. For electrodes with more than one unit, the square is split into 2 or 3 components.

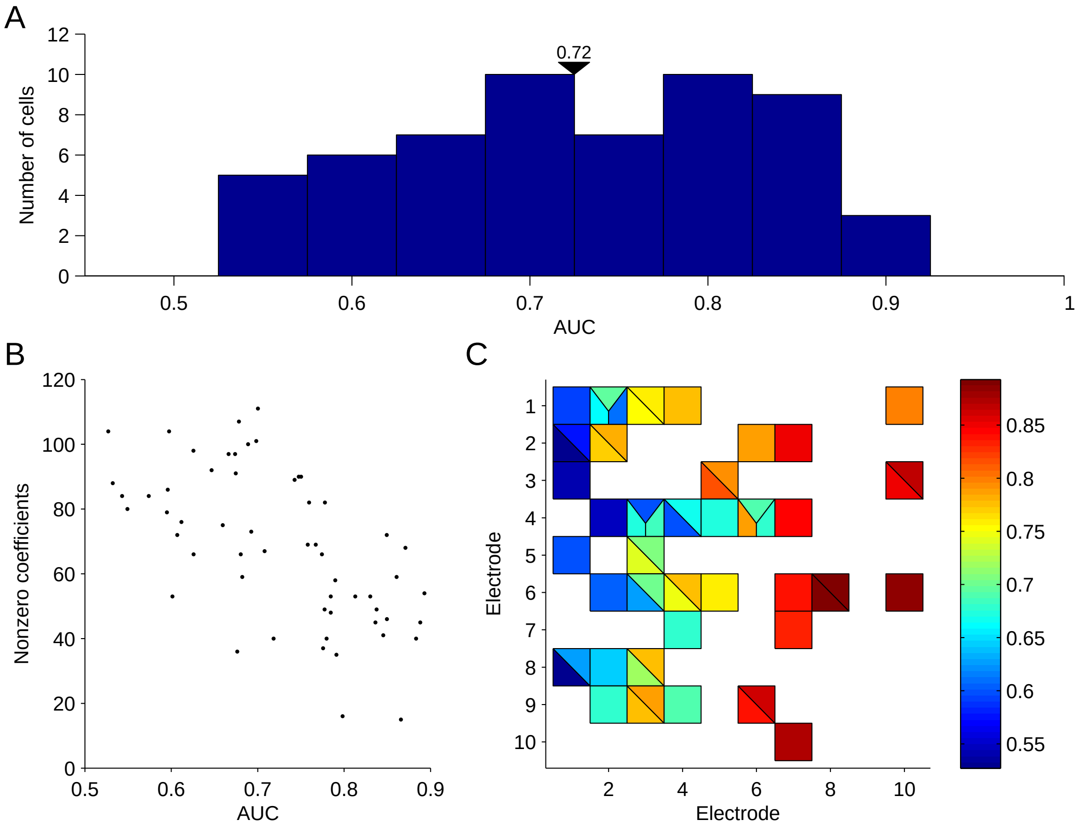

Figure 5.14 Comparison between goodness of fit and various features of the array. A: The waveform SNR is given by the ratio of the peak of the mean waveform to the standard deviation of the noise. We found no correlation between the waveform SNR and the fit quality. B: The impedance of the electrodes also was uncorrelated with AUC. C: The nearby noise correlation (averaged for cells within a small distance) follows the same pattern as the AUC plots. D: Indeed, the AUC is correlated with the nearby noise correlation.

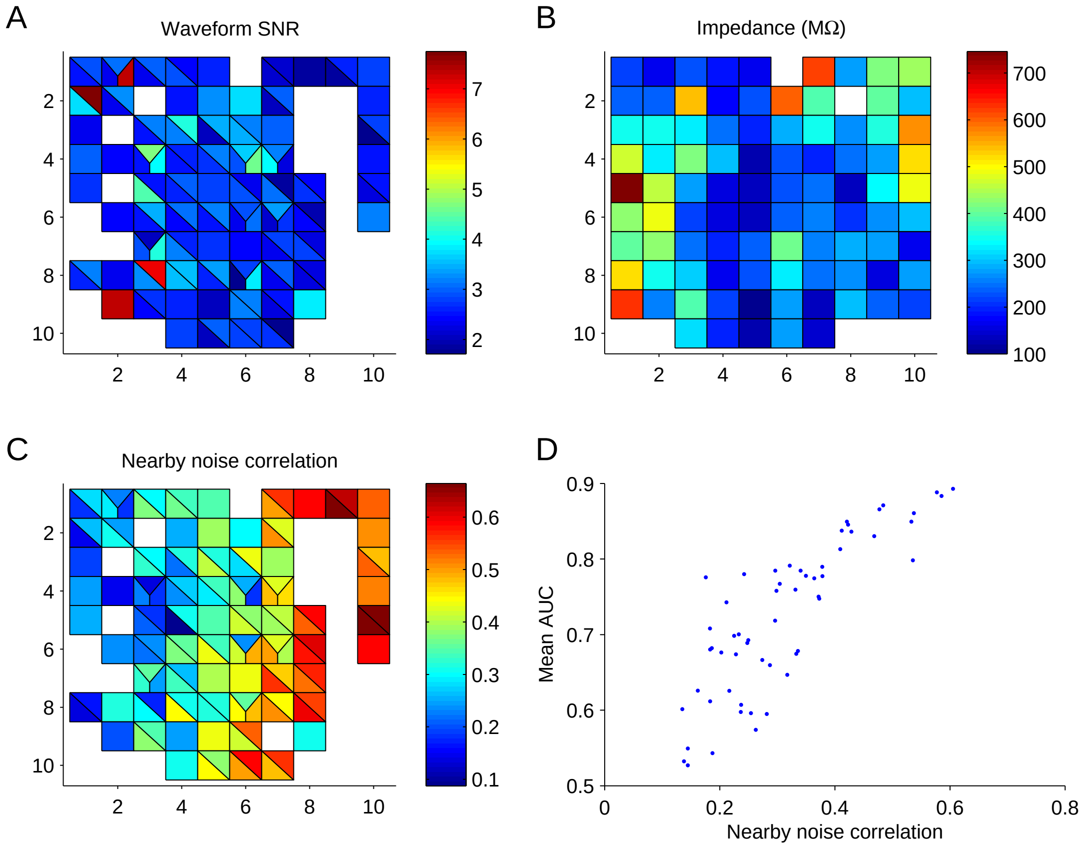

layers. Since we do not have histology for this array, we would need to analyze another array experiment where the recording depth is known to further address this finding.

History

We examined the impact of including a cell's own history as a predictor of future firing. First, in the case where a cell's history is penalized in the same manner as the rest of the cells, we compared the "rank" of that coefficient, which is 1 + the number of coefficients whose absolute value is larger than the absolute value of the history coefficient. For more than half of the cells, the history coefficient was the largest of all coupling coefficients, and for 50/57 cells the history coefficient was one of the top 3. These data is shown in Figure 5.15A. Next, we removed the history term entirely, to see if it is truly necessary in producing good models, or if it was just highly correlated with other cells that could pick up the slack when the history term is not included. The difference between the AUC in each case is given in Figure 5.15B. The mean AUC shifted lower by .01 when removing the history term from the terms, a significant shift ($p < 10^{-12}$). We also tried to unpenalize the history term, while continuing the L1 penalty on the other terms. The difference between the two conditions of penalized and unpenalized history is shown in Figure 5.15C. We found no significant difference between those two distributions (paired t-test), and thus from a prediction standpoint the penalization of history is irrelevant. Finally, we compared the fit with just a history term to the fits with all terms. Figure 5.15D shows that history alone is generally far worse in the AUC than the full model. The conclusion we draw from these analyses is that history is in most cases one of the most important predictors, but it is not by itself enough to achieve optimal performance.

Regularization types

The nature of the regularization penalty required that we prepare the data in certain ways before the fitting procedure. For example, if we use the raw firing rates of the cells as input for the GLM, cells with higher firing rates are effectively not penalized as much as low firing rate cells. This is due to the fact that these low firing rate cells require a large coefficient to have any impact. Indeed, firing rates and membership in active sets are highly correlated ($r = .6025, p < 10^{-5}$). Normalizing the input to the same mean firing rate yields a small but significant increase in the mean AUC of .0009 (paired t-test, $p < .02$). This change comes at a cost, with the mean active set size increasing by about 10 elements. Most of the elements added to active sets are the low firing rate cells. For the rest of the analyses in this work, we chose to normalize the firing rates of the cells,

Figure 5.15 A: Histogram for 57 cells of the rank of the intrinsic history term, in models where the history term is penalized the same as other extrinsic terms. Rank, here, is defined as the location in the decreasingly sorted sequence of terms, sorted by the absolute value of the term's fitted coefficient. B: Compared to the fit presented in (A), the histogram of the change in AUC due to removing the history terms. There is a small decrease in performance. C: Compared to the fit presented in (A), the histogram of the change in AUC due to removing any L1 penalty on the intrinsic history term. There is no change in the AUC. D: Compared to the fit presented in (A), the histogram of the change in AUC due to removing all the extrinsic terms, leaving only the unpenalized history term. There is a large decrease in the AUC.

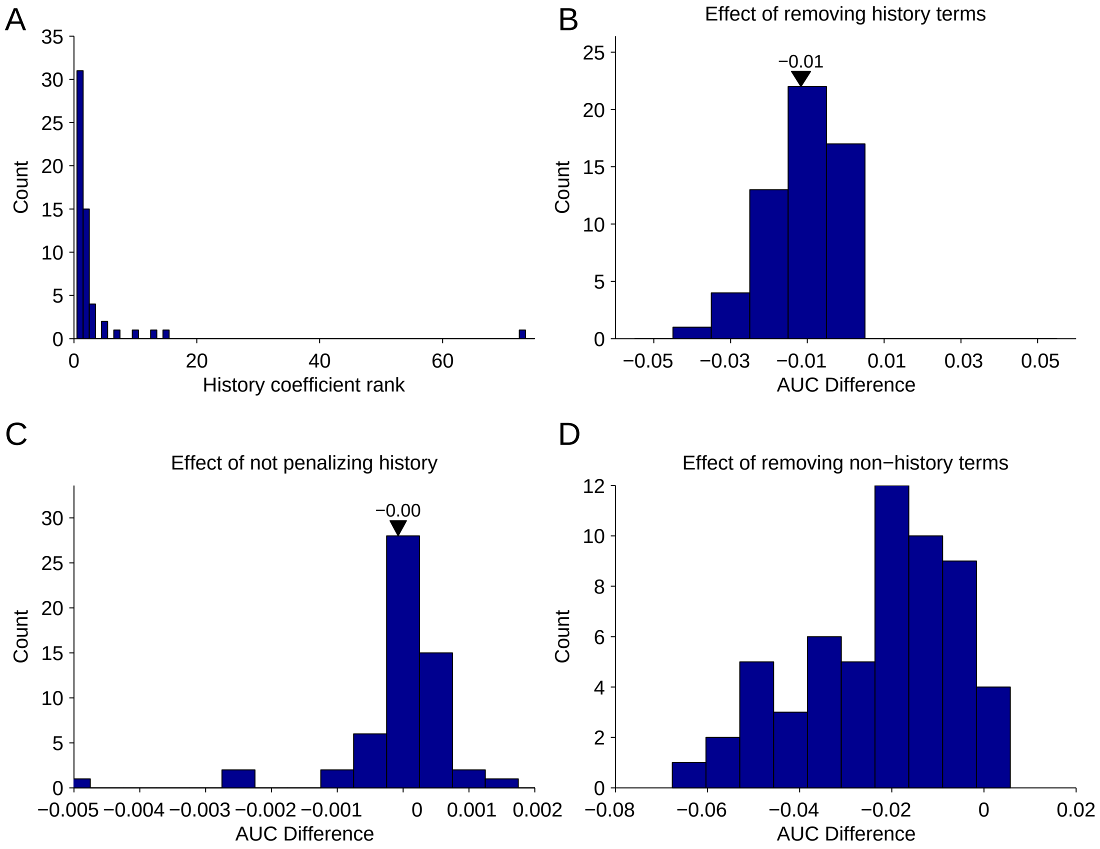

although we do not think it qualitatively influences the results presented.

We also fit models with 3 parameters per cell in the population. Instead of the one parameter for the last 100ms, we used 3 parameters for 0-20ms, 20-50ms, and 50-100ms. These were fit as independent parameters and so the active set could contain none, some or all of these 3 parameters for each cell. The mean AUC across the population was .01 larger with this increased parameter set, but also the mean active set size was 100 elements larger (Figure 5.16A+B). The moderate increase in the AUC is generally accompanied by a doubling of the active set size. This trade-off may not be desired or necessary, since a much more complex model describes the data only marginally better.

5.2.4 Meaning of model parameters

Assessing the models to see which is the best from a cross validation standpoint is only one aspect of this type of modeling; we used the model fits to help draw conclusions about the underlying network.

Connection to CCGs and noise correlation

The noise correlation measure for a given cell pair is also correlated with the model coefficients. This is not a surprising result, since the noise correlation is largely driving the inclusion of large coefficients in the model. We controlled the time scale of correlation by subtracting jitter correction terms, described above. Figure 5.17 shows the correlation between the peaks of the CCGs and the model's coefficients. Also in that plot are the shuffle corrected CCG and the noise correlation. While correlation in the CCGs and the noise correlation generally stays positive across the array, the model's coefficients tend to drop to zero after a millimeter or two. The explanatory power of the nearby units explains the data sufficiently so that the L1 regularization pushes the more distant coefficients to 0.

Dynamics of the coupling terms

For the models fit with multiple time points per network cell, we analyzed the nature of the coefficients across time. First, we found that the coefficients were generally positive, for all three epochs. They also were larger closer to the spike, in the first time epoch (1-20ms). The coefficients for the other two epochs had distributions with similar means (Figure 5.16C). For each cell analyzed, we pooled the coefficients for each time epoch. Then we combined these data across the analyzed units, yielding 7125 data points per

Figure 5.16 A: Histogram of the difference between the AUC with one parameter for each cell (1-100ms history) and three parameters for each cell (1-20ms, 21-50ms, 51-100ms). The increase is significant; about .01 on average. B: Histogram of the active set size difference between the same two parameter sets. The number of set elements increases with the extra parameters by about 100 elements on average. C: Breakdown of coefficient values for the three parameter epochs. These values are taken for all cells analyzed (57), and all neighbors (125), so $n = 7125$. D: Difference between the absolute values of the coefficients, broken down by distance between the cells in question. The two bar graphs here correspond to the difference between the first two coefficients (above) and the last two coefficients (below).

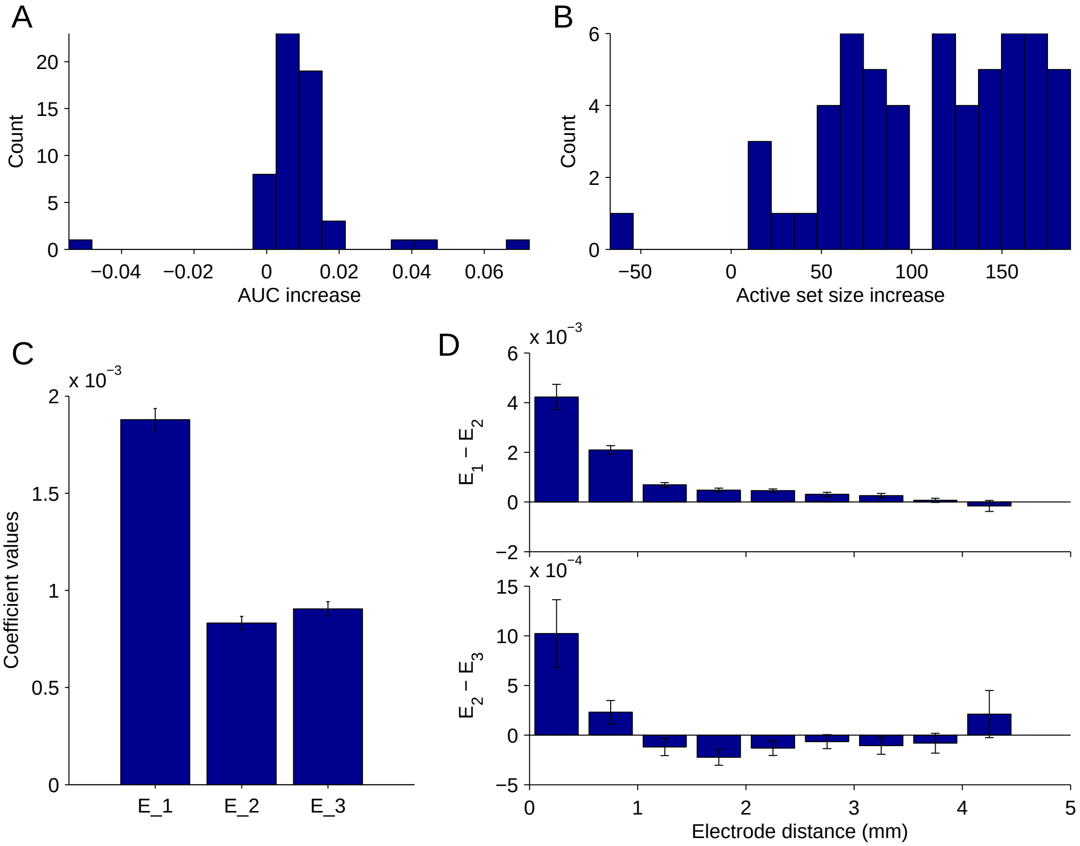

Figure 5.17 Correlation between various correlation measures and coefficients. ”R” is the noise correlation, ”SC” is the shuffle corrected CCG, and the other bars correspond to jitted corrected CCGs of specified jitter window sizes.

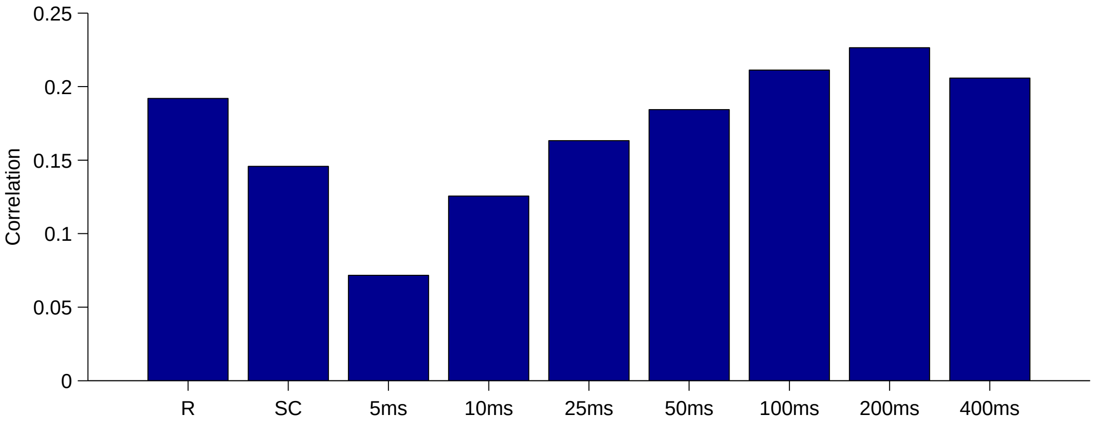

epoch. These models show that the benefit of including data from the cell population falls off quickly with time. We illustrated above the relationship between noise correlation, which seems to drive much of these parameters, and distance. Figure 5.16D shows the difference between the first and second epoch coefficients, broken down by the distance between the electrodes the units in question were recorded from. The difference is large for nearby cells and falls off rapidly for distant cells. Even for these larger distances the coefficients for the first epoch tend to have larger magnitudes than the coefficients from the second epoch. Below is the plot comparing the second and third epoch. Here, for greater distances, the relationship is reversed - the third coefficient is larger than the second on average. This suggests that for large distances ($>$ 1mm), the more distant past (51-100ms) is more informative than the intermediate past (21-50ms). Even for these large distances, however, the immediate past is most informative.

5.3 Interactions between connectivity and receptive fields

We have illustrated the results of modeling the stimulus effects or the coupling effects individually, and in this section we model them together to clarify the relationship between the two types of effects in a neural population. Figure 5.18 shows the connection between the two types of models presented above. Panels A+B show that the models based on stimulus terms are more successful for the cells on the left of the array, with the reverse true for models based on the coupling terms alone. Figure 5.18C is another way to visualize this relationship, in a scatter plot. The inverse relationship suggests that cells fall along a continuum, with cells either being well predicted by the coupling terms, or the stimulus terms, but not both.

To explore further the connection between these two types of terms in GLM models, we fit models with both types of terms to the data. Figure 5.19 shows the way we proceeded in this respect. First, we found the penalty on coupling terms that resulted in the largest AUC for the model with coupling terms alone. This penalty, λ_c, was fixed in the fitting of a full model which contained stimulus terms as well as coupling terms. The plot in panel B shows that there is an improvement in AUC in the full model over either of the more restricted models. For this cell, the AUC is lower earlier in the L1 path (the stimulus penalties are identical in these two cases). Thus, the resulting stimulus model has fewer included parameters in the fitted filter (shown below).

The technical limitations of fitting models to a large number of penalty values precluded us from finding the maximum AUC for these models. In addition, the AUC curves are not convex and have a fair amount of noise, so any maximum AUC cannot be considered the true best AUC. With these caveats in mind, we analyzed the population of cells to learn more about the interactions between the coupling terms and stimulus terms in these combined models. The example in Figure 5.19 shows a cell for which the inclusion of coupling terms reduces the benefit of an increased number of stimulus parameters. This was just one example, but when doing this same analysis for all cells in the population, we found that there were no cells in which the inclusion of the coupling terms increased the benefit of a reduced stimulus penalty on the AUC metric. This indicates that the coupling effects do not mask additional complexity in the stimulus effects. Indeed, for many cells the effect on the stimulus L1 path is that the best stimulus active set is smaller when allowing coupling terms to capture firing of the cell. For 7/57 cells, the best AUC in the stimulus path of the combined model was when all stimulus terms were excluded from the model. In these cases, there was no improved performance of the model beyond the coupling terms. As expected, the cells for which the stimulus terms dropped out or were reduced were also cells with high coupling AUC and low stimulus AUC values.

5.4 Discussion

We found that it is possible to fit models with stimulus parameters or spike coupling terms. The goodness of fit varies a great deal with the specific cell modeled. For some cells, the stimulus carries the most information about spiking, while for others the spike coupling

Figure 5.18 A+B: The maps in electrode space of the AUC values for all units. Here the AUC values for the stimulus and coupling models are shown. They have opposite patterns across the array. C: The AUCs for the stimulus model is plotted against the AUCs for the coupling models. They exhibit an inverse relationship. D: The normalized difference between the two model types is plotted in electrode space. The normalized difference is given by $\frac{AUC_s - AUC_c}{AUC_s + AUC_c}$.

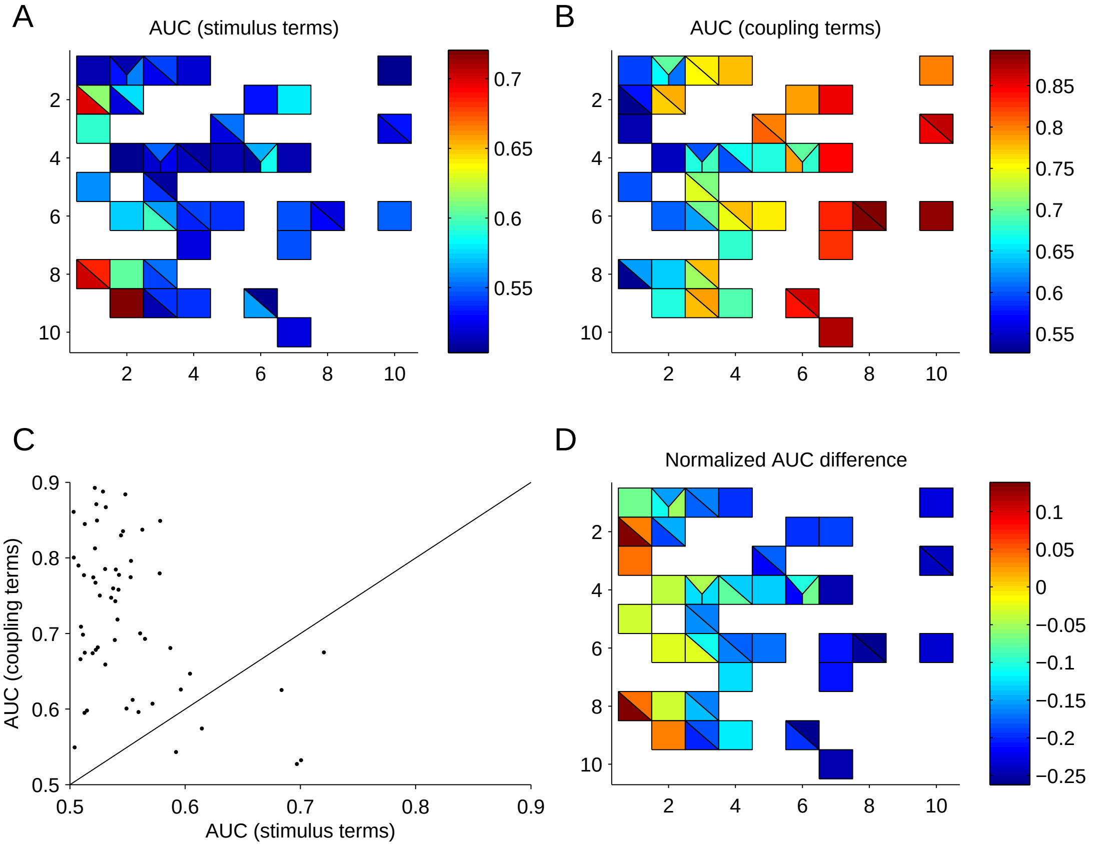

Figure 5.19 A: The penalty that corresponds to the highest AUC for this cell is circled in green. At the right is the coefficient map, in electrode space. Coefficients which are zero are colored gray. B: Two other model fits are shown here. The red curve is the AUC for the model built with stimulus terms only. The blue curve is the AUC corresponding to the model fit with coupling terms and stimulus terms. The coupling penalty is fixed at the same penalty that is circled in green in (A). For this cell, the AUC is larger for a smaller stimulus penalty, and as a result the number of terms included in the stimulus filter is smaller (below).

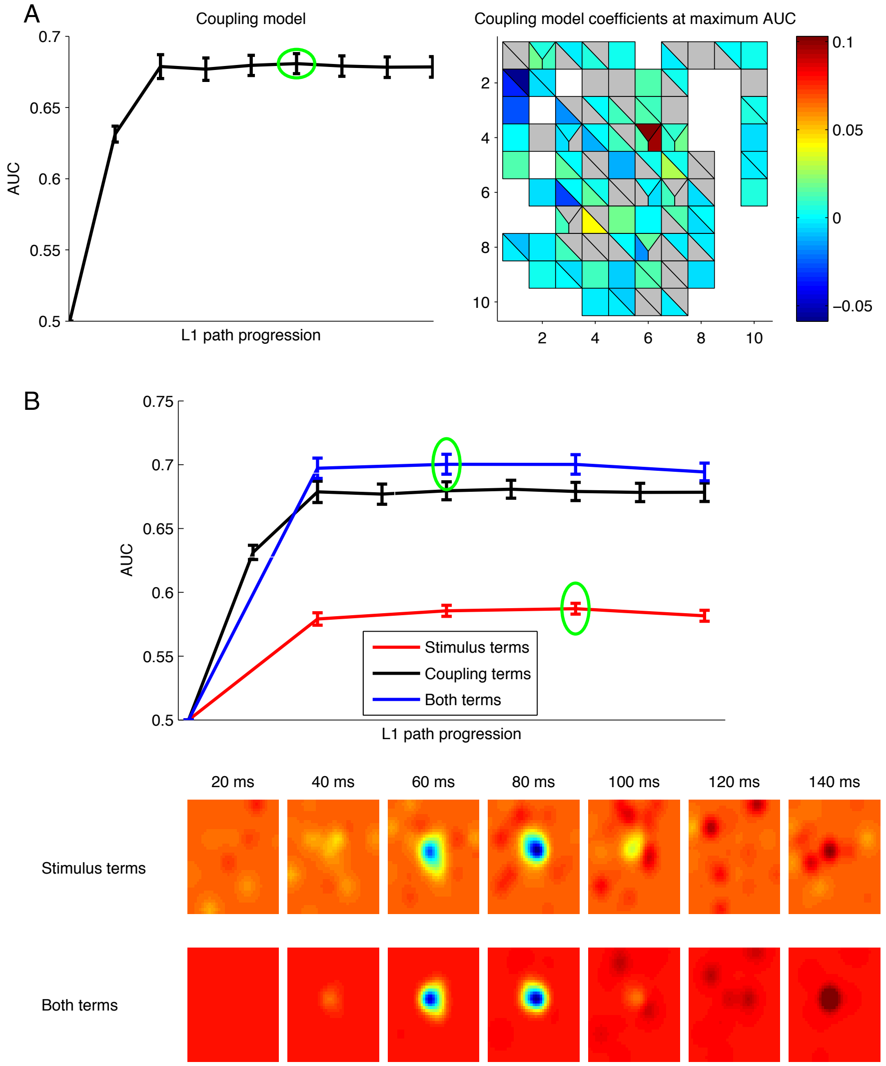

Figure 5.20 The effect of adding coupling terms to the stimulus models changes the necessity of stimulus parameters in the models. For some cells, there was an increase in the best (in relation to the AUC) L1 penalty for the stimulus parameters when including the coupling terms. For no cells did the model require a smaller L1 penalty to achieve maximum AUC after this inclusion. For some cells the best penalty was unchanged, and the cells for which it did change tended to be the ones with high coupling model AUC.

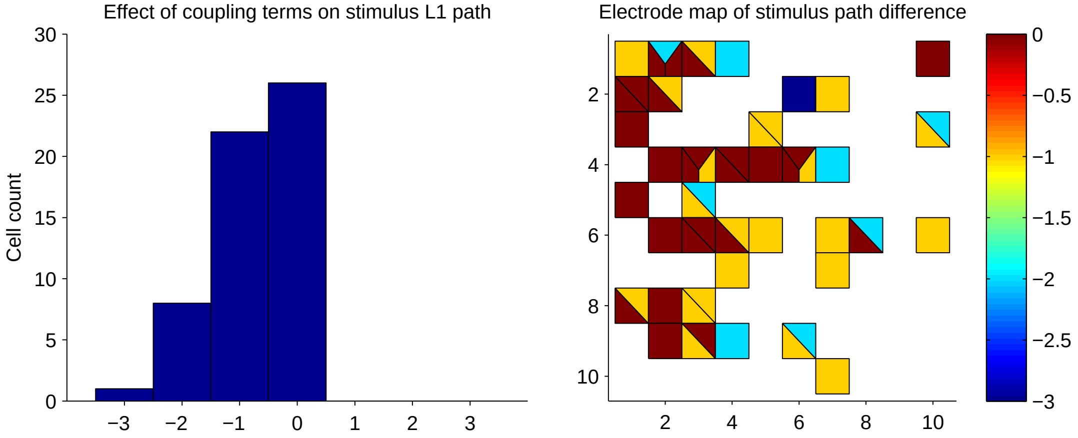

terms contain more relevant information. There was a strong effect of array location on the place each cell fell on this spectrum. We speculate that such a difference may stem from electrodes on different sides of the array sampling from different cortical layers. Unsurprisingly, the model parameters are well correlated with classical measurements of stimulus and spike coupling relationships. The stimulus coefficients correlate with terms from the spike-triggered average stimulus, and the spike coupling coefficients correlate with the corresponding pairwise noise correlation and cross-correlograms. One main difference in these measurements is that the L1 constraint encourages sparseness of nonzero coefficients, especially when the coefficients are correlated as many of these data are.

One striking difference between the stimulus and spike coupling models is that the AUC values for the well-fit spike coupling models are very high - up to .9. The stimulus models peak at .72 and most cells have AUC $< .6$. This does not necessarily indicate that the coupling effects are greater than stimulus effects. It is very likely that the the network may simply carry more information about the particular cells we have recorded. There is an orthogonal explanation as well: the linear models we have chosen to use to model the stimulus may not be appropriate in modeling most of the cells in the population. We could use this same framework to compare different kinds of models, in particular models of complex cells.

If the spikes due to the stimulus and the spikes due to the coupling terms were completely independent, the AUC values of the different models would sum in a combined model. We find that the AUC values do increase somewhat in a combined model, but are never the sum of the two individual AUC models. That is, the spikes do not belong to either one effect or the other, and can be related to both effects. For many cells, the stimulus coefficients are actually reduced, indicating as in the Chapter 4 example that some purported features of the STRF as given by the STA are better explained by other cells in the network than the stimulus terms. For other cells, the stimulus terms drop out completely of the model containing spike coupling terms. We can conceptualize that these cells are receiving the outputs of other cells which have stimulus effects, and their STAs are reflections of these network inputs.

Chapter 6

Network states

In the last chapter we showed that in predicting the firing of a neuron with a GLM, the simultaneous activity of other cells in the neural population can have a large impact on predictive power. In this chapter, we test the hypothesis that this performance is a consequence of the shared "noise" introduced in Chapter 3. We compare the performance of the spike coupling model investigated in the last chapter against GLMs built with LFP measurements indicating the general network state. We explore different aspects of the LFP (LFP value, LFP power in frequency bands, and LFP phase), and find that LFP value and power in the gamma band provided the most information relative to spiking activity. We find that models of LFP power and value are just as informative as models of spike coupling and history, suggesting that the effects of the network can subsume much of the power of spike coupling models.

6.1 Local field potentials

We introduced the LFP in chapter 3 as a signal which is measured from extracellular electrodes, and which generally is thought to reflect the average synaptic input to a region of cortex. In our context, the LFP is a time series sampled at 1KHz. Figure 6.1 shows an example of one of these recorded signals. Our recordings are from a 96 electrode array, and we have recorded one of these traces from each of the electrodes. The signal is highly correlated across a relatively large region of cortex, up to many millimeters. Figure 6.2A shows the LFP value for each of the 96 electrodes over 10 seconds during the presentation of gaussian white noise. Large fluctuations are shared on most electrodes in the population. The LFP also varies slowly with time, and exhibits a large amount of temporal correlation on the scale of hundreds of milliseconds. Figure 6.2B shows the normalized autocorrelation function for one specific electrode's LFP. This electrode is representative of the population, and all electrodes show this trend and qualitative temporal profile. Figure 6.2C shows that correlation between electrodes is very high for nearby electrodes, and falls off with distance, although it remains highly significantly positive at the extent of the array's width.

The relationship between the LFP value and the stimulus is much less strong. Figure 6.3A shows the LFP value on a single electrode over the course of 120 presentations of the same 10 s gaussian white noise movie. It is difficult to easily see any repeated stimulus related features in this figure. We computed the trial averaged LFP for this electrode, as well as the standard deviation (σ), and those two values are plotted in Figure 6.3B. Here we define SNR to be the ratio of the mean LFP value to the standard deviation of the signal – mean. The ratio is well below 1, indicating that the variability due to the stimulus are dwarfed by the extra-stimulus signal. Figure 6.3C shows the values of this SNR ratio for these 10 s. The other electrodes in the array show the same trend during white noise stimulation.

One popular method for analyzing the LFP is frequency analysis. Gamma oscillations have received a great deal of attention from many labs. The gamma activity in the LFP has been found to contribute to the BOLD response of fMRI (Logothetis et al., 2001). Also, power in the gamma frequency band is related to spiking activity (Henrie and Shapley, 2005; Rasch et al., 2008). Low frequency oscillations, however, spread farther across cortex and have greater power than the faster oscillations (Leopold et al., 2003). Figure 6.4A shows a 5 s LFP trace and its corresponding power spectral density for a single electrode. We computed the coherence between every pair of LFPs and plotted the coherence in 7 frequency bands against distance. For all frequency bands, the coherence decreases with increasing distance, and the coherence in lower frequencies persists over longer distances than the coherence in higher frequencies.

Rasch et al. (2008) has also shown a relationship between spiking and the phase of the slow oscillations in the LFP. They used a low-pass Kaiser FIR filter with a cutoff of 2Hz or 4Hz. The phase was obtained with the Hilbert transform of this low-pass signal. Figure 6.5 shows the results of the same transform on the LFP from a single electrode.

6.2 Modeling the network state with LFP

We modeled the relationship between LFP value and spiking activity for the same cells as in the previous chapter. We considered models of the network state using the measures

Figure 6.1 Examples of LFP values. A: The LFP trace of a specific electrode (1ms resolution) for 5 seconds. Both slow and fast fluctuations are apparent in the signal. B: Variations in the spatial LFP map. For 4 specific times in the trace above (1s, 2s, 3s, 4s), the LFP is shown for the entire array. Though there is a large amount of correlation between nearby electrodes, complex patterns are evident.

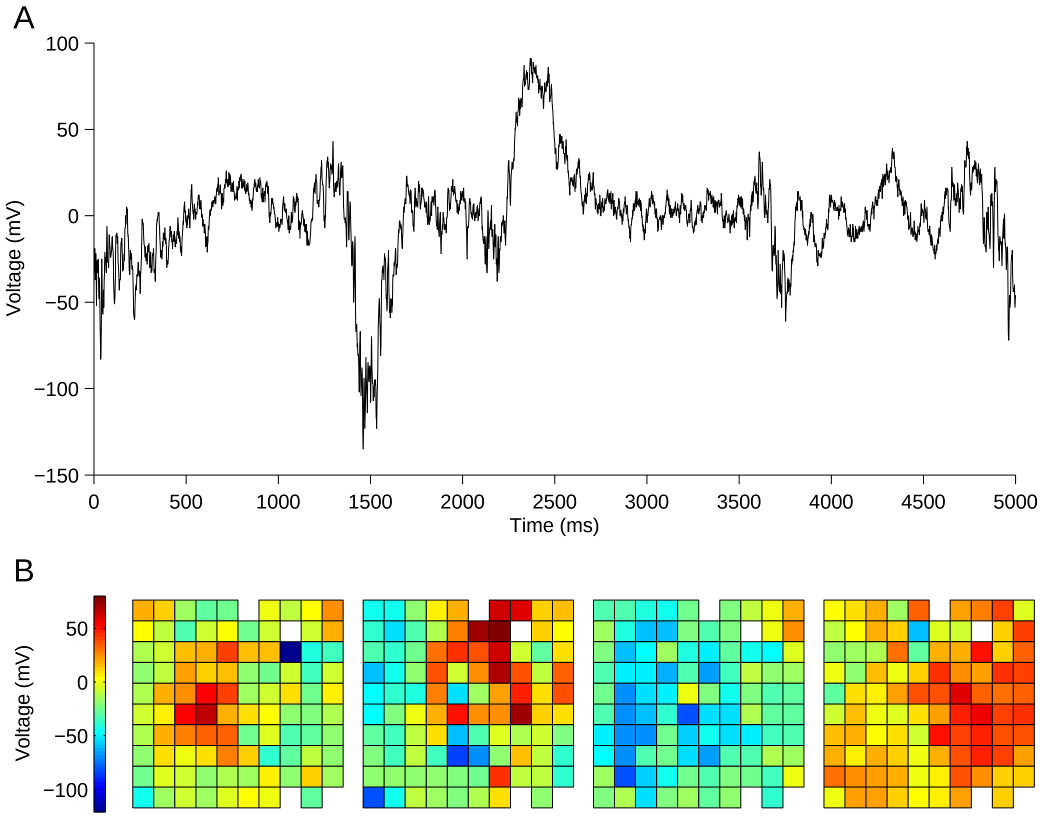

Figure 6.2 Spatial and temporal correlation in the LFP. A: The LFP values for the 96 electrodes (randomly ordered) during 10 s of white noise stimulation. Correlation is visible across the electrodes and also in time. B: The autocorrelation function for the LFP recorded on a single electrode. The autocorrelation is normalized so that the correlation at 0 ms lag is 1. C: Correlation between LFP time series' on distinct electrodes. For a given pair, the correlation coefficient is calculated between the two series of 10 s (10,000 samples). The correlation coefficients are grouped according to predefined distance bins. Standard error of the means are also shown.

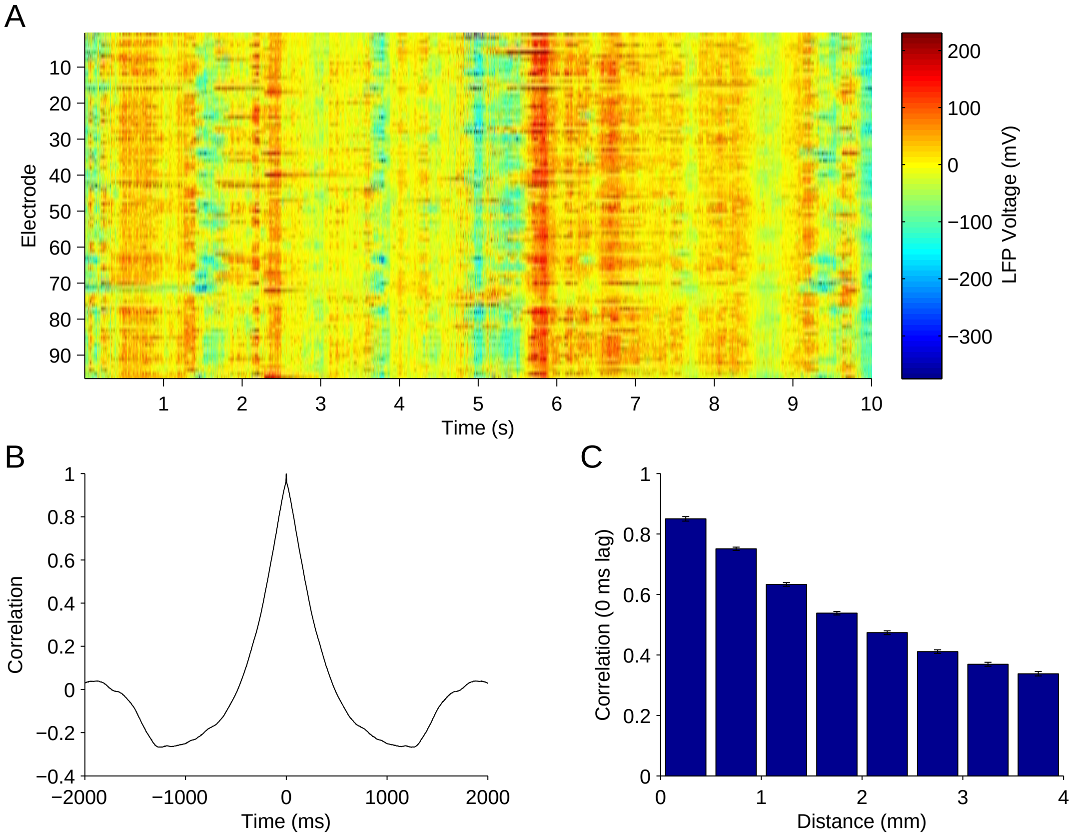

Figure 6.3 Effect of white noise stimulation on the LFP. A: For one electrode, the LFP is shown for 120 repeats of a 10 s white noise movie. Very little correlation is visible across trials. B: The trial averaged LFP is plotted in black, and hovers near 0. The standard deviation across trials is plotted in red. C: Histogram of the SNR measurement, μ/σ, for each time point shown in A and B. Other electrodes in the population follow this same trend.

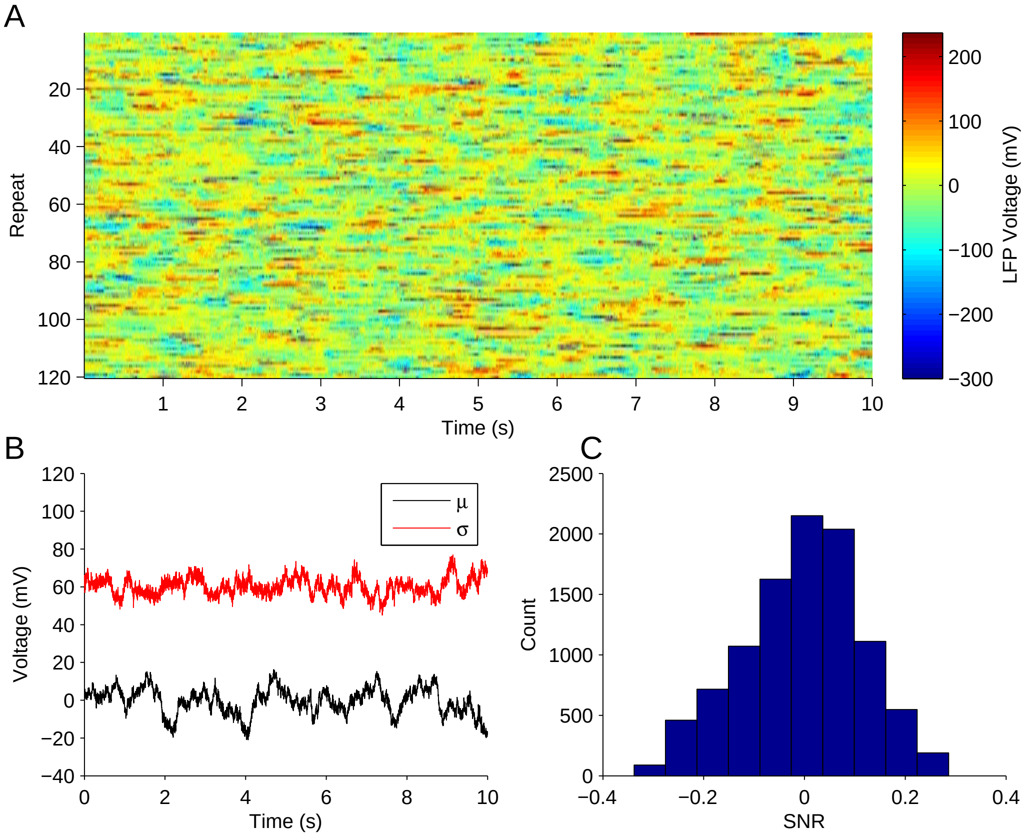

Figure 6.4 A: The LFP for a single electrode during the presentation of Gaussian white noise, and its power spectral density. B: The average LFP coherence for 7 frequency bands, for different distance bins.

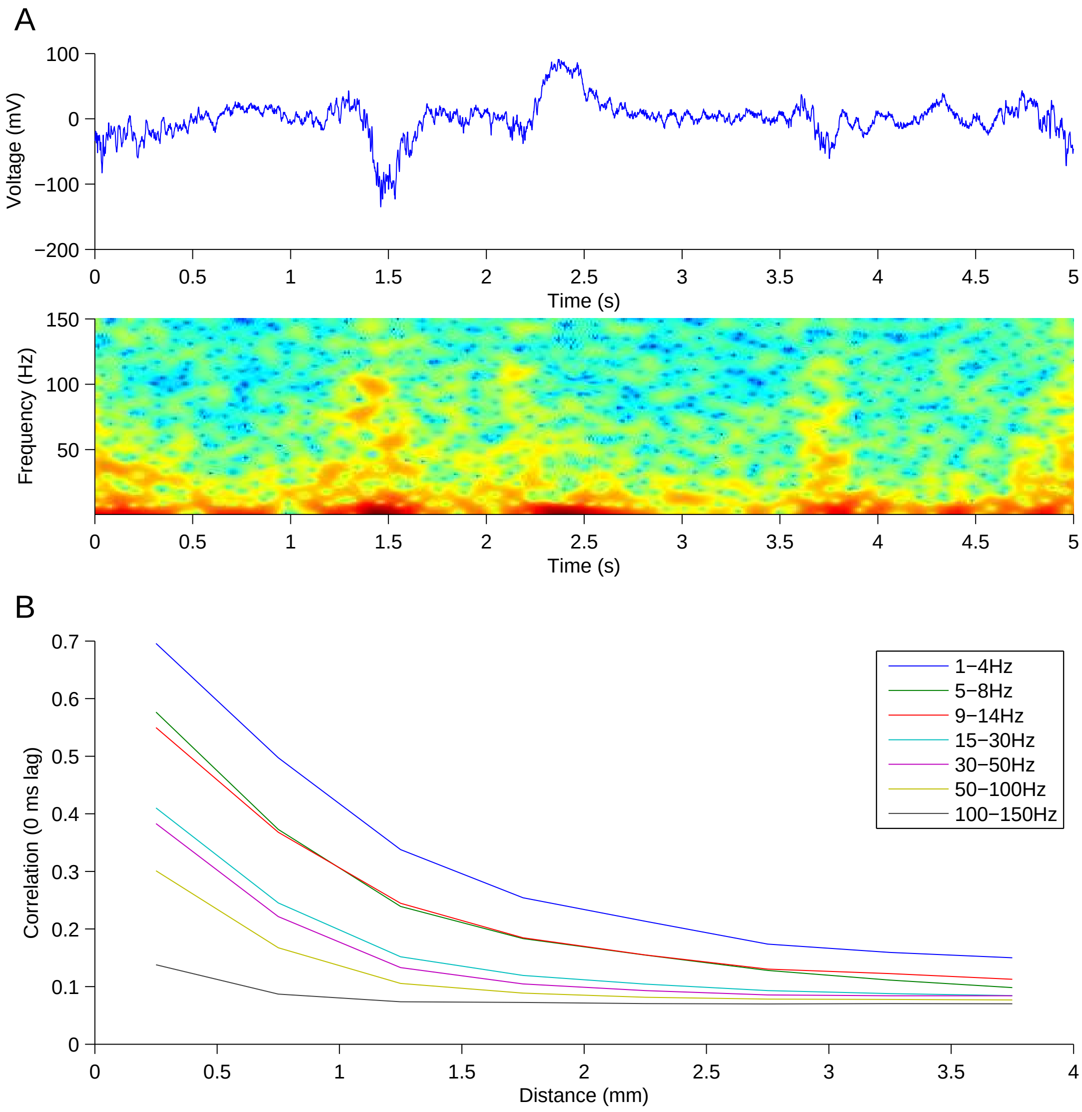

Figure 6.5 The LFP is plotted for a single electrode, and the background is colored with the phase. The phase is computed by first low-pass filtering the LFP (2 Hz) and then taking the Hilbert transform of the low-pass LFP.

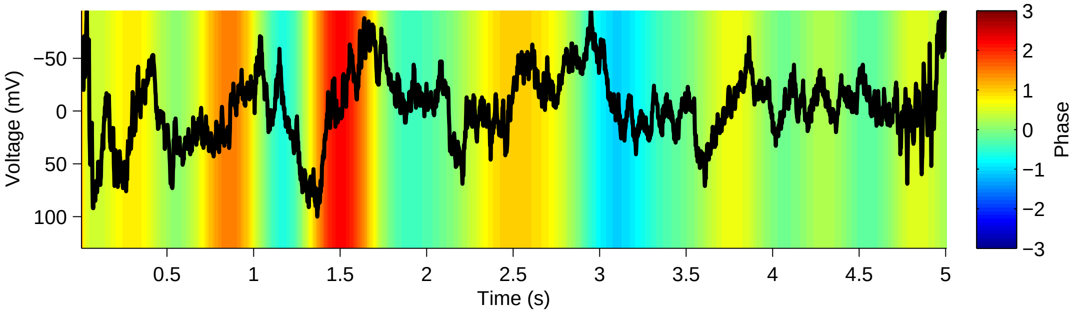

explored above. We also build a Hidden Markov Model (HMM) using the LFP as an illustration of how more complex nonlinear models of the network state can fit within this framework. We show results from GLM fits using the following network state surrogates:

- LFP value
- Power in LFP frequency bands
- Phase and power
- HMM built from the LFP

6.2.1 LFP value model

We fit the 57 units to two different models of the LFP. In the first model, each electrode in the 96-electrode array was considered to be a single variable. Since the spike trains are binned at 10ms, we also binned the LFP at that resolution, averaging the 10 data points together to form a 10ms resolution time series the same length as the spike train data. The model is thus

$$\log \mu(t) = \sum_i \beta_i v_i(t-1) \tag{6.1}$$

where v_i is the LFP value. Before fitting, we standardized the LFP values to have mean 0 and variance 1.

Figure 6.6 The fitting of one example cell. Above are the maps of coefficients paired with LFP electrode location. The location of the cell is marked with an X. Below is the AUC for the corresponding model fits.

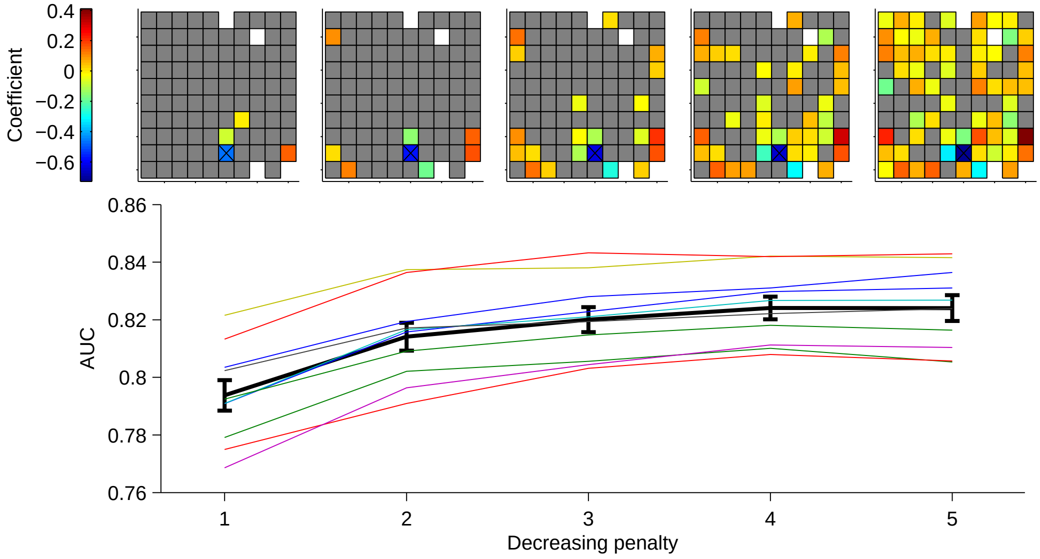

Figure 6.6 shows the result of fitting such a model to an example cell's spiking activity. Shown are the β_i values to each of 5 L1 penalties, with the largest penalty on the left. As with the spike coupling model presented in the previous chapter, the impact of the LFP value tends to be larger for nearby electrodes, with one large coefficient and many smaller ones. This reflects the spatial correlation in the LFP between nearby electrodes. In fact, there is so much correlation, that overfitting does not occur until almost all the terms are included in the model. Most of the included coefficients have low values.

In terms of the population, the location in the array was again related to the maximum AUC values. The cells toward the left of the array were not well modeled with the LFP value, while cells toward the right of the array were easily modeled (Figure 6.7A). This is quite similar to the AUC values for the spike coupling models, and we also compared these LFP models to the spike coupling models presented in the previous chapter. Figure 6.7B shows this comparison. The mean difference between the spike coupling models and the LFP value models was low (.01) but significantly different from 0 (paired t-test). Though the models have slightly different numbers of terms (LFP value models have 96 terms while the spike coupling models have 128), this is not the reason for the difference, since the spike coupling models usually contained fewer nonzero coefficients after fitting.

The coefficients for the model are shown with respect to distance in Figure 6.7C. These are the coefficients for all electrodes and all cells. The same electrode pairs (distance = 0) have larger, negative values. This reflects the correlation between the negative LFP value and spiking. The variance in the coefficient values falls off with increasing distance, with distance electrodes providing relatively less information about spiking. Figure 6.7D is another way of looking at the data in panel C. It is an analysis of the inclusion of terms in the model. The bars indicate, for each group of distances, the percentage of the coefficients that are nonzero. The nearby electrodes are almost always nonzero, and at distant electrodes many more coefficients are excluded. The falloff occurs by 1.5mm; e.g. there is just as much likelihood of a nonzero coefficient at 2mm as at 4mm. Though, from (C), the values decrease at these distances, even if the percentage of nonzero elements remains the same.

Recall that in the spike coupling models, we achieved a greater AUC when expanding the model to multiple time windows. We provided the models with 3 terms per other unit corresponding to 1-20ms, 21-50ms, and 51-100ms instead of one term corresponding to 1-100ms. The improvement was small, but significant. We explored the same issue for the LFP value models. We used the model

$$\log \mu(t) = \sum_i \sum_\tau \beta_{i\tau} v_i(t-\tau) \tag{6.2}$$

where τ ranges over $\{1, 3, 5, 7\}$, which correspond to 10ms, 30ms, 50ms, 70ms.

Figure 6.8 shows the same cell as Figure 6.6, but this time with the coefficients corresponding to the LFP value contribution at a specific time before the spike. As in the more restricted model, the largest coefficients were nearby electrodes to the electrode recording the unit in question. In addition, the most recent time bin (10ms) had the largest coefficients, and were also revealed first in the L1 path. For this cell, the AUC was not changed appreciatively, even while the number of included parameters jumped by a factor of 3.

Across the population, this expanded model showed very similar characteristics to the simpler, 1 time point example. Figure 6.9 summarizes some of the comparisons between the two models for the population. Panel A shows the AUC across the array for the expanded model, which is very similar to Figure 6.7A. In panel B, we confirm this similarity, as the two AUC measures across the population are very similar. Though a paired t-test confirmed an increase in AUC ($p < .0001$), the mean shift in AUC was only .0033, a very small amount. In addition, the shift was mostly driven by the cells with relatively low AUC values, so for most of the population the shift was even smaller. Panel C confirms the result from Figure 6.7C, and though there are many more points here, the basic finding is that nearby electrodes record LFPs which are relatively more informative about spiking.

Figure 6.7 LFP value model across the population. A: AUC values for each unit determined by models fit with LFP values. B: Comparison between AUC of the LFP model and the AUC of the coupling model. Both models are fitted with one coefficient per electrode or unit. The coupling model is somewhat more predictive on average. C: For each unit fit, the coefficient corresponding to each electrode is shown, with the x-axis indicating the distance between the unit's electrode and the LFP electrode. D: The values in (C) were binned according to distance, and the percentage of nonzero coefficients in each bin is shown on the y-axis.

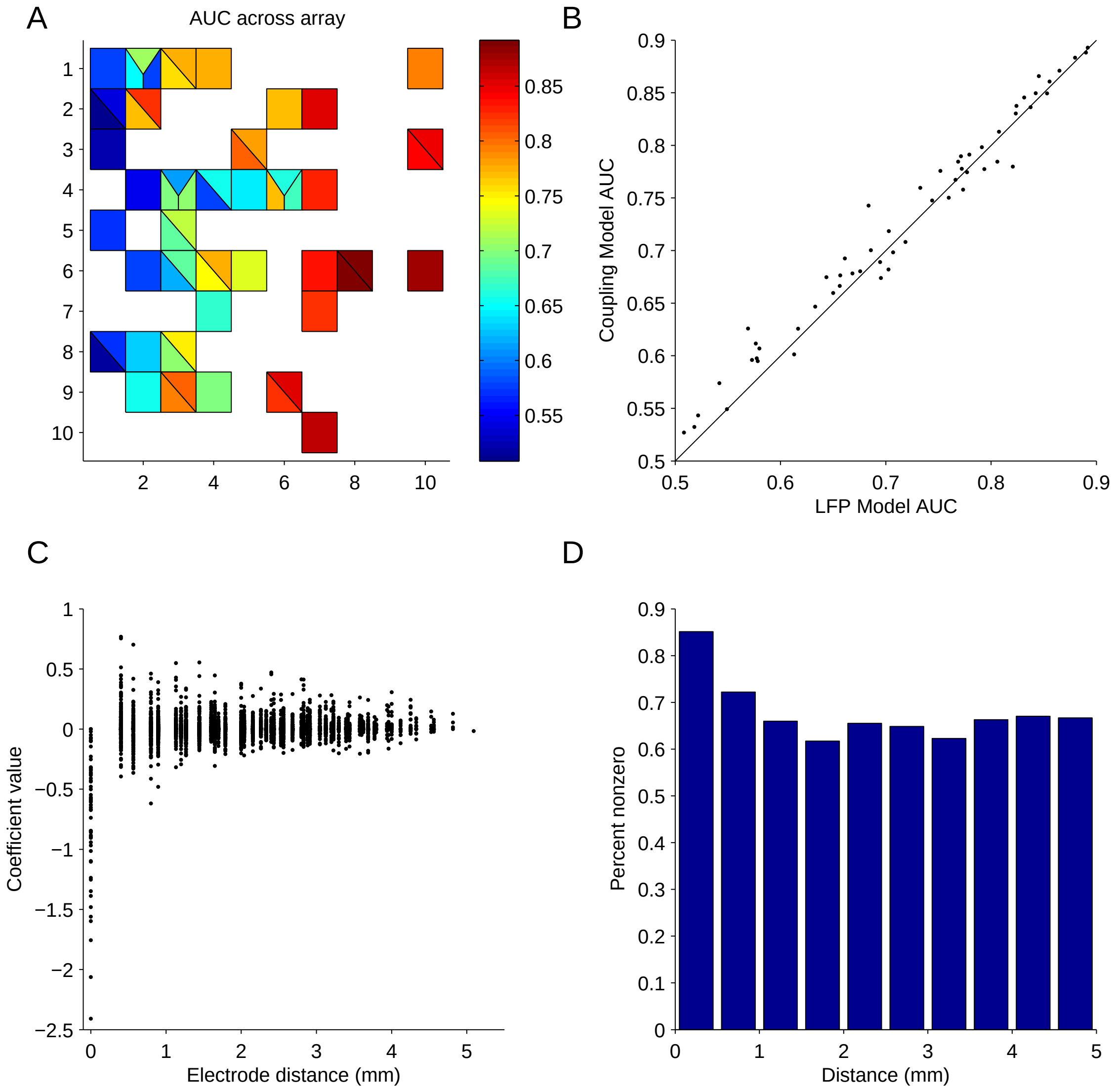

Panel D shows the breakdown of included coefficients by time point. For the 10ms term, more than half the coefficients are nonzero on average, with a falloff in time. There is an increase at 70ms. This can be explained by the large amount of correlation between these time points - most information conveyed by the 30ms term has already been explained by the 10ms term of the same electrode. There is a bump at 70ms for the same reason - anything that was informative beyond 70ms is best captured by the 70ms term as opposed to the other terms.

6.2.2 LFP PSD model

Since the power in different frequency bands has also been shown to correlate with spiking activity, we prepared a model of spiking due to the power spectral density (PSD) in the LFP. The model is

$$\log \mu(t) = \sum_i \sum_f \beta_{if} P(t, f) \tag{6.3}$$

where P is the mean power spectral density at time t over the frequency range f. Figure 6.10 shows the same example cell as in the previous two examples. It is clear that the gamma band (30-80Hz) contains the largest and most effective terms in spike prediction, with the other bands including terms mainly when the model is over-fitting. Also notable is that for this cell, the AUC is higher than the LFP value models above, and that high level of fitting is possible for only a small number of terms.

In general, the results for this model are very similar to all the extra-stimulus models presented so far. Figure 6.11 shows that the array map looks very similar as previously shown. We could not distinguish between the AUC distributions of the 3 term coupling model and the LFP PSD model with a paired t-test. However, panel B shows that the difference between the models in terms of AUC is related to the AUC values: low AUC cells are better explained by the coupling model and high AUC cells generally better explained by the PSD. A difference between this model of the LFP and the ones above is that we excluded the PSDs from the same electrode, a disadvantage for this model over one that includes the terms. We did this to avoid any waveform bleed-through. Panel C shows the falloff of the coefficient values with electrode distance. Here, the highest values are spread over the first 1 mm, since there are no 0 mm data points due to the exclusion of “same” electrodes. The pattern remains the same, with local electrodes providing the most influence in the models. Panel D shows that for the model fits, the gamma band coefficients are more likely to be included in the models.

To test the contributions of the two lower frequency bands, we fit models to gamma band terms only, and compared the AUC values between the two models. We found no

Figure 6.8 The fitting of one example cell to an LFP value with 4 independent time points. Above are the maps of coefficients paired with LFP electrode location. The rows correspond to LFP terms given at different time lags relative to the spike times. The location of the cell is marked with an X. Below is the AUC for the corresponding model fits.

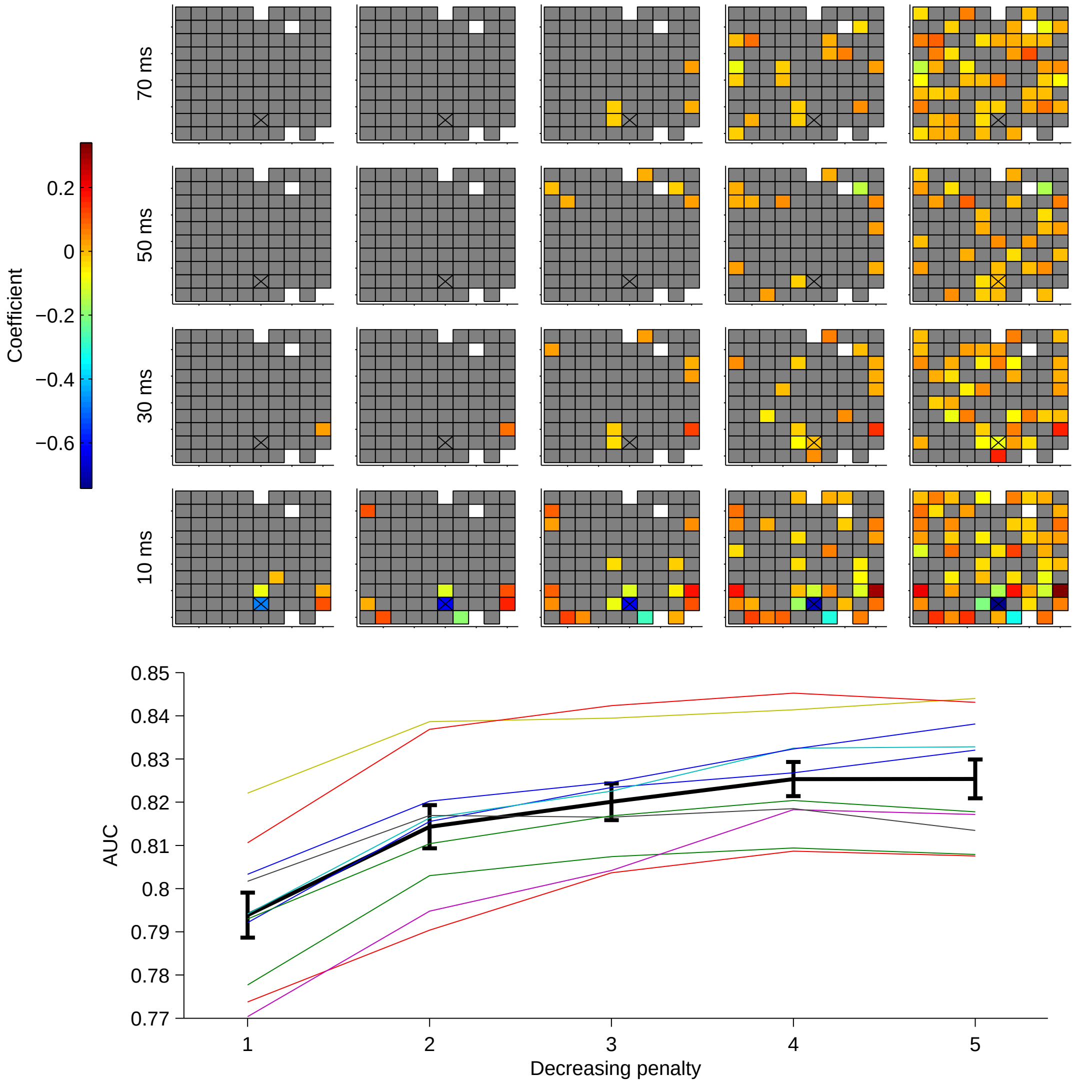

Figure 6.9 LFP value model with 4 independent time points across the population. The model consisted of 384 terms; the LFP values at 10ms, 30ms, 50ms, and 70ms for each of 96 electrodes. A: AUC values for each unit determined by models fit with LFP values. B: Comparison between AUC of the LFP model with 1 time point (10ms) and the model with 4 time point terms. The distribution corresponding to the expanded model has an AUC which is .0033 higher on average. C: For each unit fit, the coefficient corresponding to each electrode is shown, with the x-axis indicating the distance between the unit's electrode and the LFP electrode. D: The average percentage of nonzero coefficients for each time lag. Recent LFP values provide the most information about spiking.

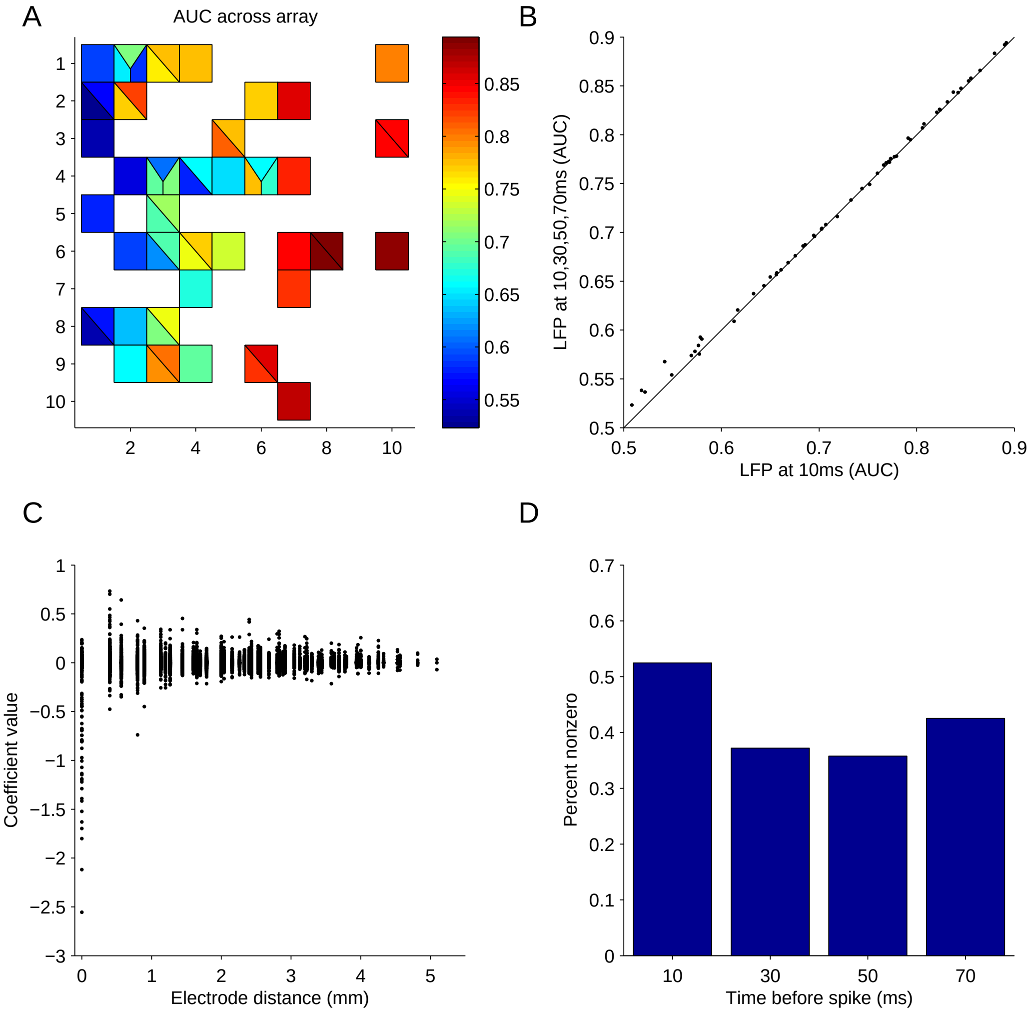

Figure 6.10 The fitting of one example cell to the LFP power in different frequency bands. Above are the maps of coefficients paired with LFP electrode location. The rows correspond to LFP terms given at different frequency ranges. The location of the cell is marked with an X. Below is the AUC for the corresponding model fits.

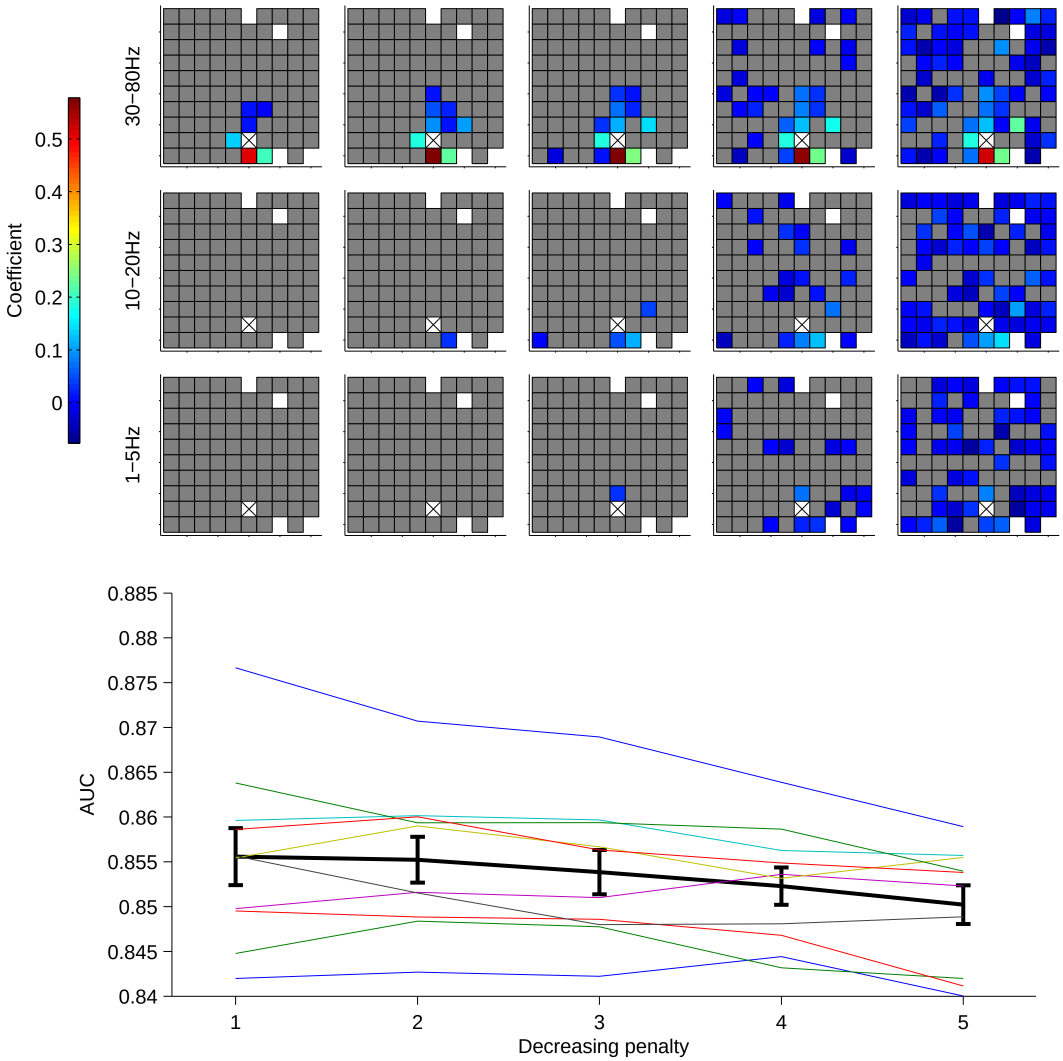

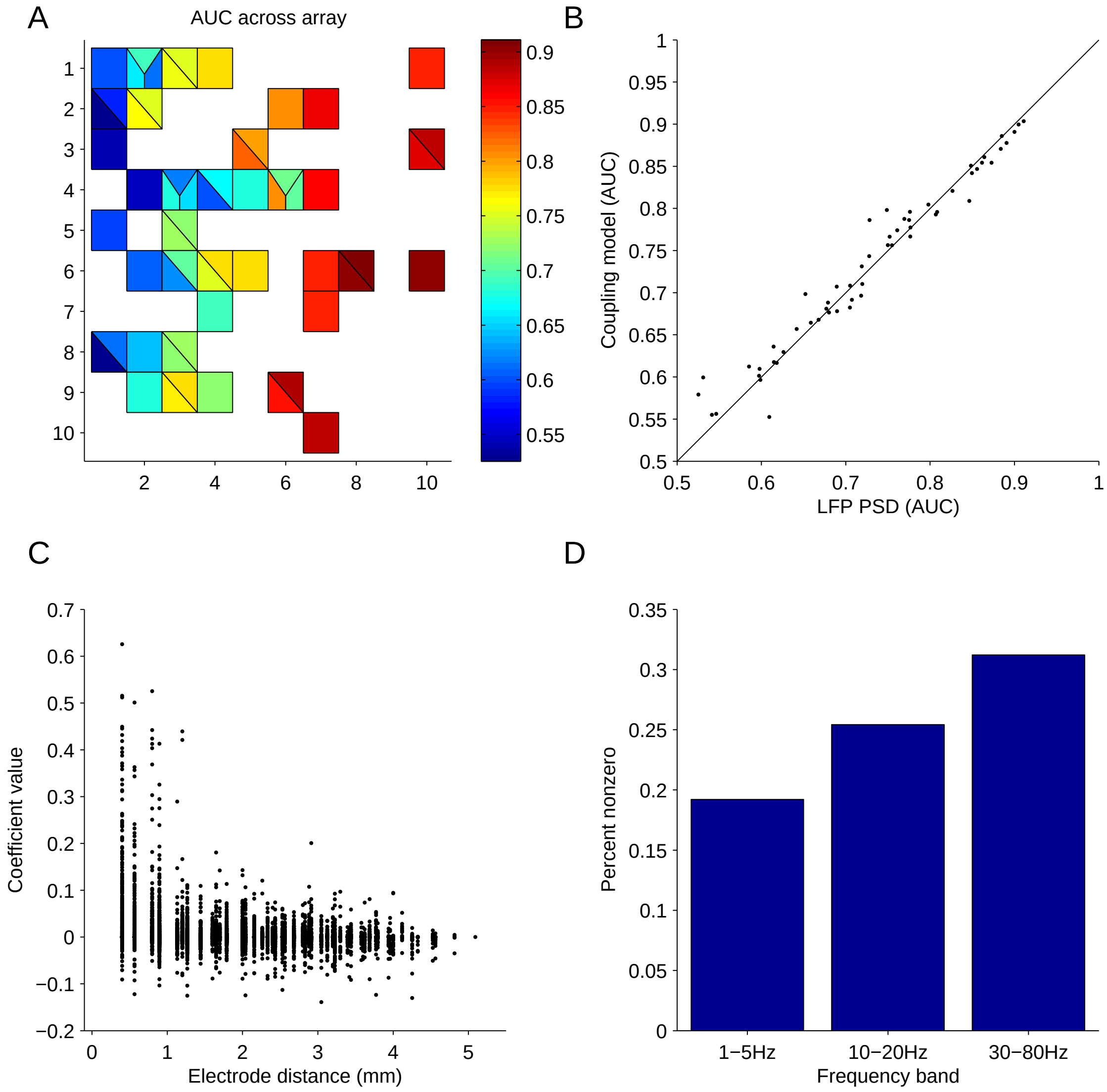

Figure 6.11 LFP PSD model across the population. The model consisted of terms for each of 3 frequency bands and 96 electrodes. A: AUC values for each unit determined by models fit with LFP values. B: Comparison between AUC of the coupling models and the LFP PSD models. C: For each unit fit, the coefficient corresponding to each electrode is shown, with the x-axis indicating the distance between the unit's electrode and the LFP electrode. D: The average percentage of nonzero coefficients in each frequency band. Frequencies in the gamma range provide more information about spiking, on average.

significant difference between the AUC distributions using a paired t-test, and thus the gamma band only model is sufficient for capturing the available information without requiring the other frequency band terms.

6.2.3 LFP phase

We also fit models including the phase of the low frequency signal, which may be related to temporally-clustered spiking activity. We followed the procedure of Rasch et al. (2008) here, first low-pass filtering the LFP signal with a pass-band of 4 Hz, and then and then taking the Hilbert transform of this slowly varying signal to arrive at an instantaneous measure of the phase for each electrode. We fit both the PSD and the phase simultaneously. Figure 6.12 shows the fitting of these terms for one cell. The phase does not have a large impact on spike prediction when considered alongside the PSD. As with the other terms, the terms which are included in the models tend to be from nearby electrodes.

In these combined phase and PSD models, PSD coefficients were more likely to be nonzero than terms from the phase across the population (Figure 6.13A). The included phase terms also did not increase the AUC values in the population. We compared the performance of the PSD only models to the PSD and phase models (Figure 6.13B) and there was no significant difference between the two AUC distributions (paired t-test).

6.2.4 Network state HMM

The GLM can accept any vector of observations, but we are not limited to passing in simple manipulations of the LFP. We can build any kind of nonlinear model based on the LFP and fit the GLM from that model instead. As an example of this versatility, we modeled the evolving LFP with a Hidden Markov Model. Many decisions needed to be made about the specific algorithm to use, the number of states, and the observation models. We chose to model the LFP value and power in the gamma band (a 192 dimensional space). We fit an mixture of gaussians HMM with 25 states using expectation maximization. The states emit observations according to a mixture of Gaussian distributions. Rabiner (1989) provides a full treatment of the HMM. After building the HMM, we found the most likely sequence of states given the data, which is known as the Viterbi path. If the path is $a(1), a(2), \dots a(T)$, then we define the state variable x as

$$x_i(t) = \begin{array}{ll} 1 & \text{if } a(t) = i \\ 0 & \text{otherwise} \end{array} \qquad \begin{array}{r} (6.4) \\ (6.5) \end{array}$$

Figure 6.12 Model fit for a single cell with LFP PSD and phase. Above are the coefficient maps across the array, and below is the regularization path AUC curve. The rows correspond to the different coefficient sets: LFP phase, and PSD over 3 different frequency bands. For this cell, very few phase coefficients were useful in comparison to the PSD coefficients.

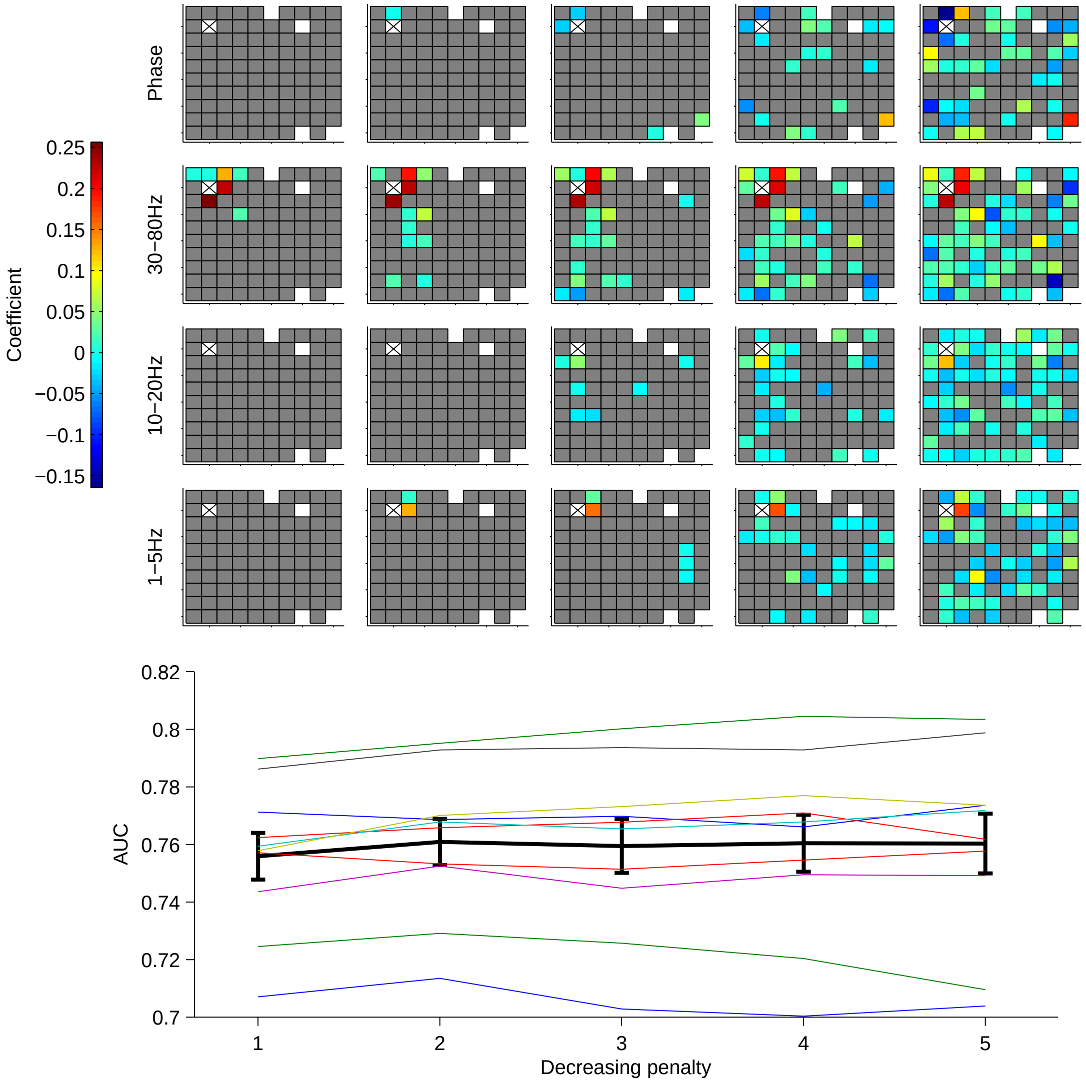

Figure 6.13 LFP phase terms contribute little to PSD models. A: For the models of PSD and phase, the percentage of nonzero coefficients of each type are shown. PSD coefficients include all three frequency bands. B: AUC comparison between PSD model alone and PSD and phase model. We found no difference between the two AUC distributions with a paired t-test.

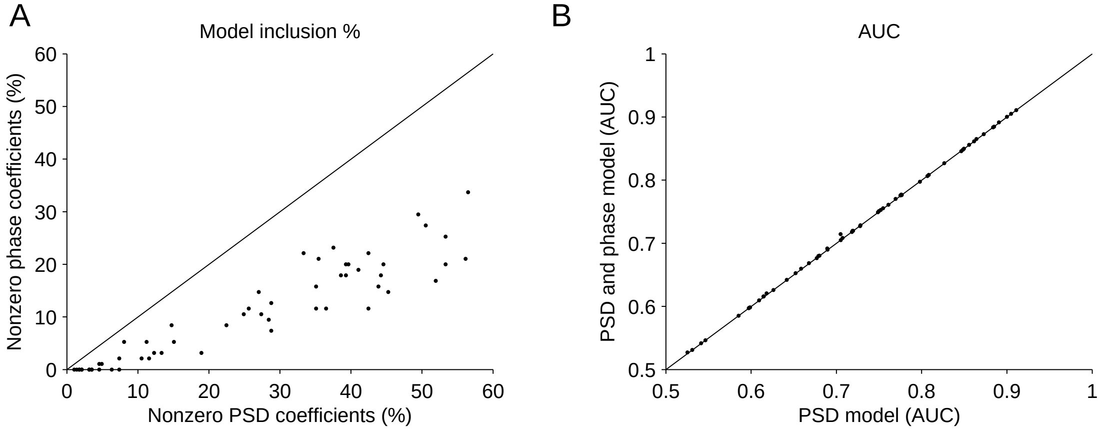

x is thus a 25 dimensional binary variable. We proceed by fitting the GLM to this state variable as before. Figure 6.14A shows the responses of the population of 57 cells for 10 s, with the corresponding state variable below. Each variable shares the same sequence of states. For illustration, we sorted the states according to their influence on the firing rate of the best fit cell. Figure 6.14B shows that the fitting performance shares the same spatial pattern as the other network models on the array. This kind of model produces smaller AUC values than the other models we have been fitting, and Figure 6.14C has a comparison between the AUC values of this model with the AUC from the PSD and value models.

This section is intended to be an example of the way that more complex nonlinear models of the network state can be incorporated into the GLM framework. The reduction in dimensionality improves the run time and memory requirements of the GLM fitting, but in this case the model of the network state is inferior. We have shown that distance in the array is a critical factor in the correlation between cell firing and LFP measurements, and it is likely that amount of this information is diminished in the HMM. A full exploration of the information that different HMMs provide is beyond the scope of this work, but the ability for this 25 state HMM to predict spike trains reasonably well in the GLM context is a promising finding. Certainly an HMM could be tailored to more closely inform the GLM about the spike trains.

Figure 6.14 A: For the 57 modeled cells, the raster of spike times for 10s of white noise stimulation is shown (above). Below is the most likely HMM state during the same time interval. States have been sorted according to their corresponding coefficients in one of the GLM models fit (one cell). B: The AUC across the array for the entire population. C: Comparison of AUC between the LFP value/PSD and the HMM GLM. The HMM GLMs are worse at predicting spikes than the much higher dimensional LFP value/PSD GLMs.

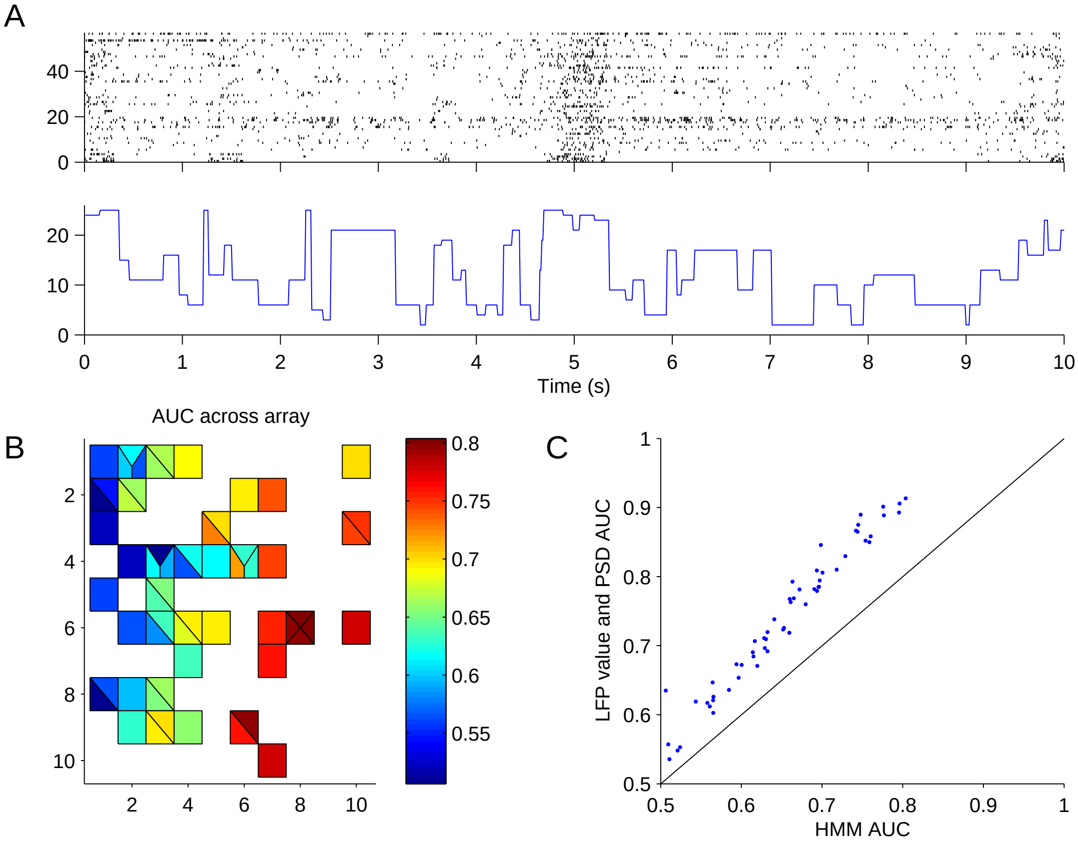

6.3 Discussion

We have shown that some features of the LFP carry more information about spiking behavior than other features. Namely, the power in the gamma frequency band is highly related to spiking in many cells, and the LFP value itself was also related. The phase of the low frequency oscillations and the power in other frequency bands were less relevant for predicting spiking activity. Still, other models of network state in place of LFP models may be better suited for this task: Lawhern et al. (2010) use the same GLM framework but incorporate a hidden network state variable that can explain network related activity.

We gave an example of fitting a GLM with HMM states. Though this particular model performed poorly relative to the best LFP models, incorporating the HMM into the framework is trivial and a better HMM could potentially reduce the dimensionality of the final model while perhaps capturing the hidden network state more accurately. We fit this HMM in a naive way with a generic prior, and a more informed model would do a better job capturing the relevant network dynamics. We ignored spiking activity when building the HMM, but taking spikes into account during the HMM fitting would probably emphasize those features related to spiking in the states.

When compared to spike coupling terms, the combined LFP power and value model has fitting performance very similar to the spike coupling models. The LFP reflects activity over a very broad region, and thus this result shows that the pairwise connectivity between two cells in the population do not generally have more predictive power than the more broad network dynamics. Our data thus suggests that much of the power of the spike coupling terms is a direct result of both cells being driven by the underlying network dynamics, rather than by a direct connection between the two cells unrelated to the more global dynamics.

Chapter 7

Implications

In this work we have laid out a procedure for modeling spike trains using various measurements taken simultaneously. Our analysis focused on cells for which the spike-triggered average had visible features. For these cells, we fit GLMs to data recorded during the presentation of a Gaussian white noise movie stimulus. When fitting spatiotemporal receptive field terms alone, all cells showed an increase in the ROC AUC from the .5 chance level, and the fitness quality distribution was related to the recording position on the array. When fitting network components alone, the performance distribution followed the opposite pattern. The cells with best AUC values when fit with stimulus terms tended to have among the lowest AUC values when fit with network terms. Models which included both kinds of terms showed modest improvements over either type of term alone.

We also fit models using different properties of the LFP. The LFP value and the LFP power spectral density, especially in the gamma frequency band (30 Hz — 80 Hz) provided good fits to the data while the LFP phase provided little information. The predominant characteristic of these fits was that signals recorded on nearby electrodes had the largest coefficients and were most likely to be included in the models. More complex models of the network state using the LFP are possible in this framework, and we used an LFP HMM as an example.

To address the goals set out in the introduction, we fit models including the most useful terms. These models included stimulus terms, spike coupling terms, LFP value, and LFP PSD. All terms were standardized and shared the same L1 penalty λ.

$$\log \mu(t) = \sum_{x}\sum_{y}\sum_{\tau} k_{xy\tau} I_{xy}(t-\tau) + \sum_{i} \alpha_i r_i(t-\tau_0) + \sum_{j} \upsilon_j L(t) + \sum_{k} \beta_k P(t) \quad (7.1)$$

where $I_{xy}(t)$ is the stimulus at spatial point (x, y), r_i is the spike count for cell i in the last

100 ms, L is the LFP value, and P is the power in the LFP gamma band. The coefficients $k, \alpha, \upsilon, \beta$ were all fit together.

7.1 Neuronal variability and shared noise

Neuronal firing has long been accepted to have sources of noise that have typically been ignored or removed. The simplest conception is that each of these cells has an independent source of intrinsic noise, and to recover the underlying firing rate function we can simply repeat the experiment many times. We have found that for many cells, the noise is not independent and is related to features of the network, like other cells or the LFP.

Cell firing was related to a combination of network effects and stimulus effects. The population included a distribution of cells, and the GLM fits to the data showed that some cells included mostly network terms, and other cells included mostly stimulus terms. For most cells, the models included both kinds of terms. Figure 7.1 shows the full firing rate μ for 3 example cells. Two of these cells are on the extremes: one of them has weight in only the stimulus terms and the other has weight only in the network terms. The other cell is more representative of most of the population - it has stimulus terms and network state terms.

In Chapter 3 we showed that by weighting spikes by the network state, the variability of the spike trains is diminished. With respect to the variety of models we built in the intervening chapters, the AUC values provide a way to measure the variability explained by different models. Figure 7.2A shows the AUCs of the stimulus model alone compared against the AUCs computed with the full models. The inclusion of network terms do indeed explain more of the variability of the spike trains than the stimulus model alone. There remains the possibility that the network terms are actually capturing stimulus information better than the stimulus terms themselves, so we also performed an AUC analysis on separate data: 120 trials of the same 30 second noise movie. Since the stimulus was repeated we were able to shuffle trials. Any stimulus information is present on every trial of this repeated stimulus, and so if the AUC improvement is entirely due to the network terms capturing stimulus information, there should be no decrease in AUC in the trial-shuffled condition. Figure 7.2B shows that this is not the case: trial shuffling reduces AUC values greatly across the population.

As mentioned in the first chapter, the PSTH is typically used as a proxy for the stimulus effects. The idea behind this is that any noise terms are averaged out after many trials to the same repeated stimulus. For the data set of a single repeated noise movie, we made a comparison of the AUC values computed from the PSTH to the AUC values due to the

Figure 7.1 For the same 10 seconds of stimulation, the model fits to 3 different cells. For each cell, three models are shown: a stimulus term only model (top), an LFP term only model (middle), and a full model with stimulus, spike coupling, and LFP terms (bottom). A: Stimulus dependent cell. The stimulus only model explains the firing of this cell well, while network components have little relation to firing. B: Network state cell. The stimulus terms do not provide much information about spiking, while network terms are predictive. C: Hybrid cell. This cell contains significant terms for both the network and for the stimulus. The full model can harness both of these forces.

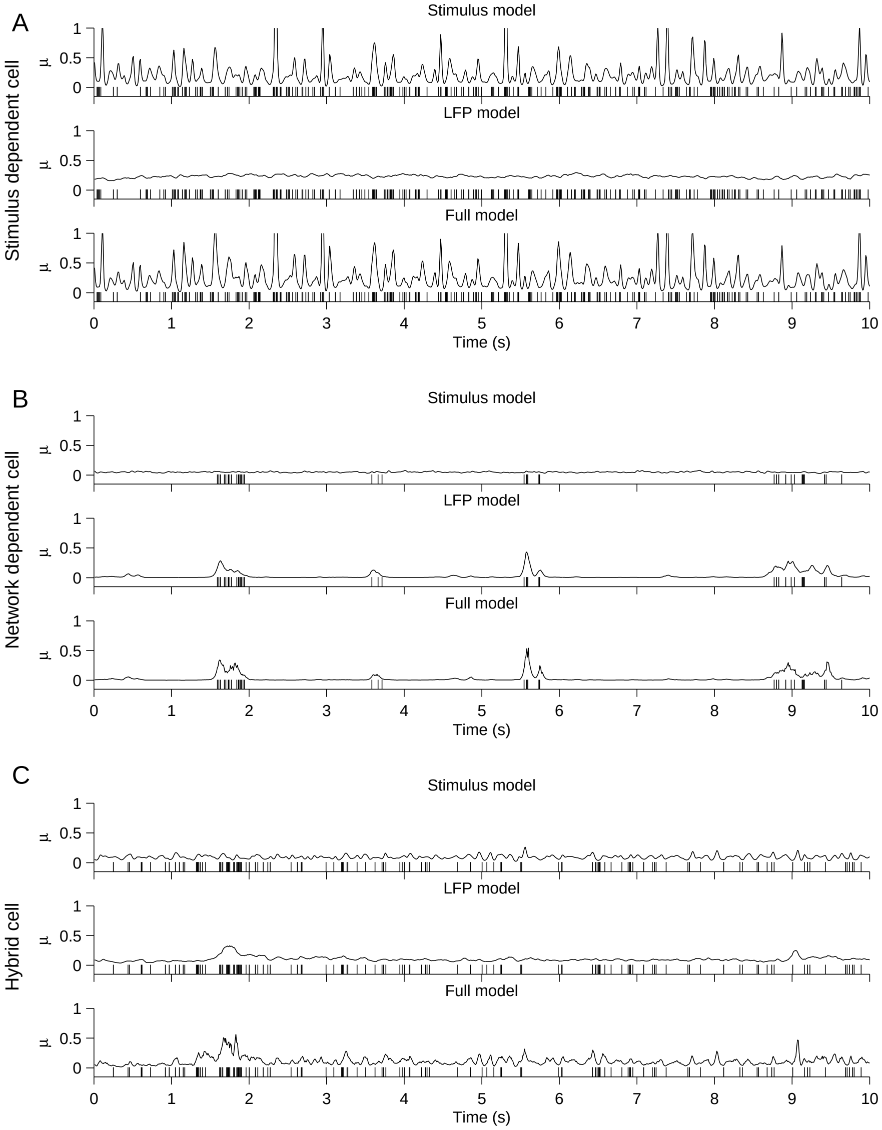

Figure 7.2 A: The AUC values of two models compared. The stimulus model contains only the explicit stimulus terms corresponding to the receptive field. The full model contains these terms as well as spike coupling terms and LFP value and PSD terms. B: For the full model, the AUCs of two different conditions during the presentation of a repeated noise movie. In the shuffled condition, the spike train from an adjacent trial is used to assess performance.

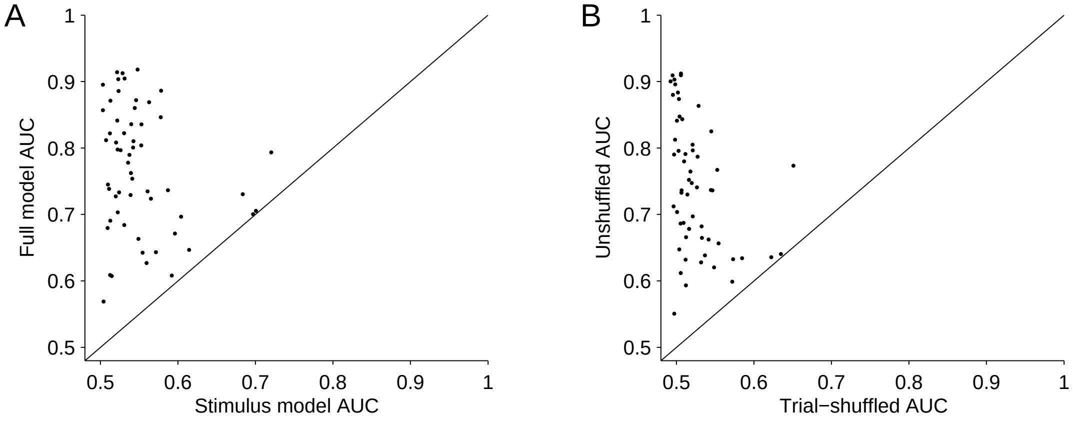

models. Recall that the AUC is computed from an ROC analysis on the thresholded μ function. Here, we define μ_{PSTH} to be the estimated firing rate given by the PSTH. Thus, it is the same function for every trial to the repeated stimulus. We compared the AUC values in the same manner as in the model procedure above, building the μ_{PSTH} function on 90% of the trials and holding out 10% of the trials for the ROC computation. Figure 7.3 shows the comparison; in most cells the full model is better than predicting the spikes than the PSTH.

If the stimulus unrelated noise has truly been averaged out of the PSTH, the stimulus-only model should do equally well in modeling the PSTH as the full model, which contains network terms. To see the ability of different models to reconstruct the PSTH, we computed the predicted firing rates (μ) to each of the 120 trials, and the predicted PSTH is simply the average of these 120 temporal functions. We computed these model predictions for the LFP model, stimulus model, and full model. Figure 7.4 shows examples of these simulated PSTHs for these three conditions. For this cell, the full model could explain over 40% of the variance in the PSTH.

Figure 7.5 shows these results for the population. The stimulus model predicted the PSTH well for some cells, but for many others the stimulus model alone cannot match

Figure 7.3 A comparison between a model made from the measured PSTH and the full model. In most cells the full model outperforms the PSTH model.

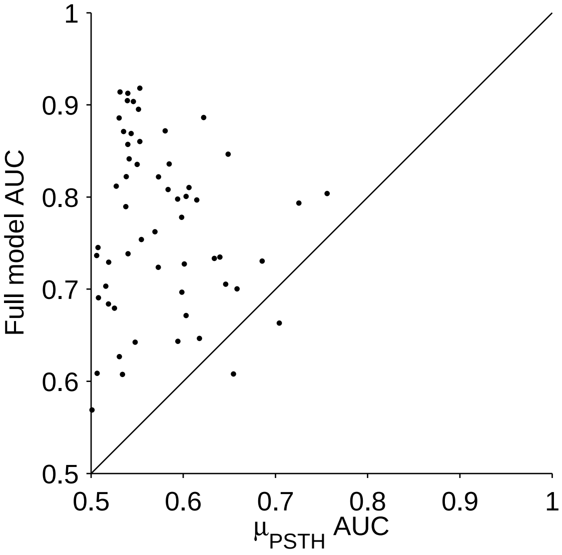

the full model's performance, indicating a corruption of the PSTH by network effects. Figure 7.5A-C show the amount of variance explained in the measured PSTH by each of the 3 models. Figure 7.5D-E show the scatter plots for the same data for the full model against each of the other models. Most cells in our population have both stimulus and network effects in the PSTHs. This is an important finding

The results we present in this work show that trial-to-trial variability can be captured more thoroughly by models which take components of the network into account. For some cells this extra explained variability is low, but for many cells it proves to be a strong effect. We have showed in chapter 3 that modeling the network induced variability can be a valuable tool in reconstructing the relationship the cell has with the stimulus when compared to traditional PSTH based methods. In addition, the AUC results throughout this work show that this modeling is very important in understanding single trial spike trains.

Figure 7.4 Estimation of the PSTH for a single cell. The reconstructions with 3 difference models are shown. The full model, capturing trial-by-trial variations in addition to stimulus effects, models the PSTH most faithfully.

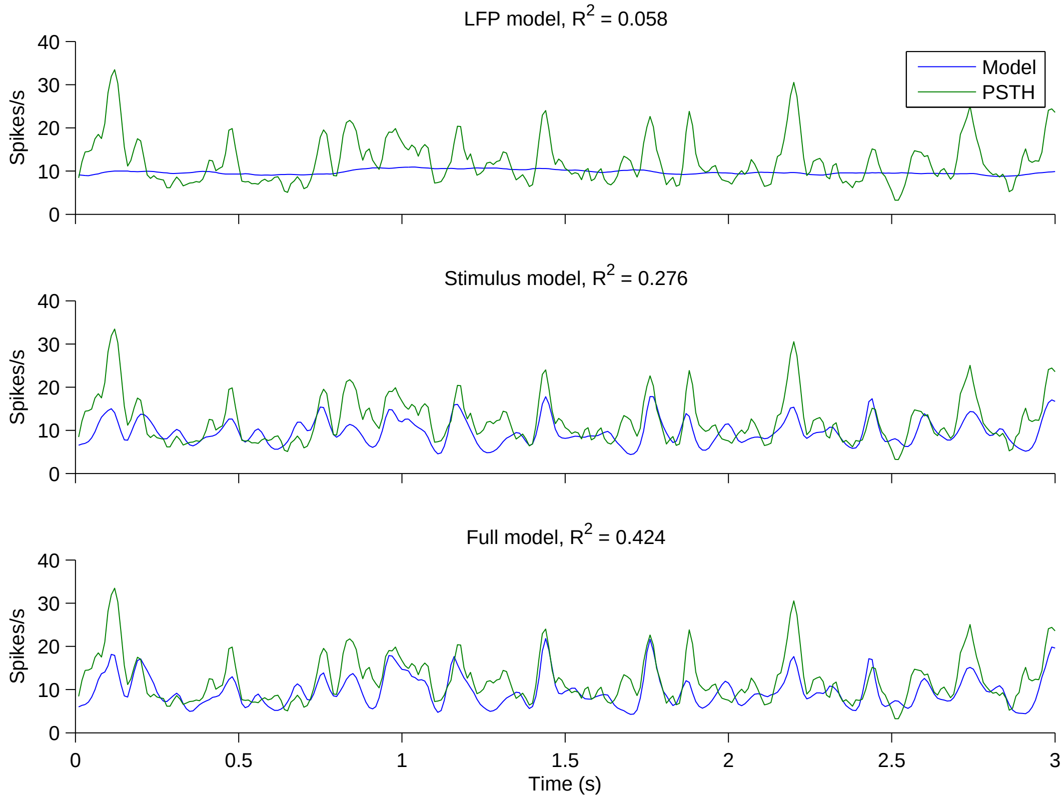

Figure 7.5 Population summary for the PSTH reconstructions. A-C: The PSTH estimates from full model have generally higher correlation with the PSTH than the LFP alone or stimulus alone models. D-E: The scatters corresponding to some of the same data in A-C.

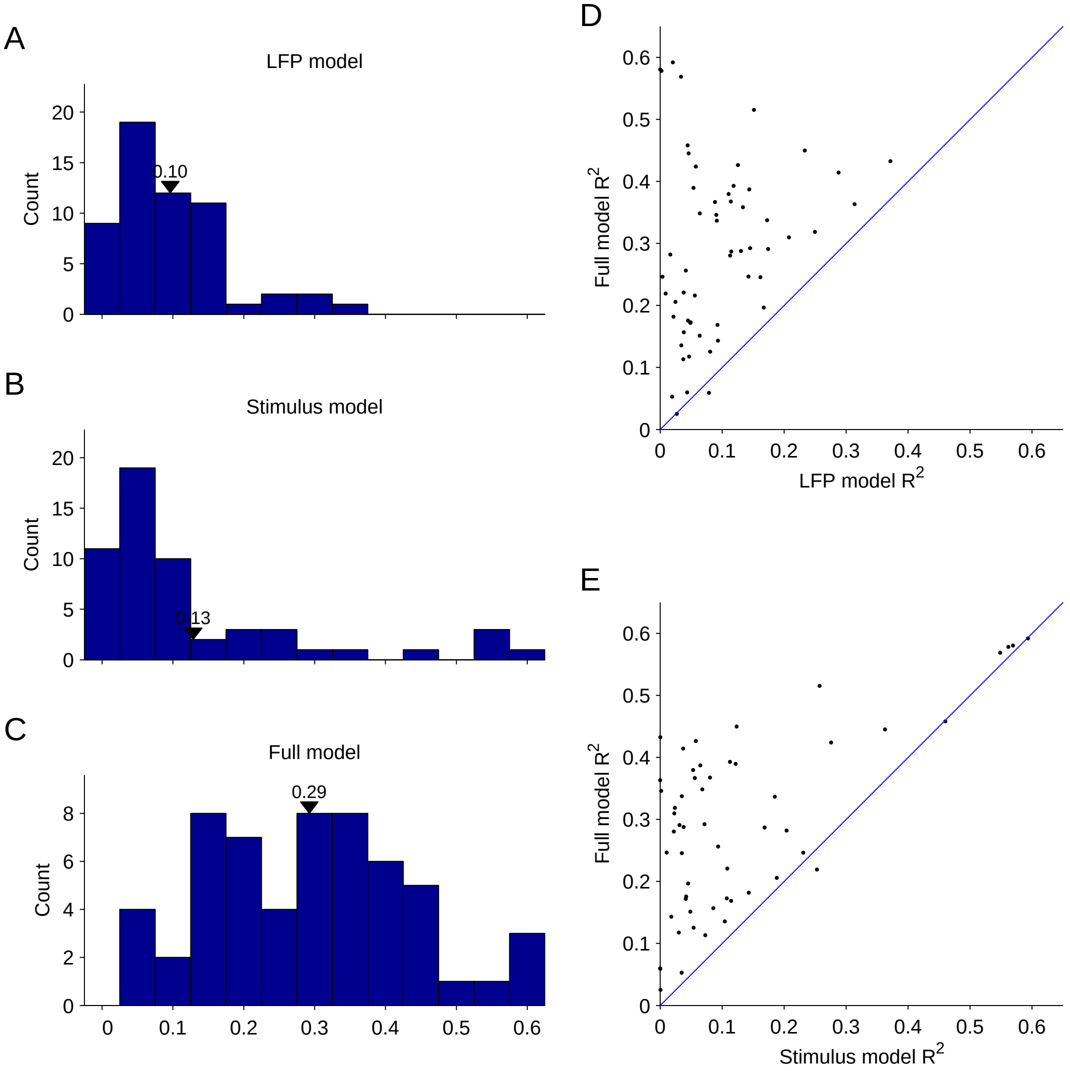

7.2 Correlation and functional connectivity

We have discussed various methods for measuring functional connectivity. Noise correlation is a long time scale measure, and captures the variations in firing rate during identical visual stimulation conditions. The cross-correlogram is a measure of the temporal correlation at different relative time lags. Many groups have used this measure as an estimate of functional connectivity, and they employ a variety of corrections. Trial shuffling can be used to reduce correlation due to correlation in the stimulus. Long-timescale correlation can greatly increase an estimate of spike synchrony, and jitter correction or spike shuffling can be used to constraint the timescale of the measurement.

Our work on modeling the spike trains opens the door to a new way of correcting the cross-correlation. The models that we have constructed make it very easy to simulate spike trains under identical network conditions. We propose that the large network effects can bias the measured functional connectivity, even with the corrections described above. For example, estimation of the amount of spike synchrony that occurs beyond chance can be related to a true local connection, or it can be related to the network state in the larger region becoming suddenly more active.

Here, we show an example of this kind of analysis. For each pair of cells, we compared the measured cross-correlation to the cross-correlation predicted by our models. In the same vein as Lawhern et al. (2010), we simulated the same 120 trials from the LFP influence models, and computed the cross-correlation for each of these models. We repeated the process 100 times to achieve 95% confidence bands on the cross-correlation function. Figure 7.6 shows five distinct pairs of cells and their true cross-correlation functions. The dotted lines indicate the 95% confidence bands given by the corresponding models. The stimulus-only models do not explain much of the measured correlation for this kind of stimulus, and the bands remain flat. The LFP models and full models tend to explain most of the rise in the cross-correlation function on the scale of hundreds of milliseconds, but often do not capture precise temporal correlation or synchrony. Figure 7.7 shows the summary of the fitness over the complete set of pairs (n=1596).

This same process can be employed in a variety of contexts and analyses, to find expected values for many measurements, from other measures of functional connectivity to maximum entropy models (Reynolds et al., 2000). These methods pave the way toward understanding the subtleties of functional connectivity while controlling for specified cell influences.

Figure 7.6 For five example cell pairings, the measured cross correlation is shown (5 rows), and the model estimates of the cross correlation for those same pairs is shown (3 models, Full, LFP, Stimulus). On the right, the cell locations on the array are shaded black. The dotted line estimates of the cross correlation are the 95% confidence bands computed with the bootstrap procedure.

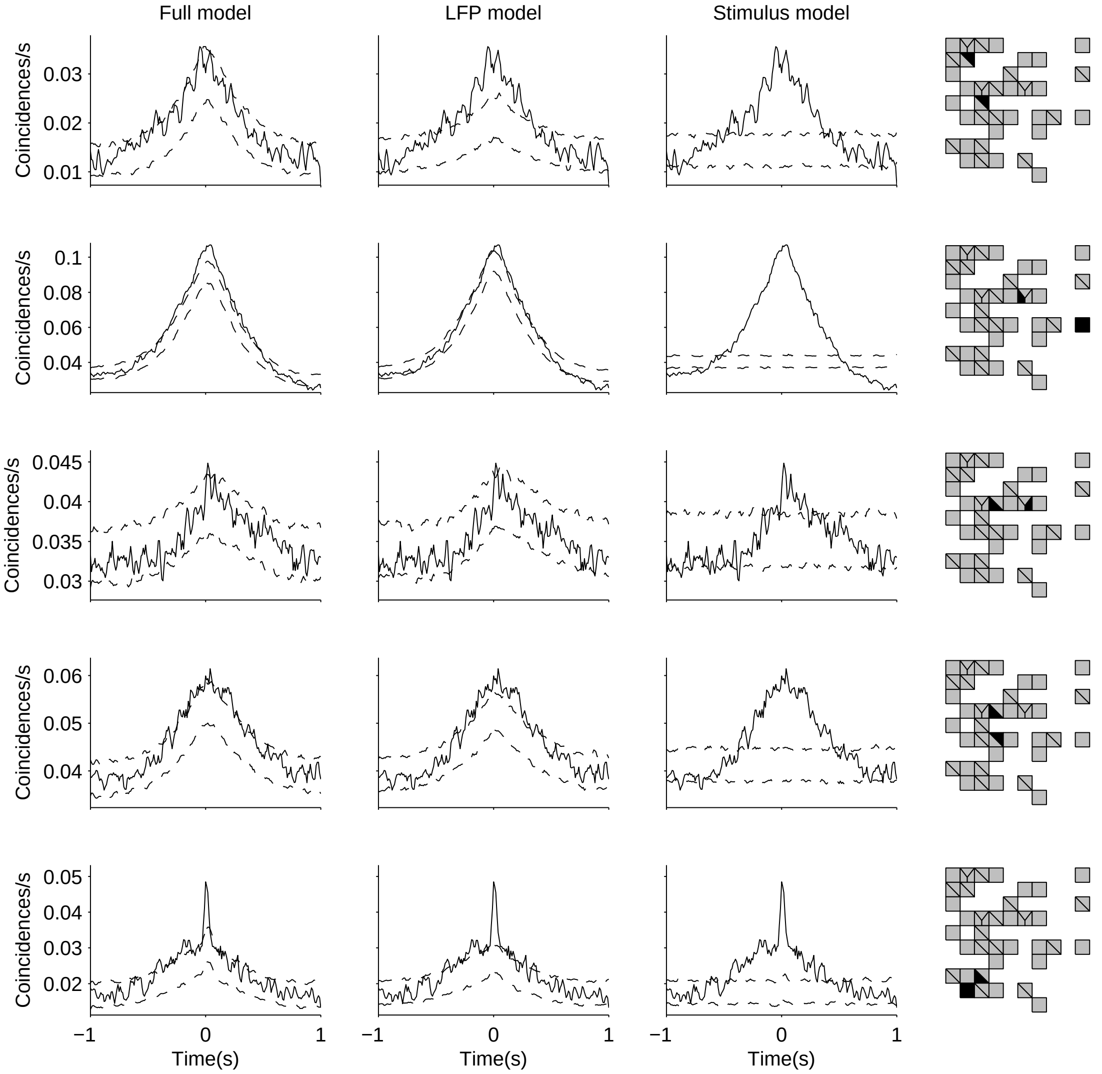

Figure 7.7 Population summary of the correlation between the measured correlation and the model predicted correlation for all cells in the population for the 3 models.

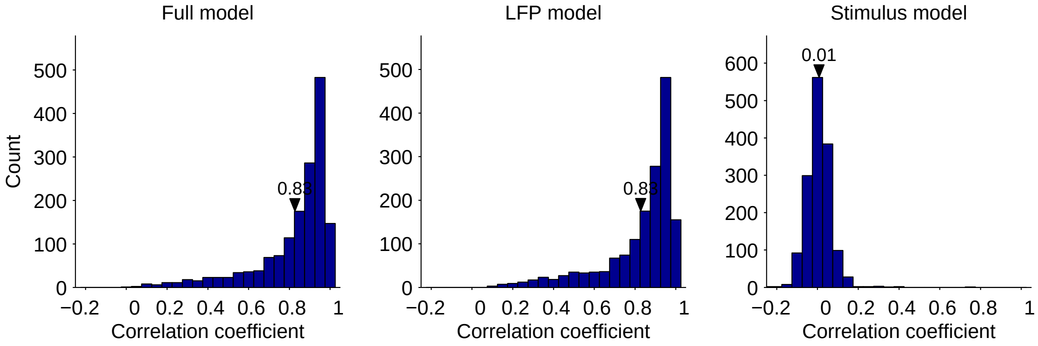

7.3 Local field potentials

We have found that local field potentials can be good indicators of spiking activity for many cells. The raw LFP values and the power in the gamma band both provide good predictability. Moreover, they generally provide comparable performance to models made from the spikes of other cells. The finding that there is little advantage to spike coupling models over the LFP models shows that these two kinds of models are mostly accounting for the same kind of effects. LFP terms are driven by many hundreds of cells over a large region, and they are not affected much by very local, direct connections. Thus, these direct and local connections are playing a comparably small role in driving spiking activity.

Of course, the limitations of the GLM models may be to blame for this similarity of performance. Much of the variance in the spike trains remain unexplained, and even the most complete model here does not perform perfectly. It is possible that a different model could harness information in the firing of other cells to improve spike train prediction, and that these models are unable to do so. It is also possible that modeling the coupling filters in different ways could improve the performance dramatically. We can conclude here that with the models we have tested, the LFP and the spike coupling terms both capture a dominant and slow network effect rather than a fast timescale direct coupling, and that this general network activity has a profound effect on spiking activity and derived measurements such as correlation.

7.4 Other issues and future directions

Layer Differences

Throughout the results in the previous chapters, we have shown distributions of many of the population measurements across the array. To sum them up, one side of the array tended to have the best STAs, and had the corresponding best AUC values when fit with the stimulus-only models. On the other side of the array, units had poorer stimulus-spiking relationships, and they had correspondingly poor STAs. These cells were driven strongly by the network effect, and their spikes were well predicted by the spike coupling models or the LFP models. Though we lack the histology to confirm our suspicions, we believe these effects are due to a layer difference in the electrode tip locations. Smith and Kohn (2009) have shown that cells in layer 4C tended to have smaller network effects compared to cells in superficial layers. Layer 4C cells receive inputs from the LGN, so they are more likely to be simple cells (Ringach et al., 2002b), which are easier to model with the kind of terms we have presented in this work. We will continue this work by extending the analysis to other arrays, and to cells with known layer locations.

Anesthesia

The data analyzed here were all recorded from an anesthetized animal. Different types of anesthesia act through a number of neurotransmitter systems (Ringach et al., 2002b). In these experiments we used sufentanil anesthesia, which acts on mu-opioid receptors not found in primary visual cortex (Lewis et al., 1983). There have not been any significant differences reported in the firing properties of V1 neurons between awake and sufentanil anesthetized animals (Movshon et al., 2003). Nonetheless, anesthesia is known to affect synchronized fluctuations of neural activity. This can be reflected in the EEG, but also in more local measures of network activity like the LFP. However, a number of studies have shown that network fluctuations exist in the awake animal, although they are modified by behavioral state. Based on intracellular membrane potential recordings, Poulet and Petersen (2008) demonstrated low frequency correlated fluctuations when mice are quiet but awake. These fluctuations decreased but were still present when the animals were actively exploring their environments. Similarly, in macaque area V4, noise correlation is reduced by visuospatial attention (Cohen and Maunsell, 2009; Reynolds et al., 2000). Thus, some of the strong network related spiking activity documented in this work may be related to anesthesia. This does not reduce the validity of the method, but tempers possible interpretations of the results. For example, we found models which predict the firing of network related cells very well, while failed to find receptive field models that performed as well. It is possible that in an awake, behaving animal this tendency would be reduced or reversed. We plan to perform these analyses on data recorded in awake animals to more fully understand the effects of anesthesia on cell spiking and network states.

Model parameters

We have made choices in our model selections due to computational constraints, data constraints, and lack of knowledge. To build these models in a conventional computer in a reasonable amount of time, we were limited to less than 1000 parameters for the 32 minutes of noise. More efficient computational algorithms, or faster computers with more memory, could greatly expand the number of parameters fit. In terms of spike coupling, it is almost certain that more direct connections exist in the brain than the ones we measured, but we are limited only to the 128 units that we were able to sort. For this we would need to apply these methods to a larger data set, and greater signal to noise would of course be helpful. Regarding the LFP, a better model of network state than the power in the gamma frequency band is sure to exist, but our understanding of the LFP is severely limited. This kind of modeling actually provides a computational method for assessing the relative performance of LFP models, but even the treatment we have provided in this work is limited.

Other stimuli

In Chapters 5-7, we fit GLMs to data recorded during visual stimulation with white noise movies. The general effects we describe throughout this work do indeed apply qualitatively to other stimulation conditions, as described in Chapter 3. We observed network fluctuations during spontaneous activity, and in other stimulation conditions as well (natural movies, gratings). The extent to which the network drives the individual cells is unknown however. Many cells may not be responsive to the type of white noise movie we showed, and the effect this has on the network influence remains unknown. We reported primarily on 57 of the cells in the population for which a STA was visible by eye, but the rest of the cells in the population may simply be selective for other kinds of stimuli. We plan to expand these analyses to other stimulation conditions to test (1) how well the models we fit here can predict spiking to other stimulus conditions and (2) for a given cell, how models fit in one stimulus condition compare to models fit in other conditions.

Summary

As computational power continues to grow, tractable models for making sense of very large data sets will grow in importance. In this document we have laid out and justified the methods for fitting generalized linear models to spike trains using high dimensional data from the stimulus, spike coupling, and LFP. We have shown that variability in spiking to repeated presentations of identical stimuli can be explained in large part by the general network activity, in many cells. These models have broad application, from the recovery of single trial firing rate functions and model assessment to the explanation of neural phenomena like correlation and synchrony.

Bibliography

Abbott LF, Dayan P (1999) The effect of correlated variability on the accuracy of a population code. *Neural Comput* 11:91–101. 1.1

Adrian ED (1928) *The Basis of Sensation* Christophers London. 1

Arieli A, Sterkin A, Grinvald A, Aertsen A (1996) Dynamics of ongoing activity: explanation of the large variability in evoked cortical responses. *Science* 273:1868–71 Notes. 3.5

Averbeck BB, Latham PE, Pouget A (2006) Neural correlations, population coding and computation. *Nat Rev Neurosci* 7:358–66. 1.1, 5.2.1

Bair W, Zohary E, Newsome WT (2001) Correlated firing in macaque visual area MT: time scales and relationship to behavior. *J Neurosci* 21:1676–97. 3.1, 3.5

Berens P, Keliris GA, Ecker AS, Logothetis NK, Tolias AS (2008) Feature selectivity of the gamma-band of the local field potential in primate primary visual cortex. *Frontiers in neuroscience* 2:199–207. 1.1, 3.5

Buzsáki G (2004) Large-scale recording of neuronal ensembles. *Nat Neurosci* 7:446–51. 1.1

Cavanaugh JR, Bair W, Movshon JA (2002) Nature and interaction of signals from the receptive field center and surround in macaque V1 neurons. *J Neurophysiol* 88:2530–46. 2.1, 2.2

Cohen MR, Maunsell JHR (2009) Attention improves performance primarily by reducing interneuronal correlations. *Nat Neurosci* 12:1594–600. 7.4

David SV, Vinje WE, Gallant JL (2004) Natural stimulus statistics alter the receptive field structure of v1 neurons. *J Neurosci* 24:6991–7006. 3.5

Dayan P, Abbott LF (2005) *Theoretical Neuroscience: Computational and Mathematical Modeling of Neural Systems* The MIT Press. 4.1.1, 5.1.1

DeAngelis GC, Ohzawa I, Freeman RD (1993) Spatiotemporal organization of simple-cell receptive fields in the cat's striate cortex. I. General characteristics and postnatal development. *J Neurophysiol* 69:1091–117. 5.1.1

Destexhe A, Contreras D (2006) Neuronal computations with stochastic network states. *Science* 314:85–90.

Ecker AS, Berens P, Keliris GA, Bethge M, Logothetis NK, Tolias AS (2010) Decorrelated neuronal firing in cortical microcircuits. *Science* 327:584–7. 1.1

Eggermont JJ, Johannesma PM, Aertsen AM (1983) Reverse-correlation methods in auditory research. *Q Rev Biophys* 16:341–414. 5.1.1

Eggermont JJ, Smith GM (1995) Synchrony between single-unit activity and local field potentials in relation to periodicity coding in primary auditory cortex. *J Neurophysiol* 73:227–45. 1.1, 3.5

Foster KH, Gaska JP, Nagler M, Pollen DA (1985) Spatial and temporal frequency selectivity of neurones in visual cortical areas V1 and V2 of the macaque monkey. *J Physiol (Lond)* 365:331–63. 2.3

Friedman J, Hastie T, Tibshirani R (2008) Regularization paths for generalized linear models via coordinate descent. *Department of Statistics* . 1.1, 4, 4.2.2, 4.2.3

Frien A, Eckhorn R, Bauer R, Woelbern T, Gabriel A (2000) Fast oscillations display sharper orientation tuning than slower components of the same recordings in striate cortex of the awake monkey. *Eur J Neurosci* 12:1453–65. 1.1

Gray CM, Maldonado PE, Wilson M, McNaughton B (1995) Tetrodes markedly improve the reliability and yield of multiple single-unit isolation from multi-unit recordings in cat striate cortex. *J Neurosci Methods* 63:43–54. 3.1

Hardin JW, Hilbe J (2007) *Generalized Linear Models and Extensions* College Station, Texas: Stata Press. 3.2

Harrison M, Amarasingham A, Geman S (2007) Jitter methods for investigating spike train dependencies In *Abstracts III-17*. Computational and Systems Neuroscience. 5.2.2

Haslinger R, Ulbert I, Moore CI, Brown EN, Devor A (2006) Analysis of LFP phase predicts sensory response of barrel cortex. *J Neurophysiol* 96:1658–63. 1.1

Hatsopoulos NG, Xu Q, Amit Y (2007) Encoding of movement fragments in the motor cortex. *J Neurosci* 27:5105–14. 4.3

He BJ, Snyder AZ, Zempel JM, Smyth MD, Raichle ME (2008) Electrophysiological correlates of the brain's intrinsic large-scale functional architecture. *Proc Natl Acad Sci USA* 105:16039–44. 1.1

Henrie JA, Shapley RM (2005) LFP power spectra in V1 cortex: the graded effect of stimulus contrast. *J Neurophysiol* 94:479–90. 1.1, 6.1

Hodgkin AL, Huxley AF (1952) A quantitative description of membrane current and its application to conduction and excitation in nerve. *J Physiol (Lond)* 117:500–44. 1.1

Huang X, Lisberger SG (2009) Noise correlations in cortical area MT and their potential impact on trial-by-trial variation in the direction and speed of smooth-pursuit eye movements. *J Neurophysiol* 101:3012–30. 1.1, 3.1, 3.5

Hubel DH, Wiesel TN (1962) Receptive fields, binocular interaction and functional architecture in the cat's visual cortex. *J Physiol (Lond)* 160:106–54. 1

Hubel DH, Wiesel TN (1968) Receptive fields and functional architecture of monkey striate cortex. *J Physiol (Lond)* 195:215–43. 2.2.2

Johnson HA, Buonomano DV (2007) Development and plasticity of spontaneous activity and Up states in cortical organotypic slices. *J Neurosci* 27:5915–25. 1.1

Jones JP, Palmer LA (1987) The two-dimensional spatial structure of simple receptive fields in cat striate cortex. *J Neurophysiol* 58:1187–211. 2.2.2, 5.1.1

Juergens E, Guettler A, Eckhorn R (1999) Visual stimulation elicits locked and induced gamma oscillations in monkey intracortical- and EEG-potentials, but not in human EEG. *Experimental brain research Experimentelle Hirnforschung Expérimentation cérébrale* 129:247–59. 1.1

Kass RE, Ventura V (2001) A spike-train probability model. *Neural Comput* 13:1713–20. 3.5

Katzner S, Nauhaus I, Benucci A, Bonin V, Ringach DL, Carandini M (2009) Local origin of field potentials in visual cortex. *Neuron* 61:35–41. 1.1, 3.5

Kelly RC, Smith MA, Kass RE, Lee TS (2010) Local field potentials indicate network state and account for neuronal response variability. *J Comput Neurosci* . 1.1

Kelly RC, Smith MA, Samonds JM, Kohn A, Bonds AB, Movshon JA, Lee TS (2007) Comparison of recordings from microelectrode arrays and single electrodes in the visual cortex. *J Neurosci* 27:261–4. 1.1, 2

Kohn A, Smith MA (2005) Stimulus dependence of neuronal correlation in primary visual cortex of the macaque. *J Neurosci* 25:3661–73. 1.1, 3.1, 3.5

Kohn A, Zandvakili A, Smith MA (2009) Correlations and brain states: from electrophysiology to functional imaging. *Curr Opin Neurobiol* 19:434–8. 3.1

Körding KP, Kayser C, Einhäuser W, König P (2004) How are complex cell properties adapted to the statistics of natural stimuli? *J Neurophysiol* 91:206–12. 3.5

Kreiman G, Hung CP, Kraskov A, Quiroga RQ, Poggio T, DiCarlo JJ (2006) Object selectivity of local field potentials and spikes in the macaque inferior temporal cortex. *Neuron* 49:433–45. 1.1

Kruse W, Eckhorn R (1996) Inhibition of sustained gamma oscillations (35-80 Hz) by fast transient responses in cat visual cortex. *Proc Natl Acad Sci USA* 93:6112–7. 1.1

Lampl I, Reichova I, Ferster D (1999) Synchronous membrane potential fluctuations in neurons of the cat visual cortex. *Neuron* 22:361–74. 1.1

Lawhern V, Wu W, Hatsopoulos N, Paninski L (2010) Population decoding of motor cortical activity using a generalized linear model with hidden states. *J Neurosci Methods* . 6.3, 7.2

Legatt AD, Arezzo J, Vaughan HG (1980) Averaged multiple unit activity as an estimate of phasic changes in local neuronal activity: effects of volume-conducted potentials. *J Neurosci Methods* 2:203–17. 3.1

Leopold DA, Murayama Y, Logothetis NK (2003) Very slow activity fluctuations in monkey visual cortex: implications for functional brain imaging. *Cereb Cortex* 13:422–33. 1.1, 3.3, 6.1

Lewis ME, Pert A, Pert CB, Herkenham M (1983) Opiate receptor localization in rat cerebral cortex. *J Comp Neurol* 216:339–58. 7.4

Liu J, Newsome WT (2006) Local field potential in cortical area MT: stimulus tuning and behavioral correlations. *J Neurosci* 26:7779–90. 1.1, 3.5

Logothetis NK, Pauls J, Augath M, Trinath T, Oeltermann A (2001) Neurophysiological investigation of the basis of the fMRI signal. *Nature* 412:150–7. 6.1

Luczak A, Barthó P, Marguet SL, Buzsáki G, Harris KD (2007) Sequential structure of neocortical spontaneous activity in vivo. *Proc Natl Acad Sci USA* 104:347–52. 1.1

Mitzdorf U (1987) Properties of the evoked potential generators: current source-density analysis of visually evoked potentials in the cat cortex. *Int J Neurosci* 33:33–59. 1.1

Mountcastle V, Davies P, Berman A (1957) Response properties of neurons of cat's somatic sensory cortex to peripheral stimuli. *J Neurophysiol* 20:374–407. 1

Movshon JA, Albright TD, Stoner GR, Majaj NJ, Smith MA (2003) Cortical responses to visual motion in alert and anesthetized monkeys. *Nat Neurosci* 6:3; author reply 3–4. 7.4

Nauhaus I, Busse L, Carandini M, Ringach DL (2009) Stimulus contrast modulates functional connectivity in visual cortex. *Nat Neurosci* 12:70–6. 1.1

Nir Y, Mukamel R, Dinstein I, Privman E, Harel M, Fisch L, Gelbard-Sagiv H, Kipervasser S, Andelman F, Neufeld MY, Kramer U, Arieli A, Fried I, Malach R (2008) Interhemispheric correlations of slow spontaneous neuronal fluctuations revealed in human sensory cortex. *Nat Neurosci* 11:1100–8. 1.1

Nordhausen CT, Maynard EM, Normann RA (1996) Single unit recording capabilities of a 100 microelectrode array. *Brain Res* 726:129–40. 2.2, 2.2.1

Paninski L, Brown E, Iyengar S, , Kass R (2009) Statistical models of spike trains In Liang C, Lord G, editors, *Stochastic Methods in Neuroscience*, pp. 278–303. Clarendon Press, Oxford. 3.2, 3.5

Paninski L (2004) Maximum likelihood estimation of cascade point-process neural encoding models. *Network: Computation in Neural Systems* . 3.2

Paninski L, Pillow JW, Lewi J (2007) Statistical models for neural encoding, decoding, and optimal stimulus design. *Prog Brain Res* 165:493–507. 3

Park MY, Hastie T (2007) L1 Regularization Path Algorithm for Generalized Linear Models. *Journal of the Royal Statistical Society: Series B (Statistical Methodology)* 69:659–677. 4, 4.2.3

Perkel DH, Gerstein GL, Moore GP (1967) Neuronal spike trains and stochastic point processes. II. Simultaneous spike trains. *Biophys J* 7:419–40. 5.2.2

Petersen CCH, Grinvald A, Sakmann B (2003) Spatiotemporal dynamics of sensory responses in layer 2/3 of rat barrel cortex measured in vivo by voltage-sensitive dye imaging combined with whole-cell voltage recordings and neuron reconstructions. *J Neurosci* 23:1298–309. 1.1, 3.5

Pillow JW, Latham PE (2008) Neural characterization in partially observed populations of spiking neurons. *Adv Neural Information Processing Systems* 20. 3.5

Pillow JW, Shlens J, Paninski L, Sher A, Litke AM, Chichilnisky EJ, Simoncelli EP (2008) Spatio-temporal correlations and visual signalling in a complete neuronal population. *Nature* 454:995–9. 1.1, 3, 3.5

Pillow J (2007) Likelihood-based approaches to modeling the neural code In Doya K, Ishii S, Pouget A, Rao R, editors, *Bayesian Brain: Probabilistic Approaches to Neural Coding*, pp. 53–70. MIT Press. 3.5

Poulet JFA, Petersen CCH (2008) Internal brain state regulates membrane potential synchrony in barrel cortex of behaving mice. *Nature* 454:881–5. 7.4

Rabiner (1989) A tutorial on hidden Markov models and selected applications in speech recognition. *Proceedings of the IEEE* 77:257 – 286. 6.2.4

Rasch MJ, Gretton A, Murayama Y, Maass W, Logothetis NK (2008) Inferring spike trains from local field potentials. *J Neurophysiol* 99:1461–76. 1.1, 1.1, 3.5, 6.1, 6.1, 6.2.3

Reid RC, Alonso JM (1995) Specificity of monosynaptic connections from thalamus to visual cortex. *Nature* 378:281–4. 5.1.1

Reynolds JH, Pasternak T, Desimone R (2000) Attention increases sensitivity of V4 neurons. *Neuron* 26:703–14. 7.2, 7.4

Ringach DL, Hawken MJ, Shapley RM (2002a) Receptive field structure of neurons in monkey primary visual cortex revealed by stimulation with natural image sequences. *Journal of vision* 2:12–24. 3.5

Ringach DL, Shapley RM, Hawken MJ (2002b) Orientation selectivity in macaque V1: diversity and laminar dependence. *J Neurosci* 22:5639–51. 2.2.2, 7.4, 7.4

Rousche PJ, Normann RA (1992) A method for pneumatically inserting an array of penetrating electrodes into cortical tissue. *Ann Biomed Eng* 20:413–22. 2.1, 2.2.4

Samonds JM, Bonds AB (2005) Gamma oscillation maintains stimulus structure-dependent synchronization in cat visual cortex. *J Neurophysiol* 93:223–36. 1.1

Samonds JM, Zhou Z, Bernard MR, Bonds AB (2006) Synchronous activity in cat visual cortex encodes collinear and cocircular contours. *J Neurophysiol* 95:2602–16. 2.2

Schneidman E, Berry MJ, Segev R, Bialek W (2006) Weak pairwise correlations imply strongly correlated network states in a neural population. *Nature* 440:1007–12. 2.1

Shadlen MN, Newsome WT (1998) The variable discharge of cortical neurons: implications for connectivity, computation, and information coding. *J Neurosci* 18:3870–96. 1.1, 3.1, 3.5

Shlens J, Field GD, Gauthier JL, Greschner M, Sher A, Litke AM, Chichilnisky EJ (2009) The structure of large-scale synchronized firing in primate retina. *J Neurosci* 29:5022–31. 1.1

Shlens J, Field GD, Gauthier JL, Grivich MI, Petrusca D, Sher A, Litke AM, Chichilnisky EJ (2006) The structure of multi-neuron firing patterns in primate retina. *J Neurosci* 26:8254–66. 2.1

Shoham S, Fellows MR, Normann RA (2003) Robust, automatic spike sorting using mixtures of multivariate t-distributions. *J Neurosci Methods* 127:111–22. 2.1

Siegel M, König P (2003) A functional gamma-band defined by stimulus-dependent synchronization in area 18 of awake behaving cats. *J Neurosci* 23:4251–60. 1.1

Smith M, Kohn A (2009) Laminar dependence of neuronal correlation in macaque V1 In *Society for Neuroscience Abstracts*. 5.2.3, 7.4

Smith MA, Bair W, Movshon JA (2002) Signals in macaque striate cortical neurons that support the perception of glass patterns. *J Neurosci* 22:8334–45. 2.3

Smith MA, Kohn A (2008) Spatial and temporal scales of neuronal correlation in primary visual cortex. *J Neurosci* 28:12591–603. 1.1, 2.1, 2.1, 3.1, 3.3, 3.5, 5.2.2

Snider RK, Kabara JF, Roig BR, Bonds AB (1998) Burst firing and modulation of functional connectivity in cat striate cortex. *J Neurophysiol* 80:730–44. 2.2

Suner S, Fellows MR, Vargas-Irwin C, Nakata GK, Donoghue JP (2005) Reliability of signals from a chronically implanted, silicon-based electrode array in non-human primate primary motor cortex. *IEEE transactions on neural systems and rehabilitation engineering : a publication of the IEEE Engineering in Medicine and Biology Society* 13:524–41. 2.2, 2.2.1

Truccolo W, Hochberg LR, Donoghue JP (2010) Collective dynamics in human and monkey sensorimotor cortex: predicting single neuron spikes. *Nat Neurosci* 13:105–11. 1.1

Tsodyks M, Kenet T, Grinvald A, Arieli A (1999) Linking spontaneous activity of single cortical neurons and the underlying functional architecture. *Science* 286:1943–6. 1.1, 3.5

Valois RLD, Albrecht DG, Thorell LG (1982) Spatial frequency selectivity of cells in macaque visual cortex. *Vision Res* 22:545–59. 2.3

Xing D, Yeh CI, Shapley RM (2009) Spatial spread of the local field potential and its laminar variation in visual cortex. *J Neurosci* 29:11540–9. 1.1, 3.5

Zohary E, Shadlen MN, Newsome WT (1994) Correlated neuronal discharge rate and its implications for psychophysical performance. *Nature* 370:140–3. 1.1, 3.1, 3.5